Role of BRD4 and its target *Ptp1b* in Endothelial cells and in cardiovascular disease models

Dissertation

For the award of the degree

"Doctor of Philosophy (Ph.D.)"

at the Georg-August University Goettingen

Within the doctoral Programme GAUSS-Biology

of the Georg-August University School of Sciences (GAUSS)

Submitted by

Sidra Shahid

From Lahore, Pakistan

Goettingen 2019

Thesis Advisory Committee

1. **Prof. Dr. Ibrahim Adham**

   Institute of Human Genetics, University Medical Centre Goettingen (UMG)

   Georg-August University Goettingen Germany.

2. **Prof. Dr. Sigrid Hoyer-Fender**

   Department of Development Biology,

   Georg-August University Goettingen Germany.

3. **Dr. Krishna Pantakani**

   Institute for Clinical Chemistry, University Medical Centre Goettingen (UMG)

   Georg-August University Goettingen Germany.

Members of examination board

Referee: **Prof. Dr. Ibrahim Adham**

   Institute of Human Genetics, University Medical Centre Goettingen

   (UMG), Georg-August University Goettingen Germany.

Co-referee: **Prof. Dr. Sigrid Hoyer-Fender**

   Department of Developmental Biology,
   Georg-August University Goettingen Germany.

Other members of examination board

1.   **Prof. Dr. Uwe Groß**

   Institute for Medical Microbiology, University Medical Centre
   Goettingen.

2.   **Prof. Dr. Ahmed Mansouri**

   Max Planck Institute for Biophysical Chemistry, Goettingen.

3.   **Prof. Dr. Ralf Dressel**

   Institute for Cellular and Molecular Immunology, University Medical
   Centre Goettingen.

4.   **PD, Dr. Michael Hoppert**

   Department of General Microbiology, Georg August University
   Goettingen.

Date of oral examination: 13.02.2019

Declaration

I hereby declare that the Ph.D. thesis entitled "Role of BRD4 and its target *Ptp1b* in Endothelial cells and in cardiovascular disease models" has been written independently, with no other sources than quoted, and has not been used or submitted in support of an application for another degree.

<div align="right">

Sidra Shahid

17.01.2019

</div>

Dedicated to my parents, family and friends for their love, affection, encouragement and support

Table of Contents

List of abbreviations

Ang-II	Angiotension II
ANOVA	Analysis of variance
Apo-A1	Apolipoprotein-A1
ATP	Adenosine triphosphate
BD1	Bromodomain 1
BD2	Bromodomain 2
BET	Bromodomain and extra terminal domain
BH4	(6R)-l-erythro-5,6,7,8-tetrahydrobiopterin
BRD4	Bromodomain containing protein 4
BRD4-L	Bromodomain containing protein 4 long isoform
BRD4-S	Bromodomain containing protein 4 short isoform
BSA	Bovine serum albumin
C2C12	Muscle myoblasts cell line
Caco-2	Human epithelial colorectal adenocarcinoma cells
Cam	Calmodulin
CAs	Carbonic anhydrases
CA-I	Carbonic anhydrase-I
CA-II	Carbonic anhydrase-II
Cal27	Oral carcinoma cell line
Cav-I	Caveolin I
ChIP	Chromatin immunoprecipitation
ChIP-seq	Chromatin immunoprecipitation with massively parallel DNA sequencing
CnA	Calcineurin A
CnB	Calcineurin B
CO_2	Carbon dioxide
CSFR-1	Colony stimulating factor 1 receptor
CTD	Carboxy-terminal domain
CVDs	Cardiovascular diseases
Da	Dalton
DAPI	4`,6-Diamidino-2Phenylindole, Dihydrochloride
DEPC	Diethylpyrocarbonate

DIA	Data independent acquisition
DMEM	Dulbecco's modified eagle medium
DMSO	Dimethyl sulfoxide
dNTPs	deoxyribonucleotide triphosphate
DPBS	Dulbecco's phosphate-buffered saline
DTT	Dithiothreitol
ECM	Extracellular matrix
ECs	Endothelial cells
EDTA	Ethylenediaminetetraacetic acid
EGTA	Egtazic acid
Endo.*Ptp1b*.KO	Mice with endothelial-specific deletion of PTP1B
Endo.*Ptp1b*.WT	Wild Type mice
eNO	Endothelial specific nitric oxide
eNOS	Endothelial specific nitric oxide synthase
ER	Endoplasmic reticulum
ET	Extra terminal domain
et al.,	"and others."
ETC	Electron transport chain
ET-I	Endothelin-1
EVOM2	Epithelial voltammeter
FCS	Foetal calf serum
FDR	False discovery rate
FGF	Fibroblast growth factors
FHL1	Four and a half LIM domains 1
FWHM	Full width at half maximum
GAPDH	Glyceraldehyde 3-phosphate dehydrogenase
GJA1	Gap junction alpha-1 protein
GLUT4	Glucose transporter
GO	Gene ontology
GPCRs	G-protein-coupled receptors
Gpx	Glutathione oxidase
KO-SHAM	Ptp1b knockout mice without transverse aortic constriction, used as an experimental control

KO-TAC	Ptp1b knockout mice with transverse aortic constriction
H3K14	Histone 3 lysine 14
H4K12	Histone 4 lysine 12
H4K5	Histone 4 lysine 5
HATs	Histone acetyltransferases
HDACs	Histone deacetylases
HDL	High-density lipoprotein
HRP-conjugated	Horseradish peroxidase-conjugated
hr	Hour
hrs	Hours
HUVECs	Human Umbilical cord derived vascular endothelial cells
IAA	Iodoacetamide
ICAM-1	Intercellular adhesion molecule 1
IGF	Insulin growth factors
IGFR	Insulin growth factor receptor
IκB-α	NF-κB inhibitor
Iκκ	IκB-Kinase
IL1	Interleukin-1
IL1β	Interleukin 1β
IL6	Interleukin-6
IL8	Interleukin-8
IPA	Ingenuity pathway analysis
IRAK1	Interleukin receptor associated kinase 1
JAK	Janus-Kinase
JQ1	(6S)-4-(4-chlorophenyl)-2,3,9-trimethyl-6H-thieno[3,2-f][1,2,4]triazolo[4,3-a][1,4]diazepine-6-acetic acid, 1,1-dimethylethyl ester
kDa	Kilo Dalton
LC-MS/MS	Liquid chromatography-tandem mass spectrometry
LDL	Low-density lipoprotein
LDL-Cholesterol	Low-density lipoprotein cholesterol
LPS	Lipopolysaccharides
MAPKs	Mitogen activated protein kinases

MHCs	Myosin heavy chains
MI	Myocardial Infarction
mins	minutes
MLCs	Myosin light chains
mM	Mili molar
M-MLV-RT	Moloney murine leukemia virus reverse transcriptase
mTOR	Mammalian target of rapamycin
MyD88	Myeloid differentiation primary response 88
Na_2EDTA	Disodium ethylenediaminetetraacetic acid
Na_3VO_4	Sodium orthovanadate
NFAT	Nuclear factor of activated T cells
NF-κB	Nuclear transcription factor κB
nM	Nano molar
NO	Nitric oxide
p65	RelA subunit of NF-κB
PAK-1	p21-activated kinase-1
PCA	Principal component analysis
PCR	Polymerase chain reaction
PDGFR	Platelet derived growth factor receptor
PFA	Paraformaldehyde
PI3K	Phosphoinositol-3-kinase
PMSF	Phenylmethylsulfonyl fluoride
P-TEFB	Positive transcription elongation factor
PTP1B	Protein tyrosine phosphatase 1B
Ptp1b-KO	Mice with PTP1B deficiency
PTPs	Protein tyrosine phosphatases
qRT-PCR	Quantitative real time polymerase chain reaction
RNA Pol-II	RNA polymerase II
ROS	Reactive oxygen species
RT	Room temperature
RTKs	Receptor tyrosine kinases
RVX-208	2-[4-(2-hydroxyethoxy)-3,5-dimethylphenyl]-5,7-dimethoxy-4(3H)-quinazolinone

SDS	Sodium dodecyl sulfate
SDS-PAGE	Sodium dodecyl sulfate polyacrylamide gel electrophoresis
SELE	E-Selectin
SEM	Standard error of mean
SEs	Super enhancers
shRNA	Short hairpin RNA
SMCs	Smooth muscle cells
STAT	Signal transducer activator of transcription
STRING	Search Tool for the Retrieval of Interacting Genes/Proteins
SWATH	Sequential Window Acquisition of all Theoretical fragment ion spectra
TAC	Transverse aortic constriction
TBST	Tris-buffered saline with tween
TEER	Trans-endothelial/epithelial electrical resistance
TGFβ	Transforming growth factor β
Tie2.ERT2.Cre	Mice expressing a fusion protein of *Cre* recombinase-estrogen receptor under the control of endothelial receptor tyrosine kinase promoter
TLR2TL-2	Toll like receptor-2
TLR4/TL-4	Toll like receptor-4
TNF-α	Tumor necrosis factor α
TNFR	Tumor necrosis factor receptor
VCAM-I	Vascular cell adhesion molecule 1
VEGFR	Vascular endothelial growth factor receptor
WT	Wild type
WT-SHAM	Wild type mice without transverse aortic constriction
WT-TAC	Wild type mice with transverse aortic constriction
μg	Micro gram
μl	Micro liter
μM	Micro molar

List of Figures

List of Tables

1. Introduction

Cardiovascular diseases (CVDs), relating to heart and circulatory system, are among the leading causes of death worldwide. In developing countries, 31% of mortality rate is due to CVDs, and it has been estimated that it will become the major cause of deaths by 2020 (Stewart *et al.,* 2017). A wide spectrum of cardiac and vascular pathologies such as cardiac fibrosis, reduced angiogenesis after myocardial infarction (MI), atherosclerosis and cardiac hypertrophy are some important forms of CVDs (World Health organization report 2014-2017) (Banquet *et al.,* 2011; Carmeliet, 2005).

- Cardiac fibrosis is referred as abnormal thickening of cardiac muscles with deposition of extracellular matrix (ECM), which reduces the mechanical function of heart (Tian *et al.,* 2017). In normal cardiac function, cardiac fibroblasts maintain the ECM secretion like Collagen I and III in cardiac tissues (Nicoletti and Michel, 1999). This homeostatic balance of ECM is necessary to maintain mechanical force and electrical conductance in heart tissue (Travers *et al.,* 2016). Hypertension, hyperglycemia and ischemia effect these fibroblasts leading to transforming them into myofibroblasts which secrete altered ECM proteins, mainly high amount of Collagen I (Nicoletti and Michel, 1999). This altered ECM reduces the cardiac tissue efficiency and promotes fibrosis, which leads to cardiac failure (Nicoletti and Michel, 1999; Travers *et al.,* 2016).

- Myocardial infarction (MI), also known as heart attack, occurs when there is insufficient blood supply to cardiac tissues (ischemia) (Kobayashi *et al.,* 2017). Angiogenesis, formation of new capillaries is a response of cardiac tissue to compensate the ischemic condition (Hueso *et al.,* 2017; Kobayashi *et al.,* 2017). Reduced angiogenesis is a common pathological condition in CVDs (Kobayashi *et al.,* 2017). Prolonged ischemic conditions can lead to metabolic imbalance in ischemic tissues, which leads to cardiac failure (Hueso *et al.,* 2017). Therapeutic studies focused on improving cardiac angiogenesis after MI shows that it results in reduced risk of cardiac failure (Hueso *et al.,* 2017; Kobayashi *et al.,* 2017).

- Atherosclerosis is another common pathological condition associated with prognosis of multiple CVDs. Atherosclerosis is a disease, in which plaques develop inside the arterial walls (Verstraete, 1990; Zampetaki *et al.,* 2010). Disturbed blood flow, hypertension and high cholesterol levels in blood exerts stress on arterial wall,

which leads to endothelial cells (ECs) dysfunction (Kwak *et al.,* 2014; Zampetaki *et al.,* 2010). ECs dysfunction leads to atherosclerotic plaque development (Kwak *et al.,* 2014). Unstable plaques in atherosclerosis can rupture and activate the immune system, which develops a thrombus (Kwak *et al.,* 2014).

- Cardiac hypertrophy is defined as abnormal enlargement of cardiac muscles due to increased size of cardiomyocytes and deposition of ECM as a result of prolonged cardiac fibrosis (Hara *et al.,* 2017). Cardiac chambers, specifically left ventricle, become enlarge due to deposition of excess ECM, which leads to cardiomyocyte death (Samak *et al.,* 2016). Hypertrophic tissues become stiff and reduce the blood pumping efficiency of heart, which can lead to cardiac failure (Heineke and Molkentin, 2006; Samak *et al.,* 2016).

Among several forms of CVDs, atherosclerosis and cardiac hypertrophy are the focus of this thesis and will be discussed further in detail. Multiple environmental and biological factors contribute in the development of CVDs. Major risk factors for the development of atherosclerosis and cardiac hypertrophy can be divided into two categories: 1. Modifiable risk factors (diabetes, hypertension, elevated levels of cholesterol, obesity, and smoking) and 2. Non-modifiable risk factors (Aging, ethnicity, family history/genetic and gender).

1.1 Modifiable risk factors in CVDs

Modifiable risk factors include those factors, which are preventable and can reduce the risk of developing atherosclerosis or cardiac hypertrophy. Major modifiable risk factors are diabetes, hypertension, elevated levels of cholesterol in blood, obesity and smoking (Fig. 1.1) (Deaton *et al.,* 2011).
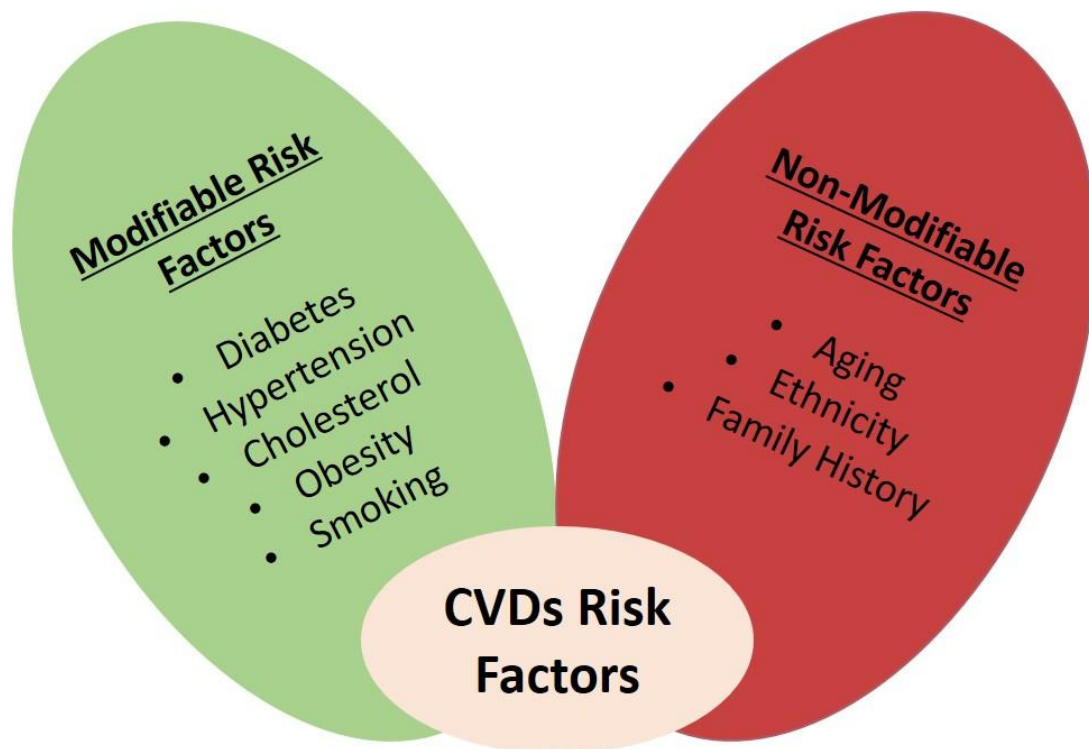
Figure 1.1. Risk Factors in CVDs. Modifiable risk factors (green) are those that can be controlled or improved. These include diabetes, hypertension, cholesterol, obesity and smoking. Non-modifiable factors (red) are those that cannot be altered like age, ethnicity and family history (Genetic contribution) of disease.

1.1.1 Diabetes

Diabetes, also known as hyperglycemia (high blood sugar level) is classified as a modifiable risk factor. Once developed, it cannot be cured completely. However controlling blood sugar levels can reduce the risk of CVDs development (Leon and Maddox, 2015). Hyperglycemia leads to glycation of cholesterol molecule, which enhances its oxidation thereby leads to ECs dysfunction and promotes CVDs (Rosiek and Leksowski, 2016). The endothelium (ECs) is not only important to maintain homeostatic balance between blood and tissues (Fig. 1.2A) (Hadi *et al.,* 2005; Messner and Bernhard, 2014), but also for non-adhesive, anticoagulant, anti-hypertrophic and anti-inflammatory functions of endothelium dependent vasodilation (Hadi *et al.,* 2005; Michaelis, 2014). Intriguingly, Insulin resistance and hyperglycemia contributes to the development of atherosclerosis and ECs dysfunction via reducing the production of endothelial Nitric Oxide Synthase (eNOS) and by enhanced production of Reactive Oxygen Species (ROS) (Leon and Maddox, 2015). The low levels of eNOS production leads to reduced ECs-dependent-vasodilation. While elevated levels

of ROS cause cell death and injury in ECs, which leads to inflammatory response and the development of CVDs (Leon and Maddox, 2015).

1.1.2 Hypertension

Hypertension, or high blood pressure, is developed by environmental and genetic factors and contributes significantly to mortality associated with CVDs. It is known that persons with hypertension have 50% more chances to develop heart diseases compared to non-hypertensive person (Huq *et al.,* 2018). Hypertension increases the risk of ECs dysfunction and atherosclerosis probably by increasing ROS production and various vasoconstrictors such as endothelin-1 (ET-I) and Angiotension II (Ang-II), production (Higashi *et al.,* 2012; Rosiek and Leksowski, 2016). Elevated levels of ROS and vasoconstrictors disrupt ECs dependent vasodilation and leads to the development of CVDs (Bleakley *et al.,* 2015; Higashi *et al.,* 2012).

1.1.3 Elevated levels of Cholesterol

Cholesterol is classified as one of the major contributing factor in CVDs development (Rosiek and Leksowski, 2016). High levels of low-density lipoprotein cholesterol (LDL-Cholesterol) and triglycerides, collectively known as dyslipidemia, impairs ECs function by perturbing the eNOS signalling pathway (Dart and Chin-Dusting, 1999; Kim *et al.,* 2012). Nitric Oxide (NO), a vasodilatory gas, derived from eNOS signalling pathway, is responsible for maintaining anti-apoptotic and anti-proliferative environment in blood vessels (Sessa, 2004). Dyslipidemia is also known to stimulate leukocyte adhesion to ECs, therefore, contributes in atherosclerosis development (Dart and Chin-Dusting, 1999). LDL-Cholesterol also contributes in progression of atherosclerotic lesions formation and is a dominating contributing molecule in lipid core of atherosclerotic lesions (Hadi *et al.,* 2005; Rosiek and Leksowski, 2016).

1.1.4 Obesity

Obesity is a multifactorial disorder, in which both genetic and environmental factors are involved (Wang and Nakayama, 2010). Obesity indirectly increases the risk for CVDs development as a result of the development of diabetes, hypertension, and high levels of cholesterol in blood (Kachur *et al.,* 2017). It has been reported that obese children have impaired contractile function and develop left ventricular hypertrophy (Jing *et al.,* 2016). Obesity leads to disruption in lipid metabolism and increases ECs dysfunction due to

increased inflammation (Lovren *et al.,* 2015). These attributes of obesity make a person more prone to develop atherosclerosis as compared to non-obese persons (Lovren *et al.,* 2015).

1.1.5 Smoking

Smoking is directly linked to multiple diseases like lung cancer, ischemia, atherosclerosis, endothelial dysfunction, hypoxemia, and thrombosis (Hadi *et al.,* 2005). Smoking impairs the balance between endothelium specific vasoconstrictor and vasodilatory chemical production (Messner and Bernhard, 2014; Michael Pittilo, 2000). Smoking has been also reported as a contributing factor in lipid profile alteration and to increase the expression of adhesion molecules on ECs and reduce eNO production, which leads to endothelial dysfunction and atherosclerosis development (Messner and Bernhard, 2014).

1.2 Non-modifiable Risk factors in CVDs

Non-modifiable risk factors are those, which cannot be controlled or modified. These include Aging, ethnic background and family history.

1.2.1 Aging

Age is an independent risk factor that increases the risk of CVDs development in together with other risk factors such as diabetes, hypertension and high cholesterol levels (Dhingra and Vasan, 2011). Advanced age is associated with cellular senescence of ECs, loss of blood vessels elasticity (Hadi *et al.,* 2005; Stewart *et al.,* 2017) higher ROS production, which results in endothelial dysfunction and loss of ECs vasodilation ability (Higashi *et al.,* 2012; Matz and Andriantsitohaina, 2003).

1.2.2 Ethnic background

It has been reported that South Asian population has higher risk of CVDs development as compared to European population. This is mainly due to life style differences, which lead to the development of diabetes, high LDL-Cholesterol levels and hypertension (Chaturvedi, 2003). Mexicans and African Americans are also reported to have higher risk of CVDs development (Chaturvedi, 2003; Forouhi and Sattar, 2006).

1.2.3 Family History/Genetic factor

Linkage analysis and genetic association studies have been one of a successful approach in determining CVDs development (Kathiresan and Srivastava, 2012). Risk of developing

CVDs increases if first-degree and second-degree relatives are affected (Imes and Lewis, 2014). Risk of atherosclerosis development increases up to 3-fold if parents are atherosclerotic (Kathiresan and Srivastava, 2012). There is a 40% higher chance of CVDs development if a sibling is affected, while children of CVDs patients have 75% higher chance of developing CVDs (Imes and Lewis, 2014; Kolber and Scrimshaw, 12014).

Taken together, all the above-mentioned factors independently and synergistically contribute in the development of CVDs, including atherosclerosis and cardiac hypertrophy (Hadi *et al.,* 2005; Rosiek and Leksowski, 2016).

1.3 Atherosclerosis

Atherosclerosis refers to the thickening of arterial wall, which occurs due to the accumulation of lipids and fibrous materials in major arteries. Mostly the branched areas, which are exposed to disturbed blood flow are more prone to plaque development (Chien, 2008; Zampetaki *et al.,* 2010). There are three main layers in artery (Fig. 1.2A). The tunica intima is the inner most layer that is lined by monolayer of ECs. The middle layer, tunica media, mainly consists of smooth muscle cells (SMCs) that are embedded in ECM. The outer most layer, adventitia, contains fibroblasts, micro vessels, mast cells and nerve endings (Fig. 1.2A) (Chien, 2008; Libby, 2000; Zampetaki *et al.,* 2010). The accumulation of lipids and fibrous material occurs mostly at branched areas, which are exposed to disturbed blood flow and ultimately leads to activation of pro-inflammatory signalling pathways (Chien, 2008). Lipid accumulation is also associated with higher apoptotic activity of ECs, reduced eNOS production, increased ROS production and responsible for increased permeability of ECs, which eventually leads to endothelial dysfunction and atherosclerosis (Zampetaki *et al.,* 2010). Atherosclerotic lesion development starts with accumulation of monocytes into intima due to endothelial dysfunction.

1.3.1 Stages of Atherosclerosis

Atherosclerosis can be divided into following stages

1. Endothelial dysfunction

2. Migration and maturation of monocytes

3. Plaque formation

4. Thrombosis
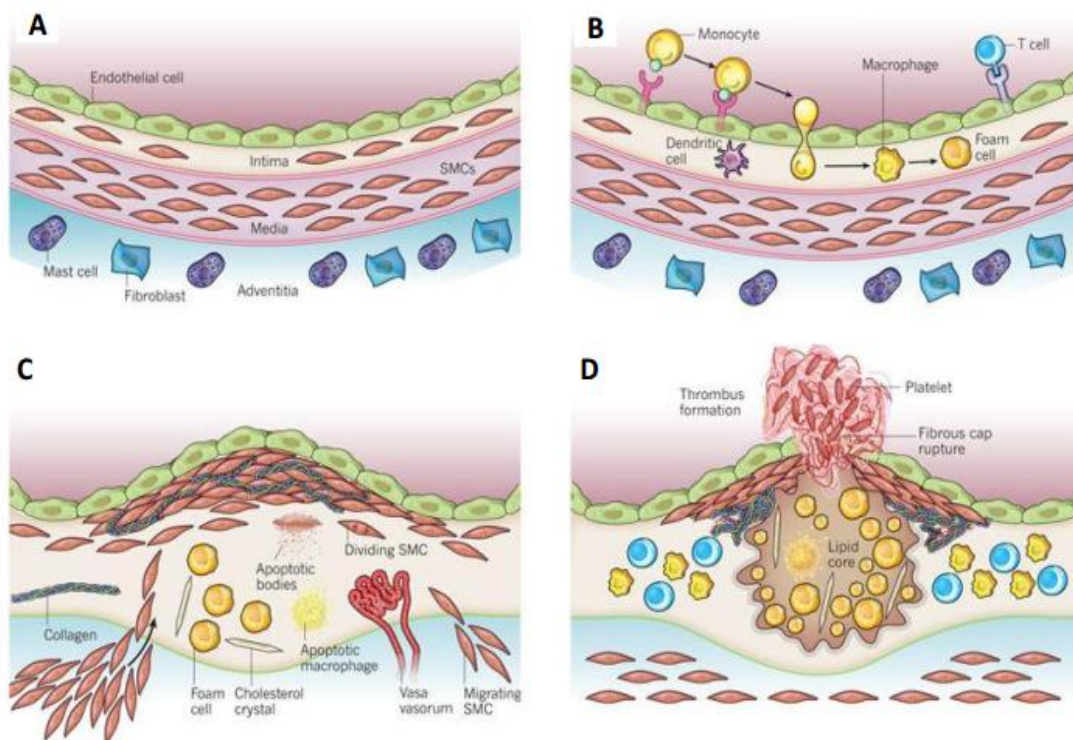
Figure 1.2. Stages of Atherosclerosis. A. The innermost layer of artery is lined by ECs, which maintain the homeostatic balance between blood and artery. Middle layer consists mainly of SMCs, while the outer most layer contains nerve cell endings, fibroblast cells and mast cells. **B.** Inflammatory response leads to activation of ECs, which primes binding of monocytes to ECs, and their migration into intima. Inside intima, monocytes mature into macrophages, take up lipid molecules, and form foam cells. **C.** SMCs along with collagen fibers migrate to intima and make thick fibrous cap. Lipid molecules accumulate in centre of the plaque and form lipid core. **D.** Plaque cap ruptures due to disturbed blood flow, which triggers the immune response, and a thrombus is formed. Thrombus can block the artery partially or completely. (Figure published by Libby *et al.,* 2011).

1.3.1.1 Endothelial Dysfunction

Endothelium is important to maintain homeostatic balance between blood and tissues (Fig. 1.2A) (Chien, 2008; Zampetaki *et al.,* 2010). Different environmental factors and signalling pathways are involved in protection and activation of ECs. Increased levels of homocysteine, LDL, micro-organisms, smoking and diabetes are considered as triggering factors of ECs dysfunction (Hadi *et al.,* 2005; Higashi *et al.,* 2012; Hueso *et al.,* 2017; Messner and Bernhard, 2014). Cytokines like interleukin-1β and tumor necrosis factor α (TNF-α) are responsible for the initiation of ECs dysfunction by activating nuclear transcription factor κB (NF-κB) and protein kinase C pathways (Brown *et al.,* 2014; Xiao *et al.,* 2014). NF-κB is a key regulator of inflammation during atherosclerosis (Brown *et al.,* 2014). Activation of NF-κB leads to translocation of NF-κB from cytoplasm to the nucleus, which initiates transcription of downstream target genes including cytokines, chemokines and adhesion molecules like E-Selectin (*SELE*) and Vascular Cell Adhesion Molecule 1

(*VCAM-1*) (Gerhardt and Ley, 2015). ECs express adhesion molecules on their surface, which starts interacting with different blood cells like monocytes.

1.3.1.2 Migration and maturation of Monocytes

Migration of monocytes into intima is a multistep process that involves capturing of monocytes on activated ECs, slow rolling on the surface of ECs, firm binding to ECs and then migration into intima (Gerhardt and Ley, 2015). SELE mediates the capturing and slow rolling of monocyte and T-cells on ECs, while VCAM-1 is responsible for firm adhesion of leukocytes on ECs, which facilitates its migration into intima (Fig. 1.2B) (Gerhardt and Ley, 2015; Libby, 2000). Migrated monocytes mature into macrophages, which fuse with lipoproteins to make foam cells (Gerhardt and Ley, 2015; Libby, 2000).

1.3.1.3 Plaque Formation

Foam cells accumulate to make a lipid core of lesion. SMCs migrate from tunica media to intima and accumulate in lesions along with cellular and ECM like collagen, proteoglycans, and elastin and form thick fibrous cap (Gerhardt and Ley, 2015; Libby, 2000; Xiao *et al.,* 2014). The lesion protected by this thick fibrous cap is referred as atheroma or atherosclerotic plaque. Central lipid core of plaque, known as necrotic core, consists mainly of lipid molecules and cholesterol crystals (Fig. 1.2C) (Libby, 2000).

1.3.1.4 Thrombosis

Atherosclerotic plaques are of two types stable and unstable, based on their composition (Falk, 1992). Stable plaques are rich in ECM and SMCs and have thick stable cap. While unstable plaques are rich in soft extracellular lipids and highly infiltrated with foam cells leading to be more prone to rupture (Falk, 1992). Fibrous cap of unstable plaques ruptures due to physical abrasion from blood flow and activates acute thrombosis response that can lead to blood coagulation and thrombus formation (Fig. 1.2D). Thrombus can extend ,restrict the lumen of the artery, and can cause further complications like angina, myocardial infarction, dysrhythmia and sudden cardiac arrest (Libby, 2000). Atherosclerosis reduces the normal blood flow, which can cause cardiac arrest and death.

1.3.2 Signalling Pathways and transcription factors involved in Atherosclerosis

Atherosclerosis is categorized as an inflammatory disease. Inflammation is the important step in initiation and progression of plaque formation (Conti and Shaik-Dasthagirisaeb, 2015). Multiple signalling pathways have been identified as regulators of inflammation such as mitogen activated protein kinases (MAPKs), signal transducer activator of transcription

(STAT), Janus-Kinase (JAK) and NF-κB (Montecucco *et al.,* 2012; von der Thusen *et al.,* 2003). Among these signalling pathways, NF-κB is the main signalling pathway of inflammation (Hajra *et al.,* 2000; Xiao *et al.,* 2014).
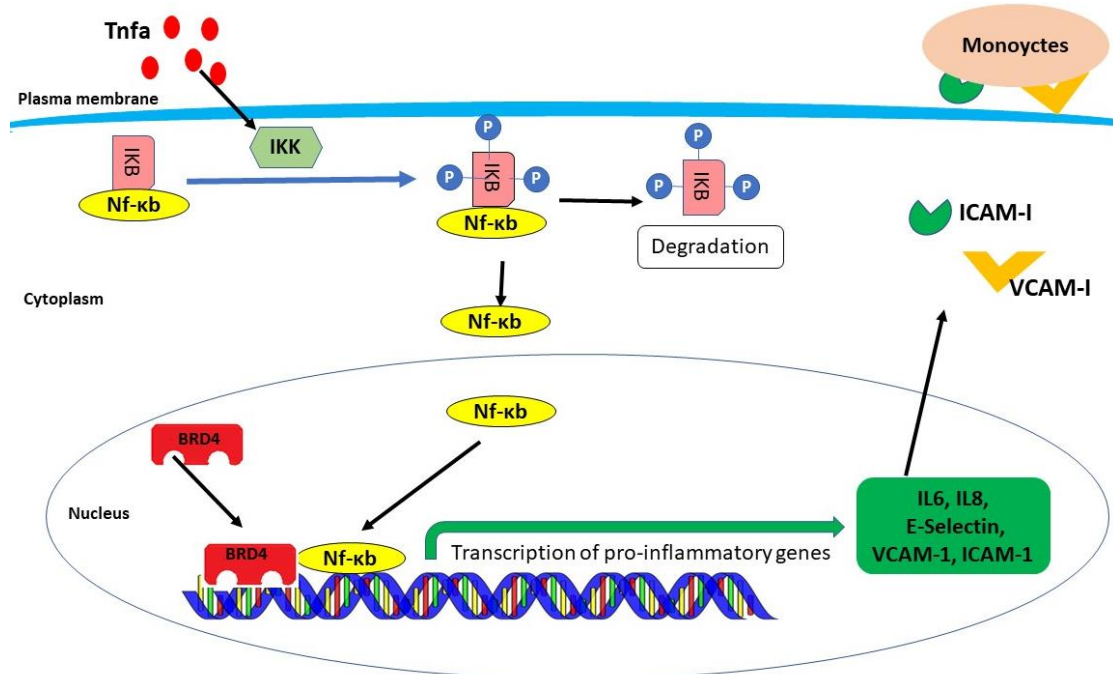
Figure 1.3. NF-κB Signalling pathway. NF-κB heterodimer (RelA and p50) is present in cytoplasm bound with IκB-α in an inactive state. When there is an inflammatory signal, IKK is activated and phosphorylates the IκBα, which is then degraded by the proteasome assembly. The activated NF-κB dimer migrates into the nucleus and binds to chromatin and initiates the transcription of inflammatory markers (E-Selectin, VCAM-I, ICAM-I, IL6, IL8). Adhesion molecules (VCAM-I, ICAM-I) are expressed on activated ECs and binds to monocytes.

Activation of NF-κB pathway is reported in multiple inflammatory diseases like Rheumatoid arthritis, atherosclerosis, multiple sclerosis, asthma and inflammatory bowel disease (Tak and Firestein, 2001). NF-κB is a heterodimer consisting of p50 and p65 (RelA) subunits. In resting state ECs, NF-κB binds to its inhibitor (IκB-α), which keeps NF-κB in an inactive form (Tanaka and Iino, 2016; Xiao *et al.,* 2014). Central step of NF-κB cascade is liberation of NF-κB from IκB-α. Inflammatory mediators like TNF-α, lipopolysaccharides (LPS) and Interleukin-1 (IL-1) binds to toll like receptors (TL4, TL2) on plasma membrane and activates IκB-Kinase (IKK) (Monaco and Paleolog, 2004). IKK phosphorylates IKB-α, which is subsequently ubiquitinated and degraded by proteasome assembly, and liberates NF-κB for nuclear translocation (Monaco and Paleolog, 2004; Xiao *et al.,* 2014). Inside the nucleus, NF-κB interacts with different chromatin modifiers (Histone deacetylases - HDACs, p300, BRD4), transcription factors (c-Myc, p53) and binds to enhancer regions of approximately 400 genes to induce their expression (Fig. 1.3) (Tanaka and Iino, 2016).

Multiple pro-inflammatory genes such as cytokines Interleukin 6 and 8 (IL6, IL8), TNF-α and adhesion molecules like SELE, Intercellular Adhesion Molecule 1 (ICAM-1), VCAM-1, which contribute for progression of inflammation and ECs dysfunction are all activated via NF-κB signalling pathway (Tanaka and Iino, 2016; Xiao *et al.,* 2014). Among the regulatory partners of NF-κB, Bromodomain containing protein 4 (BRD4), a chromatin modifier has been recently highlighted more due to its important role during inflammation and in atherosclerosis (Picaud *et al.,* 2013; Xu and Vakoc, 2014b).

1.3.3 Role of BRD4 in atherosclerosis

NF-κB interacting partners include different transcription factors and chromatin modifiers including BRD4 (Tanaka and Iino, 2016). BRD4, an epigenetic regulator, is a member of BET (Bromodomain and extra terminal domain) tandem bromodomain containing family. BET family members contain two N-terminal bromodomains, Bromodomain 1 (BD1) and Bromodomain 2 (BD2) and an Extra terminal (ET) domain (Najafova *et al.,* 2017). BRD4 is known for its role in multiple cellular activities like inflammation, DNA damage repair, spermatogenesis, and cell cycle (Devaiah *et al.,* 2016; Devaiah *et al.,* 2012; Najafova *et al.,* 2017). It is also involved in transcription of oncogenes (Crowe *et al.,* 2016; Najafova *et al.,* 2017). BRD4 has both histone acetyl transferase (HAT) and kinase activity (Devaiah *et al.,* 2016; Devaiah *et al.,* 2012). BRD4 recognizes and binds to acetylated lysine residues of histone proteins, H3 (H3K14 - histone 3 lysine 14) and H4 (H4K5 - histone 4 lysine 5 or H4K12 - histone 4 lysine 12) via BD1 and BD2 (Devaiah *et al.,* 2016).
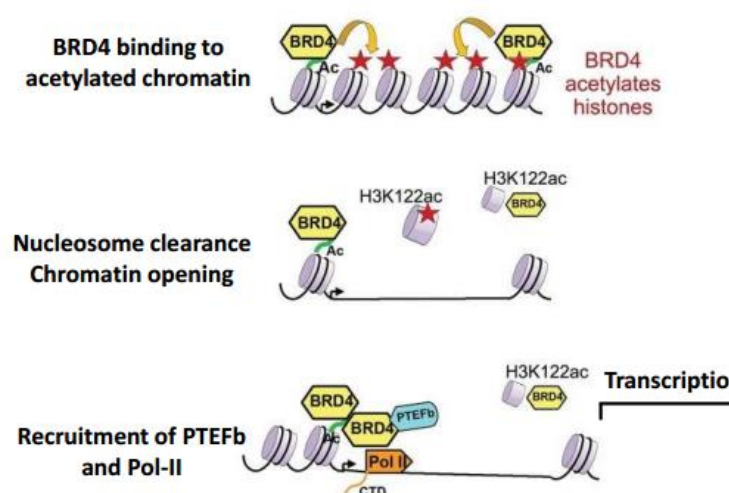
Figure 1.4. Binding of BRD4 on chromatin and acting as HAT and Kinase. BRD4 protein binds to the acetylated chromatin and acetylates histones, leading to DNA-Histone disassembly and opening of chromatin. BRD4 recruits positive transcription elongation factor (P-TEFb) and RNA polymerase 2. BRD4 also acts as atypical kinase and phosphorylates CTD of RNA-Pol II to initiate transcription of target genes (Figure is published by Devaiah *et al.,* 2016).

After binding to chromatin, BRD4 acetylates the core of histones at H3K122 residue and leads to nucleosome (histone-DNA complex) disassembly (Fig. 1.4), followed by recruitment of RNA Polymerase II (RNA Pol-II) (Devaiah *et al.,* 2016). Then C-terminal end of BRD4 protein recruits positive transcription elongation factor (P-TEFB) (Crowe *et al.,* 2016; Devaiah *et al.,* 2012). It has been reported that BRD4 phosphorylates the Serine residue at position 2 (Ser2) of Carboxy-terminal domain (CTD) of RNA Pol-II ensuring proper transcriptional initiation and elongation (Fig. 1.4) (Crowe *et al.,* 2016; Devaiah *et al.,* 2012).

Among the BET protein family members, BRD4 has higher expression in ECs than other BET proteins (Huang *et al.,* 2016). There are two naturally existing splice variants/isoforms of *BRD4* known as *BRD4 Long* (*BRD4-L*) and *BRD4 short* (*BRD4-S*) (Alsarraj *et al.,* 2013; Alsarraj *et al.,* 2011; Crawford *et al.,* 2008). Both BRD4-L and BRD4-S proteins share the same N-terminal region except for last three amino acids, while the C terminal domain is absent from BRD4-S isoform (Fig. 1.5) (Chiang, 2009). BRD4 isoforms have been reported to act antagonistically in breast cancer progression, where the BRD4-L isoform reduces cancer metastasis, while the BRD4-S enhances the cancer metastasis (Alsarraj *et al.,* 2013). Moreover, BRD4-S isoform is overexpressed in colon cancer cell lines (Alsarraj *et al.,* 2011).

Figure 1.5. Human BRD4 protein isoforms structure. The long isoform of human BRD4 (hBRD4-L) is 1362 amino acid long (152kDa), while the short isoform of human BRD4 (hBRD4-S) is 722 amino acid long (80kDa). Both isoforms share similarity in structure concerning bromodomain I (BDI), bromodomain II (BDII) and an extra terminal domain (ET). However, the long isoform has extra C-terminal region (CTM) which is absent in short isoform.

The evidence that BRD4 has influence on inflammatory response, specifically in atherosclerosis, came up in 2013. In this year, two independent studies revealed that BRD4 was inhibited by a chemical compound, RVX-208, that was already tested for treatment of atherosclerosis by enhancing HDL components APO-A1, but whose exact molecular target till then remained unclear (Picaud *et al.,* 2013; Xu and Vakoc, 2014b). RVX 208 is in clinical

trials for treatment of diseases like atherosclerosis, Diabetes, Alzheimer's disease, and chronic kidney disease (Drugs.R.D, 2011; McLure *et al.,* 2013; Vidler *et al.,* 2013).

After identifying BRD4 as a target of RVX208, much research was done to identify the exact contribution of BRD4 to atherosclerosis as well as to other inflammatory diseases. In quiescent ECs, BRD4 is known to interact with super enhancers (SEs) of genes that encode for proteins with basal cellular functions (Fig. 1.6). As described above, TNF-α mediated inflammatory stimuli results in the translocation of the NF-kB from cytoplasm to nucleus, which enhances the transcription of pro-inflammatory genes (Brown *et al.,* 2014). Recent studies have uncovered that upon activation of NF-κB, BRD4 redistributes on chromatin from SEs of resting state genes to SEs of pro-inflammatory genes along with NF-κB (Drugs.R.D, 2011; McLure *et al.,* 2013; Xu and Vakoc, 2014b). BRD4 interacts with acetylated Lysine residue (Lysine-310) of the RelA subunit of NF-kB (Huang *et al.,* 2009). NF-κB and BRD4 have been reported to initiate an inflammatory response through up regulation of adhesion molecules and inflammatory cytokines (Fig. 1.6). Chromatin immunoprecipitation (ChIP) with massively parallel DNA sequencing (ChIP-seq) studies on ECs reported that SEs and promoter regions of 271 genes were enriched for RelA and BRD4 after inflammatory stimuli including *SELE* and *VCAM1* (Brown *et al.,* 2014; Xu and Vakoc, 2014b).
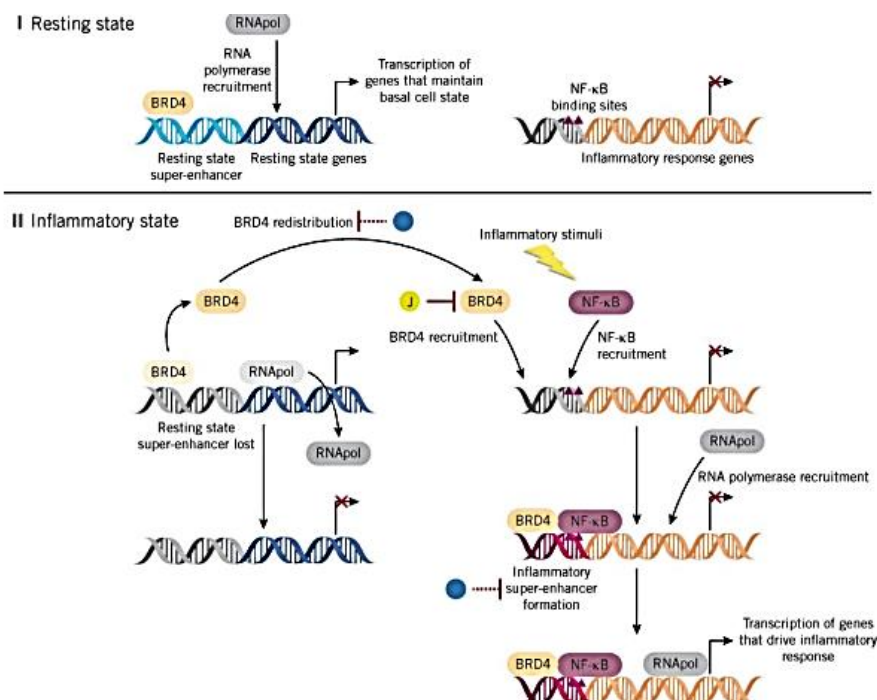
Figure 1.6. Redistribution of BRD4 on chromatin during Inflammatory stimulus. I in normal resting state ECs, BRD4 binds to SEs of resting state genes. II During inflammatory state, BRD4 redistributes on chromatin and bind to SEs of pro-inflammatory genes along with NF-κB. (Figure published by Lou *et al.,* 2014).

1.4 Cardiac Hypertrophy

Cardiac hypertrophy is characterised by thickening and enlargement of heart muscles and shortening of ventricular chambers (Tardiff, 2006). Cardiac hypertrophy occurs due to inflammation and cardiomyocyte growth exceeding the capacity of capillaries to sufficiently supply nutrients and oxygen thus, leading to cardiac hypoxia and cardiomyocytes death. Furthermore, deposition of ECM and fibrosis leads to reduced blood pumping ability of heart (Shimizu and Minamino, 2016; Tardiff, 2006). There are two types of cardiac hypertrophy namely physiological and pathological hypertrophy, which are developed due to extra work load on heart (Tardiff, 2006). Physiological hypertrophy develops in response to pregnancy and excessive exercise, in which cardiac function is enhanced to fulfil the energy demand (Shimizu and Minamino, 2016). Pathological hypertrophy is characterised by myocardial dysfunction, change in sarcomeric structure, hypertrophic and fibrotic ventricle (Fig. 1.7) (Samak *et al.,* 2016).
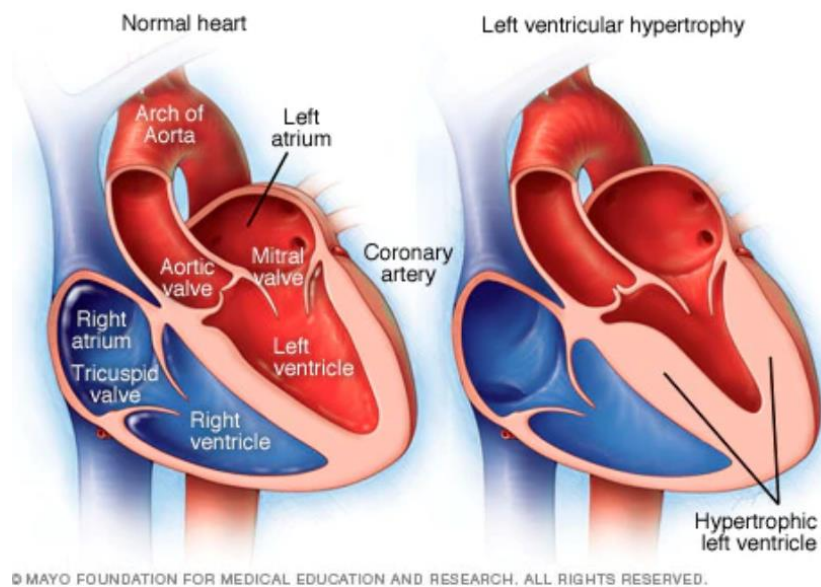
Figure 1.7. The structure of a normal and cardiac hypertrophy heart. The structure of a normal heart (left) with a normal left ventricular size is shown. The structure of a left ventricular hypertrophic heart (right) showing reduced size of ventricular chamber due to increased fibrosis, increased size of cardiomyocytes and deposition of ECM. (Figure published by Mayo foundation for medical education and research https://www.mayoclinic.org/diseases-conditions/hypertrophic-cardiomyopathy/symptoms-causes/syc-20350198).

Multiple pathological conditions such as hypertension, valvular defects, ischaemia, coronary artery disease and diabetes, which increase the energy demand are responsible for the development of cardiac hypertrophy (Heineke and Molkentin, 2006). Initially, cardiac hypertrophy is a compensatory mechanism in response to increased work demand due to

mechanical and biochemical stress. During this phase, cardiomyocytes become enlarge and increase protein synthesis along with increase in cardiac fibroblasts proliferation (Heineke and Molkentin, 2006). Cardiac fibroblasts, under stress conditions, change their morphology between fibroblast and SMCs and are known as myofibroblasts (Manabe *et al.,* 2002). Myofibroblast cells produce inflammatory chemokines, cytokines and play a significant role in the development of inflammation in hypertrophic heart (Manabe *et al.,* 2002). Prolonged hypertrophy results in cardiac cell death and leads to fibrosis, a condition in which collagen fibres deposits in ventricular chambers, stiffens the ventricles and reduced the contraction and relaxation of heart (Carreno *et al.,* 2006; Manabe *et al.,* 2002). Increased fibrosis leads to reduced oxygen diffusion, which create hypoxic environment resulting in cardiac cell death (Manabe *et al.,* 2002). Stiffness of cardiac tissues and apoptotic conditions leads to impaired cardiac functions (Talman and Ruskoaho, 2016).

1.4.1 Signalling Pathways in Cardiac Hypertrophy

Multiple proteins and signalling pathways are known to act as stimulus for cardiac hypertrophy. Activated signalling pathways in physiological and pathological hypertrophy are different. In **physiological hypertrophy**, fibroblast growth factors (FGF), Ang II, insulin growth factors (IGF) and transforming growth factor β (TGFβ) activate tyrosine kinase receptors, which further on initiate the phosphoinositol-3-kinase (PI3K) and mammalian target of rapamycin (mTOR) signalling pathways (Fig. 1.8) (Samak *et al.,* 2016). The activation of these signalling pathways leads to increased protein synthesis to compensate work load (Samak *et al.,* 2016).

On the other hand, in **pathological hypertrophy** activated signalling pathways include MAPKs and JAK, which activate the transcription of maladaptive genes responsible for hypertrophic growth (Carreno *et al.,* 2006; Samak *et al.,* 2016). G-protein-coupled receptors (GPCRs) are also activated in pathological hypertrophy through Ang-II, ET-I (Carreno *et al.,* 2006; Samak *et al.,* 2016). GPCRs activate multiple downstream transcription factors, specifically NF-κB and nuclear factor of activated T cells (NFAT) (Fig. 1.8) (Samak *et al.,* 2016). GPCRs activate voltage-gated calcium ion channels, which leads to elevated levels of calcium ions (Ca^{+2}) inside cardiomyocytes (Carreno *et al.,* 2006; Samak *et al.,* 2016). Increased Ca^{+2} levels are detected by calmodulin (Cam), which leads to dephosphorylation and nuclear translocation of NFAT via activation of calcineurin A and B (CnA, CnB) (Fig. 1.8) (Samak *et al.,* 2016).
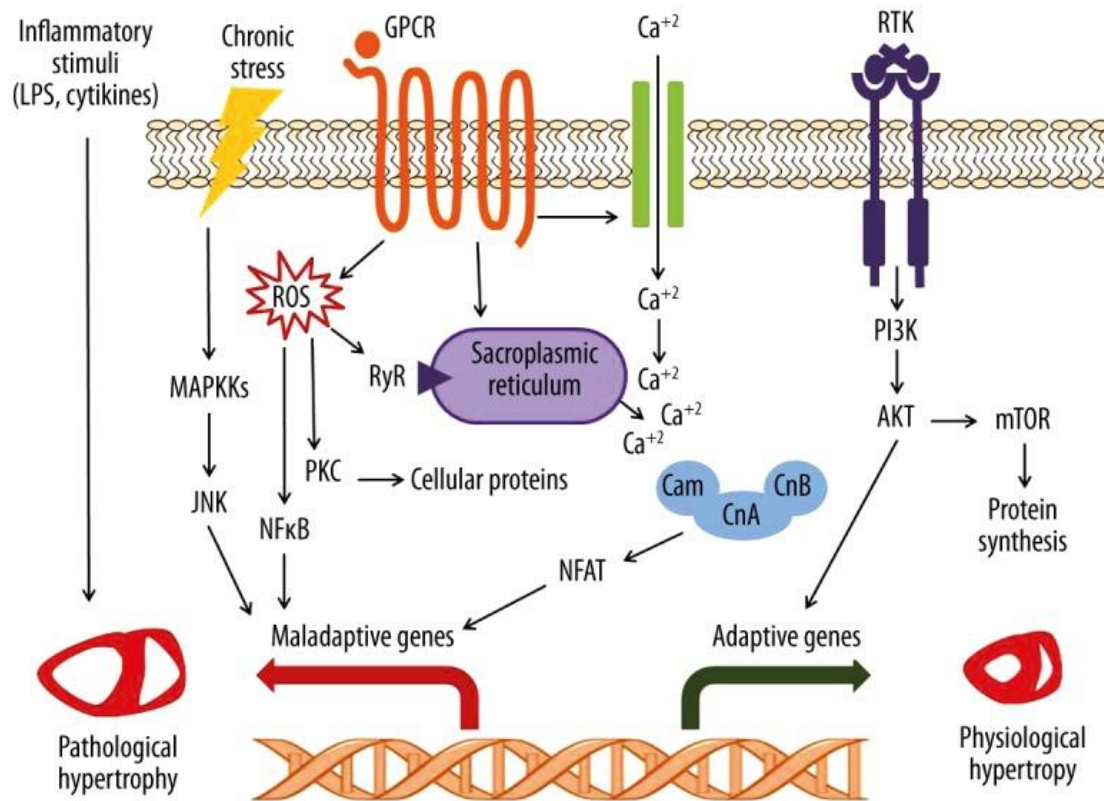
Figure 1.8. Signalling pathways in Cardiac hypertrophy. PI3K and mTOR signalling pathways are activated in physiological hypertrophy while MAPKs, JNK, NFAT and NF-κB are involved in the development of pathological cardiac hypertrophy. (Figure published by Samak *et al.,* 2016)

ROS also contributes to cardiac hypertrophy by inducing apoptosis and activating NF-κB signalling pathway (Fig. 1.8) (Samak *et al.,* 2016). Activation of NF-κB signalling pathway and inflammatory cytokines expression, such as IL6, TNF-α and IL-1β, is a hallmark of hypertrophy (Carreno *et al.,* 2006; Samak *et al.,* 2016). The role of NF-κB signalling pathway is not clearly understood, however it is known that it enhances the infiltration of inflammatory cells such as macrophages and T-cells during fibrosis (Samak *et al.,* 2016). Among the targets of NF-κB signalling pathway, Protein Tyrosine Phosphatase 1B (PTP1B) is a protein, reported to have higher expression during inflammation (Zabolotny *et al.,* 2008).

1.4.2 PTP1B

Protein kinases, which are responsible for phosphorylations at serine, tyrosine, threonine, and lysine residues, constitute one of the largest enzyme family encoded by human genome (Manning *et al.,* 2002). Tyrosine phosphorylation is required for activation of receptor tyrosine kinases (RTKs), while protein tyrosine phosphatases (PTPs) are negative regulators of this activation. PTPs were first identified in 1988 when, PTP1B was purified from human placenta (Tonks *et al.,* 1988). The PTP family of enzymes have four classes, classes I, II and III are known as cysteine-based PTPs, whereas class IV is known as aspartate-based PTPs (Alonso *et al.,* 2004; Low *et al.,* 2014). The class I PTPs are further divided into two subgroups namely transmembrane- or receptor-type PTPs and the intracellular PTPs (Barr, 2010). The first intracellular PTP to be purified and characterized was PTP1B (Tonks *et al.,* 1988).

PTP1B has three major domains on the basis of structure and function. The N-terminal catalytic domain is responsible for the phosphatase activity of the enzyme and two flanking Proline rich domains are responsible for protein-protein interactions, while the C-terminal ER targeting domain anchors the enzyme to endoplasmic reticulum (ER) (Fig. 1.9) (Yip *et al.,* 2010).
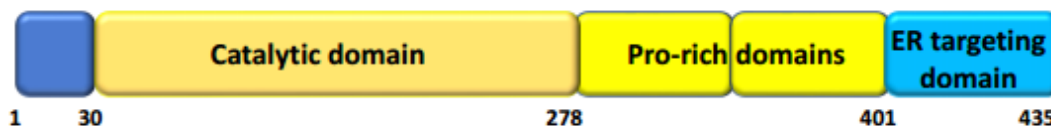
Figure 1.9. Domain architecture of PTP1B. The PTP1b enzyme has three major structural domains namely: **Catalytic domain-** the main central domain of the enzyme; **Proline rich domain-** responsible for binding of enzymes to its targets; and **ER targeting domain-** responsible for attachment of enzyme to ER.

Expression of PTP1B is induced by TNF-α both *in vivo* and *in vitro* (Panzhinskiy *et al.,* 2013; Zabolotny *et al.,* 2008). Multiple substrates of PTP1B have been identified and the prominent ones are insulin receptor tyrosine kinase, leptin signalling and vascular endothelial growth factor receptor (VEGFR) (Lanahan *et al.,* 2014; Nakamura *et al.,* 2008). Multiple studies have shown that *Ptp1b*-knockout (*Ptp1b*-KO) mice have higher insulin sensitivity, resistant to weight gain even when fed with high fat diet, and have lower level of triglycerides in blood, which is due to higher leptin sensitivity (Elchebly *et al.,* 1999; Tamrakar *et al.,* 2014). Neuronal *Ptp1b* KO mice are resistant to obesity and have higher

physical activities, as compared to wild type mice, which become obese and slow, showing that leptin action is controlled by neuronal PTP1B (Bence *et al.,* 2006). Pre-natal and post-natal angiogenesis is a crucial biological process for the development of blood vessels and in wound healing (Ambler *et al.,* 2001; Dormond *et al.,* 2001; Isogai *et al.,* 2001). VEGFR2, a tyrosine kinase receptor, is mainly involved in ECs migration during angiogenesis (Holderfield and Hughes, 2008; Lamalice *et al.,* 2007). Interestingly, PTP1B is a negative regulator of VEGFR2 signalling in ECs (Lanahan *et al.,* 2014; Nakamura *et al.,* 2008). Both *in vivo* and *in vitro* studies showed that inhibition of PTP1B function enhances ECs migration and angiogenesis (Besnier *et al.,* 2014; Lanahan *et al.,* 2014).

It has been confirmed that overexpression of PTP1B results in inhibition of VEGFR2 phosphorylation, while endothelial-specific deletion of PTP1B (Endo.*Ptp1b*.KO) improves VEGF signal transduction (Lanahan *et al.,* 2014; Nakamura *et al.,* 2008). Genome wide gene expression analysis has confirmed the enhanced expression of PTP1B in case of high cardiac afterload (Toischer *et al.,* 2010). Long term application of PTP1B inhibitor or short hairpin RNA (shRNA) mediated inhibition in mice improves angiogenesis, ECs function and reduces cardiac remodelling, making PTP1B as a promising new target to treat CVDs (Gomez *et al.,* 2012).

Previous studies used systemic pharmacological inhibition or genetic deletion of *Ptp1b* in mice model, which protects the mice from heart failure after MI and improves ECs dysfunction. However, this inhibition or deletion can affect other cell types (cardiomyocytes, fibroblasts) in cardiac remodelling. Therefore, role of ECs remained unclear. To overcome this problem, ECs specific *Ptp1b* KO (Endo.*Ptp1b*.KO) mice were generated (Gogiraju *et al.,* 2016). These mice, upon cardiac overload by transverse aortic constriction (TAC), showed reduced oxidative stress, cardiac hypoxia, fibrosis, enhanced angiogenesis, which resulted in improved survival. In this regard, it is interesting to identify novel proteins/pathways, which are involved in PTP1B deficient hearts to device efficient therapies for CVDs.

1.5 Aims of the study

The present study is designed to better understand the role of BRD4 and its isoforms in ECs during inflammation by using *in-vitro* model of Human umbilical cord derived vascular endothelial cells (HUVECs). The aim is to investigate role of BRD4 isoforms in heart tissues of mice models of aging and cardiac hypertrophy. Moreover, we want to investigate role of BRD4 in monolayer integrity of ECs during inflammation. We also want to analyse PTP1B expression during inflammation and identify the possible mechanism responsible for cardio protection in Endo.*Ptp1b.*KO hearts using proteomics approach.

2. Materials and Methods

2.1 Cell Culture

All *in-vitro* experiments were performed using primary Human Umbilical cord derived Vascular Endothelial Cells (HUVECs) under sterile conditions. HUVECs were purchased from Promo Cell and cultured using growth medium prepared by mixing Endothelial cells basal medium (Promo Cell) and Endothelial Cell Growth Medium Supplement Pack (Promo Cell), 1% Penicillin/Streptomycin (Sigma). Cells were cultured on 0.2% Gelatin coated flasks/plates at 37°C in a humidified incubator with 5% CO_2. For trypsinisation, cells were washed with DDPBS (PAN-Biotechnologies) and incubated in Trypsin-EDTA (Gibco) at 37°C for 3-5 min. Trypsin activity was inhibited with DMEM medium (PAN-Biotechnologies) containing 10% FCS (Gibco) and 1% Penicillin/Streptomycin. Trypsin was removed by centrifugation at 1000 x g for 5 min. Cells were resuspended in growth medium and transferred to a new flask. Cell counting was performed, when necessary, by using Neubaeur improved chamber. The cells which are at passages between 7 and 9 were used for all the experiments. 5×10^4 cells/cm^2 were used for all treatments unless otherwise stated.

2.2 Treatments

2.2.1 TNF-α treatment

Human recombinant TNF-α (Peprotech) stock solution (2.5 µg/ml) was prepared in 0.1% BSA solution. Cells were treated with 20 ng/ml of TNF-α for 2 hrs, then washed with DPBS before fixation or trypsinisation.

2.2.2 JQ1 treatment

5 mg of Bromodomain Inhibitor JQ1 (ApexBio technologies) was dissolved in 109.41 µl DMSO (Sigma) to prepare a stock solution of 100 µM. Cells were treated with 500 nM JQ1 for 4 hrs or 12 hrs depending upon experimental set up. Control cells were treated with equal volume of DMSO, then washed with DPBS before fixation or trypsinisation.

2.2.3 RVX208 treatment

5 mg of Bromodomain inhibitor RVX208 (ApexBio technologies) was dissolved in 1 ml of DMSO (Sigma) to prepare a stock solution of 13.498 mM. Cells were treated with 50-, 100-

, 150- and 200-µM RVX208 for 4 hrs or 30- and 60-µM 12 hrs depending upon experimental set up. Control cells were treated with equal volume of DMSO, then washed with DPBS before fixation or trypsinisation.

2.2.4 Claramine treatment

5 mg of PTP1B inhibitor Claramine trifluoroacetate salt (Sigma) was dissolved in 1 ml of water to prepare a stock solution of 8.49 mM. Cells were serum starved for 2 hrs in ECs medium in absence of serum followed by treatment with 10-, 50- and 100-µM of Claramine for 30 mins, then washed with DPBS before fixation or trypsinisation.

2.3 Immunofluorescence staining of HUVECs

Cells were grown on small cover slips coated with 0.2% Gelatin and treated, as indicated. After completion of the experiment, the culture media was removed, and cells were washed with DPBS. Cells were fixed with 4% PFA for 30 mins. followed by washing with DPBS 2 times for 10 min each (2 X 10 min). Afterwards, blocking was done with 50 mM Ammonium Chloride (NH$_4$Cl) for 10 min at room temperature (RT). Cells were washed (3 X 4 min) with permeabilization buffer (0.2% Triton X-100 (Sigma) in DPBS) followed by incubation at RT with anti NF-κB antibody (cell signalling) prepared at 1:100 dilutions in permeabilization buffer. After 1 hr of incubation, cells were again washed 3 X 4 min each with permeabilization buffer. Afterwards, cells were incubated with 1:300 diluted secondary antibody, anti-rabbit IgG conjugated with Alexa 488 (Life Technologies), for 1 hr at RT followed by washing again with permeabilization buffer (3 X 4 min) to remove excessive antibody. Finally, cells were washed twice with DPBS and mounted with 4`,6-Diamidino-2Phenylindole, Dihydrochloride (DAPI) (Vector Laboratories). Fluorescent cells were visualised using Axiovert 200M confocal Microscopy (Carl Zeiss).

2.4 RNA expression analysis

2.4.1 RNA extraction from Cells/Tissues

For total RNA extraction, Trizol (Invitrogen) was used according to manufacturer's instructions. Briefly, HUVECs were treated, washed with DPBS twice and then harvested by trypsinization. 500 µl of Trizol reagent was added/ 10 cm^2 and cells were homogenized by vortexing, and total RNA was precipitated using chloroform/isopropanol extraction

method (Rio *et al.,* 2010). RNA was washed with 70% Ethanol and air dried, then dissolved in Diethylpyrocarbonate (DEPC) (Sigma) treated dH_2O and stored at -80°C. RNA was quantified using NanoDrop 2000C (PeqLab, ThermoFisher Scientific).

RNA extraction form mice heart tissues was done by pulverizing the tissue in liquid nitrogen using conventional mortar and pistol. Afterwards, pulverized tissues were dissolved in Trizol using a tissuelyser bead mill (Qiagen). The remaining RNA extraction protocol was as described above.

2.4.2 cDNA synthesis

cDNA was prepared by using SuperScript™ IV First-Strand Synthesis System (Invitrogen). DNase digestion was performed on total RNA before cDNA synthesis. Briefly, 2 μg of RNA ideally in 8 μl of DEPC water was incubated with 1 μl of Amplification grade DNase enzyme (Sigma) and 1 μl of 10x DNase reaction buffer (Sigma) for 15 min at RT. 1 μl of Stop solution (Sigma) was added to inhibit the reaction and heated at 70°C for 5 min. Then 1X Reverse Transcriptase buffer (Invitrogen), 0.5 μMol/L each dNTP (Roche), 13.3U M-MLV-RT (Invitrogen) enzyme and 1 U/μl RNase inhibitor (Promega) and 0.15μM Primer p(dT)$_{15}$ for cDNA synthesis (Roche) were added and incubated at 42°C for 1 hr. Inactivation of enzymes was done by heating the reaction mix at 70°C for 10 min. cDNA was stored at -20°C.

2.4.3 Quantitative Real Time Polymerase Chain Reaction (qRT-PCR)

Primers were designed by using online Primer 3 software. Details of primers used in this study are given in tables 2.1 and 2.2. qRT-PCR reaction mixture was prepared by mixing 1 μl of 10 X PCR reaction buffer (Roche), 1 μl of DMSO (Sigma), 0.5 μl of 1:1000 dilutions of SYBR Green (sigma), 0.2 mmol of each dNTP (Roche), 0.15 U of Taq-Polymerase (produced In-house), 10pmol/μl of Forward and Reverse primers and 1μl of cDNA (1:10 diluted), volume was made up to 20μl with H_2O. PCR conditions to amplify cDNA were set as

- **Denaturation**, 95°C for 2 min one cycle,
- **PCR-40 cycles**
  - denaturation 95°C for 30 sec,
  - Annealing 56°C for 30 sec,
  - Extension 72°C for 30 sec.

- **Acquisition** temperature was different for each primer set (Table 2.1).

PCR reaction were run and analysed using LightCycler 480 (Roche). Data was analysed with LightCycler 480 software SW 1.5.1 (Roche) and values were normalised to house-keeping gene human/mice *GAPDH/Gapdh* and in case of isoform study *BRD4-Total/Brd4-total*. Comparative Ct method ($2^{-\Delta\Delta Ct}$) was used to measure relative fold change mRNA expression (Schmittgen and Livak, 2008).

Table 2.1 Human mRNA expression primer list

Gene name	Direction	Sequence	Product Size (bp)	Acquisition Temp (°C)
GAPDH	Forward	TGGGTGTGAACCATGAGAAGTA	120	81
	Reverse	GAGTCCTTCCACGATACCAAAG		
SELE	Forward	CTCTCCCTCCTGACATTAGCAC	123	81
	Reverse	AGGCTTTTGGTAGCTTCCATCT		
VCAM-I	Forward	GGAAAAACAGAAAAGAGGTGGA	125	79
	Reverse	GCCCATGACACTACATGTCAAC		
IL6	Forward	AGTGAGGAACAAGCCAGAGC	99	79
	Reverse	GTCAGGGGTGGTTATTGCAT		
BRD4-Common	Forward	TCCAACCCTAACAAGCCCAA	110	81
	Reverse	GAAAGGCCATGCAAACTGGT		
BRD4-Long	Forward	AGCGAAGACTCCGAAACAGA	97	81
	Reverse	TCTGCTGATGGTGGTGATGA		
BRD4-Short	Forward	TCCTCCAAGATGAAGGGCTT	156	81
	Reverse	AGCTTGCTGGGAAGGAATCT		
MIDKINE	Forward	ACCAGTGCCTTCTGTCTGCT	176	81
	Reverse	ATTGTGGGGAAGAACAAAAGC		
p38MAPK	Forward	CCAGCTTCAGCAGATTATGC	246	81
	Reverse	TGGTACTGAGCAAAGTAGGCA		
PTP1B	Forward	TGGGAAATGCAGGGAGTTCT	135	81
	Reverse	TGACTCATGCTTTCGATGCC		

Table 2.2 Mouse mRNA expression primer list

Gene name	Direction	Sequence	Product Size (bp)	Acquisition Temp (°C)
Gapdh	Forward	AGGTCGGTGTGAACGGATTTG	129	81
	Reverse	TGTAGACCATGTAGTTGAGGTCA		
Brd4-Common	Forward	AAGCCTGGAGATGACATCGT	148	81
	Reverse	TTGCTGCCCCTGTTTCTTTC		
Brd4-Long	Forward	AGCCAAGTCCTCAAGTGACA	107	81
	Reverse	TCTCCTTCTCTGCATGCTCA		
Brd4-Short	Forward	ACGTGATTGCTGGTTCTTCC	123	81
	Reverse	CCGTGTCCAATGATTAGGCA		

2.5 Cell Viability Assay

Cell viability assay for each experimental set was performed using trypan red cir dye exclusion assay. Briefly, cells were trypsinised and resuspended in 1 ml of HUVEC medium. 5 µl of resuspended cells were mixed with 20 µl of media and 25 µl of 0.5% trypan blue dye. Then, 10µl of mixture was loaded onto haemocytometer. Viable cells (colourless) and non-viable cells (blue coloured) were counted and percentage of viable cells was calculated.

2.6 Protein Isolation

HUVECs were grown and treated as described above. Cells were washed with DPBS and trypsinised. Cell pellets were resuspended by using lysis buffer (Cell Signalling) containing final concentration: 2 mM Tris/HCl, 15 mM NaCl, 0.1 mM Na$_2$EDTA, 0.1 mM Egtazic acid (EGTA), 0.1% Triton X-100, 0.25 mM sodium pyrophosphate, 0.1 mM β-glycerophosphate, 0.1 mM Sodium orthovanadate (Na$_3$VO$_4$), 0.1 µg/ml leupeptin and 1 mM Phenylmethylsulfonyl fluoride (PMSF), EDTA-free protease inhibitor cocktail (Sigma) and Phospho-stop phosphatase inhibitor (Sigma) were added freshly. Lysates were centrifuged at 13000rpm for 15min and clear supernatants (total proteins) were separated. Proteins quantification was done by Bradford method using protein reagent dye (Bio-Rad).

2.7 Western blot

Equal amounts of protein (35µg) were resolved on 4-12% Bis-Tris SDS-PAGE (sodium dodecyl sulfate-polyacrylamide gel electrophoresis) gels (Thermofisher Scientific) together with molecular weight standards, Proteins were transferred onto nitrocellulose membrane of 0.4 µM pore size (Millipore) by using Trans-blot SD cell system (Bio-Rad) for one hour. To avoid non-specific binding, membranes were blocked in blocking buffer: 5% milk in Tris-buffered saline, containing 50mM Tris-HCl, 200 mM NaCl and 0.1% Tween-20 (TBST). Blocked membranes were incubated overnight at 4°C with blocking buffer containing indicated primary antibodies against, anti-HSP70-antibody (Cells Signaling #4872) in 1:1000 dilution, anti-BRD4-antibody (Abcam # ab84776) in 1:1000 dilution, anti-β-actin-antibody (Sigma # A5316) in 1:10,000 dilution, anti-MIDKINE-antibody (Abcam #ab36038) in 1:500 dilution, anti-PTP1B-antibody (Cell Signaling #5311) in 1: 1000 dilution, anti-AKT-antibody (Cell Signaling #9272) in 1:1000 dilution and anti-p-AKT (Ser 473)-antibody (Cell Signaling #9271) in 1:500 dilution. Next day, membranes were washed in blocking buffer for 3 times 15 min each followed by incubation with horseradish peroxidase-conjugated (HRP-conjugated) secondary antibody (Bio-Rad) in 1:10,000 dilution for 1hr at room temperature. Membranes were washed in blocking buffer 3 times, 15 min each followed by washing with DPBS. Protein bands were detected by using chemiluminescence detection method using Chemi-Doc (Bio-Rad). Protein bands were quantified by Image lab software and normalized to either HSP70 or β-actin.

2.8 Trans-Endothelial/Epithelial Electrical Resistance (TEER)

In order to analyse the intactness of HUVECs monolayer, TEER was measured across the monolayer as described previously (Callahan *et al.,* 2004; Kazakoff *et al.,* 1995; Man *et al.,* 2008). Briefly, HUVECs were plated on 0.4µM transwell inserts (Corning CoStar cooperation), coated with collagen, and plated cells at a density 1 x 10^5 cells/well at passage 4. Achievement of monolayer was confirmed by measuring the TEER across the monolayer. Experiments were performed only when TEER reached the reference value of >70Ω.cm^2 as described previously (Callahan *et al.,* 2004; Kazakoff *et al.,* 1995; Man *et al.,* 2008; Srinivasan *et al.,* 2015). Established monolayers were treated with DMSO (control) for 12 hrs, TNF-α for 12 hrs, RVX208/JQ1 for 12 hrs, pre-treatment with RVX208/JQ1 for

12 hrs followed by TNF-α for 12 hrs. TEER was measured after 1-, 3-, 6-, 12- and 24-hrs of treatments using the epithelial volt/Ohm meter (EVOM2). Values were normalized against the resistance of blank well coated with collagen and containing only medium.

2.9 Statistical Analysis

Statistical analysis of real time, western blot and TEER data was performed using GraphPad Prism 5 software. Three or more independent biological replicates of all experiments were analysed by analysis of variance (ANOVA) and were compared to control groups by using Bonferroni post-test. Statistical significance was analysed by using Student´s t-test. All results were plotted in graphs as mean and error bars represent ± standard error mean (SEM). Probability of less than 0.05 was considered significant (* $p<0.05$, ** $p<0.01$, *** $p<0.001$).

2.10 Experimental animals

2.10.1 Aging Mice

Wild-type C57BL/6 mice (courtesy of Dr. Muzna Zahur, Viral Vector Lab, Department of Neurobiology, UMG) which were bred under sterile conditions and animals were sacrificed at the age of 1-, 3-, 6-, 8-, 12-, 15- and 18-months. Hearts were immediately frozen in liquid nitrogen.

2.10.2 Hypertrophic Mice

The generation and maintenance of inducible Endothelial cell-specific *Ptp1b* knock-out (Endo.*Ptp1b*.KO) and the corresponding control (Endo.*Ptp1b*.WT) mice were reported previously (Gogiraju *et al.,* 2016). Likewise, the transverse aortic constriction (TAC) or SHAM surgery on 10-12 week old female mice (Endo.*Ptp1b*.KO and Endo.*Ptp1b*.WT) was reported previously (Gogiraju *et al.,* 2016). Briefly, mice with *loxP* flanked *Ptp1b* allele (*Ptp1b^{fl/fl}*) were bred either with Wild type mice or with transgenic mice expressing a fusion protein of *Cre* recombinase-estrogen receptor under the control of endothelial receptor tyrosine kinase promoter (*Tie2.ERT2.Cre*). The off-spring with desired genotype were then fed with Tamoxifen diet to induce Cre recombinase activity. Afterwards, 10-12 weeks-old females with either KO or WT genotype were subjected to TAC or SHAM surgery. In TAC group, a band is placed around the aorta of mice to induce pressure on heart, while SHAM

(an experimental control) group also underwent surgery, however, aortic arch was exposed but no band was placed around the aorta. This strategy gave rise to four groups of animals namely: 1. Wild-type SHAM (WT-SHAM), 2. Wild-type TAC (WT-TAC), 3. Endothelial-specific *Ptp1b* knockout SHAM (KO-SHAM), and 4. Endothelial-specific *Ptp1b* knockout TAC (KO-TAC). After 20 weeks of TAC/SHAM surgery, five independent animals were taken from each group as biological replicates and whole heart tissue lysates were prepared in the presence of protease and phosphatase inhibitors. Afterwards, 50 µg of proteins were tryptic digested and the resulting peptides were subjected to liquid chromatography-tandem mass spectrometry (LC-MS/MS) analysis.

2.11 Global Proteome analysis

2.11.1 In-solution digestion

We performed the in-solution digestion of total proteins essentially as described previously (Leon *et al.,* 2013), with minor modifications. Equal amounts of proteins (50 µg) from each animal were precipitated with 5 volumes of ice cold 100% acetone. Pellets were washed with 1 ml of ice cold 80% ethanol (Waters), dried and resuspended in 0.1% Rapigest (Waters) solution (Rapigest prepared in 25 mM ammonium bicarbonate solution). Proteins were then reduced using dithiothreitol (DTT) and alkylated with iodoacetamide (IAA). Trypsin concentration of 0.1 µg/µl (Promega) was used at 1:40 ratio to Protein: Trypsin (For 1mg protein 25 µg trypsin) to digest the protein. Proteins were digested overnight at 37° C with constant shaking. After overnight incubation, formic acid was added to reduce the pH and to stop the trypsin reaction as well as to degrade Rapigest. Samples were centrifuged at 13000 rpm for 5 min to pellet down undigested proteins and degraded Rapigest. Supernatants were dried in the speed vacuum concentrator and processed for mass spectrometry analysis.

2.11.2 LC-MS/MS Analysis

For mass spectrometric analysis, samples were reconstituted in 2% acetonitrile/0.1% formic acid (*v:v*) and were analysed as described previously (Khan *et al.,* 2016). Briefly, reconstituted samples were analysed at Q-Exactive hybrid quadrupole mass spectrometer (ThermoFisher Scientific) by using Excallibur 2.4 software. 70,000 full width at half maximum (FWHM) resolution settings were used to acquire MS scan across 350-1600m/z. Peptides were selected on basis of following criteria: charge state 2, or higher, up to 12

most abundant peptide, intensity threshold of $>2*10^{-4}$. Followed by isolation at 2.0 FWHM width, fragmentation was done with nitrogen at 25% collision energy. In order to record the resulted product ion spectra resolution setting was 17,5000 FWHM. Three technical replicates per sample were acquired.

2.11.3 Bioinformatic analysis of mass spectrometry data

Peak lists were extracted with Raw2MSMS software in data independent acquisition (DIA) model and the obtained mass spec data was processed using Sequential Window Acquisition of all THeoretical fragment ion spectra (SWATH) analysis. Difference of expression between the groups was observed by Principle Component Analysis (PCA) using MarkerView Software 1.2.1.1 (AB SCIEX). In order to perform cluster analysis, we used Search Tool for the Retrieval of Interacting Genes/Proteins (STRING) database to analyse functional annotation of differentially expressed proteins.

2.11.4 Welch's t-test based analysis

After validation of different clusters in PCA, data was further analysed by Welch's t-test to generate lists of differentially expressed proteins (significance level $p< 0.05$) between all groups. Comparison was done first between WT-SHAM and KO-SHAM groups and then between WT-TAC and KO-TAC groups. Detailed analysis of proteomic data set with Welch's t-test generated lists of upregulated and downregulated proteins in all groups. Volcano plots were generated by using -Log10 of p values (Welch's t test), which were associated with individual proteins, against Log_2 of fold change in abundance between the WT-SHAM and KO-SHAM, WT-SHAM and WT-TAC, KO-SHAM and KO-TAC, WT-TAC and KO-TAC.

2.11.5 Ingenuity Pathway analysis (IPA)

In order to analyse the proteome data with reference to functions of proteins, pathways involved, upstream regulators, downstream effectors, we decided to use Ingenuity Pathway analysis (IPA- Qiagen) in collaboration with Prof. Tuula Anneli Nyman, University of Oslo. The data was uploaded to IPA after calculating p-values and fold change using Perseus software. Direct and indirect relationship between the differentially regulated proteins were analysed and supported by previously reported experimentally observed data from human and mice studies. We considered proteins with a p values <0.05 and a fold change cut-off value of 1.5 as significant and generated the lists of top canonical

pathways, differentially abundant proteins and potential upstream regulators based on statistical measurement of differential expression based on the statistical effect size, log2 ratio, and the P value (Z-Score).

2.12 Mitochondrial Functional Assay

In order to analyse the effect of PTP1B inhibition on HUVECs mitochondrial function, we used mitochondrial ToxGlo^{TM} assay kit (Promega). Briefly, 1×10^4 cells/well were plated in 96 well culture plates. Cells were allowed to adhere and grow over night. Next day, cells were treated as follows: 1. non-treated control, 2. Claramine 100µM (PTP1B inhibitor) 30 min, 3. TNF-α only (1500/ml for 6hrs), 4. Pre-treatment with Claramine for 30 min followed by TNF-α treatment for 6hrs, 5. Sodium Azide 100µM for 3 hrs.

After completion of treatments, cell membrane integrity was analysed via detection of dead cell protease activity. 5X cytotoxicity detection reagent was prepared by mixing 10 µl of fluorogenic peptide substrate (Promega) with 2 ml of assay buffer (Promega). 20 µl of cytotoxic detection reagent was added and incubated at 37°C for 30 min. Cytotoxic detection reagent analyse membrane integrity and give fluorescence while interacting with necrosis associated protease. Fluorescence was measured with Victor multilabel counter (Wallac) at 485nm$_{Ex}$/520–530nm$_{Em}$. Average of measured values of non-treated controls were subtracted from average of all treatments and percentage response of each test was calculated.

Next, 2X ATP detection reagent was prepared by mixing 10 ml of ATP detection buffer containing ATPase inhibitors and Luciferase (Promega) with lyophilised ATP detection substrate, luciferin (Promega). 100 µl of ATP detection reagent was added to lyse the cells. ATP generates the luminescent signal which was measured with Victor multilabel counter (Wallac). Average of measured values of non- treated controls were subtracted from average of treatments and percentage response of each test was measured. To minimise the ATP production from glycolysis, all treatments were done in DMEM containing Galactose and in the absence of serum to avoid Glucose.

3. Results.

3.1 Establishment of *in-vitro* inflammatory model using HUVECs

In order to establish the *in-vitro* inflammatory model, HUVECs were treated with or without (control) 20ng/ml TNF-α for 2 hrs. Afterwards, cells were fixed in 4% PFA, stained with anti-NF-κB antibody and analysed for cellular localisation of NF-κB. As expected, NF-κB was localised in cytoplasm of control cells, however, it translocated inside the nucleus in TNF-α treated cells (Fig. 3.1A). It is known, that upon activation by inflammatory stimuli, NF-κB binds to Super Enhancers (SEs) of pro-inflammatory genes regulatory regions and turn-on the transcription of pro-inflammatory genes like *VCAM-I, SELE, IL6* and *IL8*. Hence, we performed mRNA expression analysis for *VCAM-I* and *SELE*, two well-known markers of inflammation, and found significantly induced expression of them in TNF-α treated cells as compared to control cells (Fig. 3.1B). These results confirm the successful establishment of *in-vitro* inflammatory phenotype in HUVECs.
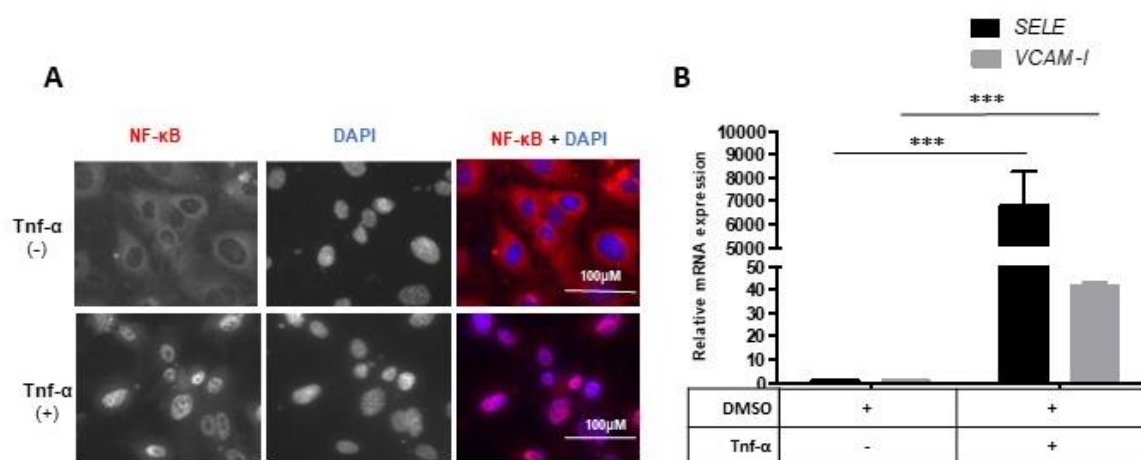
Figure 3.1. Establishment of inflammatory phenotype in HUVECs. A, Immunofluorescence images showing control (-) and TNF-α treated (+) HUVECs which were stained with anti-NF-κB antibody (red) and nuclei were counter-stained with DAPI (blue). **B**, bar graph showing relative mRNA levels of *VCAM-I* and *SELE* after normalization to house-keeping gene *GAPDH*, in control and TNF-α treated cells. Values are mean ± SEM of three biological replicates and asterisks indicate statistical significance of *** $p < 0.001$.

After establishment of *in-vitro* inflammatory model, we decided to analyse the effect of BRD4 inhibition on HUVECs with and without inflammatory stimuli. We wanted to analyse, whether this inhibition is rescuing the HUVECs from inflammatory stress.

3.2 Role of BRD4 during inflammation

It is recently reported that BRD4 interacts with NF-κB and the resulted complex binds to SEs of pro-inflammatory gene regulatory regions during inflammatory response (Brown *et al.,* 2014; Xu and Vakoc, 2014a). Therefore, it is interesting to analyse whether BRD4 inhibition has any significant effect on inflammatory response. Towards this end, we comparatively studied two small molecule inhibitors of BRD4, namely JQ1 and RVX208.

3.2.1 BRD4 inhibition using JQ1 inhibitor

The small molecule thienotriazolodiazepine, widely known as JQ1, binds to bromodomains of BET family proteins BRD2, BRD3, BRD4 and BRDT, and inhibits their activity (Bid and Kerk, 2016). Among the BET family members, BRD4 is highly expressed in HUVECs; hence the results obtained with JQ1 might be directly attributable to BRD4 inhibition in these cells (Huang *et al.,* 2016). To establish the concentration of JQ1 required to efficiently inhibit the BRD4 function, we treated HUVECs with different concentrations of JQ1 (50 nM to 1 μM) for 4 hrs followed by 2 hrs of TNF-α treatment. Thereafter, cells were harvested and analysed for the expression levels of pro-inflammatory marker *VCAM-I*. Our analysis indicated that treatment with 500 nM of JQ1 was more effective in suppressing pro-inflammatory marker expression in our system (Fig. 3.2A). As these preliminary results are in agreement with the literature (Brown *et al.,* 2014), we decided to use 500 nM of JQ1 in all our further experiments, unless otherwise stated.

Next, we designed an experimental set-up in which HUVECs were treated in four groups:- **1: Control -** cells were treated with DMSO for 4 hrs, **2: TNF-α-only -** cells were treated with DMSO for 4 hrs followed by TNF-α for 2 hrs, **3: JQ1-only -** cells were treated with JQ1 for 4 hrs, and **4: JQ1+TNF-α -** cells were treated with JQ1 for 4hrs followed by TNF-α for 2 hrs. In order to check any possible cytotoxic effect of TNF-α and JQ1 treatments on HUVECs, we checked the viability of cells after treatments by using Trypan blue dye exclusion assay. These results showed that none of the treatments had any significant cytotoxic effect as compared to control cells (Fig. 3.2B). RNA expression analysis revealed that the control as well as JQ1-only treated cells have basal levels of pro-inflammatory

markers, whereas TNF-α treated cells showed significantly higher expression of inflammatory markers (Fig. 3.2C).
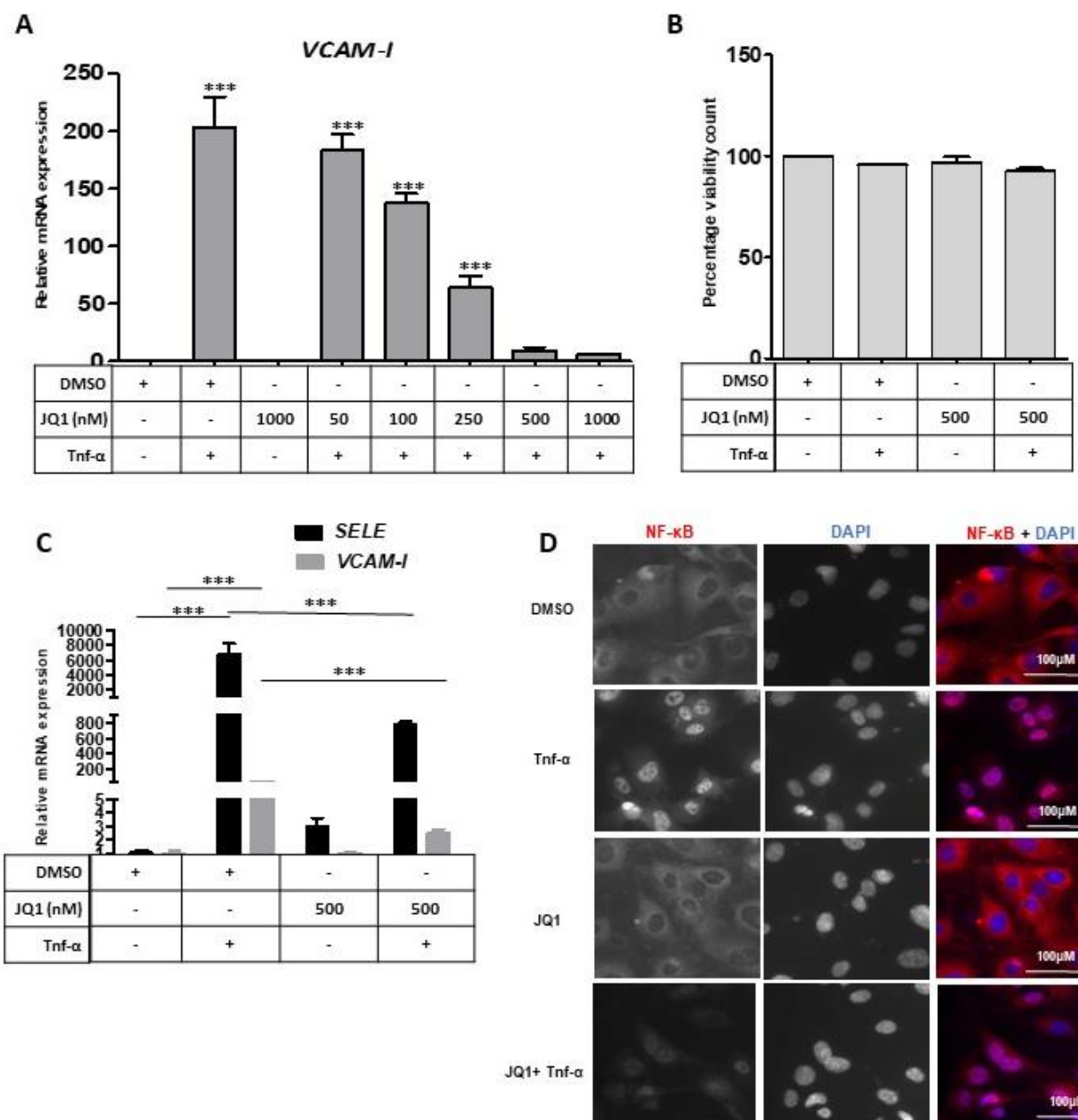
Figure 3.2. BRD4 inhibition using small molecule inhibitor JQ1. A, bar graph showing relative mRNA expression of *VCAM-I* after normalization to house-keeping gene *GAPDH*, in HUVECs treated with DMSO (control)-, TNF-α-only, JQ1-only- (1 μM), and various concentrations of JQ1 (50-, 100-, 250-, 500 nM, and 1μM) followed by TNF-α treatment. **B,** bar graph showing viability of cells (% viability unit) after treated with TNF-α-only, JQ1-only and JQ1+TNF-α. **C,** bar graph showing relative mRNA levels of *VCAM-I* and *SELE* after normalization to house-keeping gene *GAPDH*, in DMSO (control), TNF-α treatment, JQ1-only treatment and JQ1 followed by TNF-α treatment. Values in A and C are mean ± SEM of three biological replicates and asterisks indicate statistical significance of *** p< 0.001, and ** p<0.01. **D,** Immunofluorescence images of HUVECs treated with DMSO (control)- , TNF-α-only- , JQ1-only and JQ1+TNF-α were stained with anti-NF-κB antibody (red) and nuclei were stained with DAPI (blue).

Interestingly, pre-treatment with JQ1 significantly blocked the expression of pro-inflammatory markers *VCAM-I* and *SELE* by 20-fold and 9.5-fold, respectively, as compared to TNF-α-only treated cells (Fig. 3.2C). These results indicate successful inhibition of BRD4 function, which results in blocking of its binding to SEs of pro-inflammatory genes and subsequent inhibition of their expression.

As a next step, we analysed NF-κB localisation in above mentioned treatments. As expected, NF-κB is present in the cytoplasm of control and JQ1-only treated cells, whereas it translocated into the nucleus in TNF-α treated cells. Notably, we found that JQ1 pre-treatment did not affect the nuclear translocation of NF-κB (Fig. 3.2D).

Collectively, these results indicate that JQ1 inhibits the function of BRD4 in HUVECs and thereby alleviates the inflammatory phenotype. Although JQ1 has been used in almost all BRD4 inhibition studies, its non-specificity to BRD family proteins and short half-life makes it unsuitable for clinical use (Wadhwa and Nicolaides, 2016). Recent studies identified RVX208 as another BRD4 inhibitor, which covalently binds to BD2-domain of BRD4 (Picaud *et al.,* 2013; Wadhwa and Nicolaides, 2016). Interestingly, RVX208, whose molecular target was not known until recently, was already used in clinical trials for treatment of different diseases like atherosclerosis, diabetes, Alzheimer's disease, and chronic kidney disease (Nikolic *et al.,* 2015; Picaud *et al.,* 2013). Hence, we comparatively studied the efficiency and effectivity of BRD4 inhibition using JQ1 and RVX208 in our inflammatory model.

3.2.2 BRD4 inhibition using RVX208 inhibitor

To establish the concentration of RVX208 required to efficiently inhibit the BRD4 function, we treated HUVECs with different concentrations of RVX208 (50-, 100-, 150-, and 200 µM) for 4 hrs followed by 2 hrs of TNF-α treatment as we established for JQ1 experiments. Thereafter, cells were harvested and analysed for the expression level of pro-inflammatory marker *SELE.* This analysis showed no expression reduction of *SELE* in TNF-α treated cells (Fig. 3.3A), indicating that RVX208 probably could not inhibit BRD4 function, even at higher concentration, and after 4 hrs of treatment. Hence, we decided to use time dependent strategy to identify the time and concentration of RVX208 required to inhibit BRD4 function. For this reason, we treated the cells with 30 µM and 60 µM of RVX208 for 12-, 24-, and 48-hrs followed by treatment with TNF-α. In order to check any possible cytotoxic effect of TNF-α and RVX208 treatment on HUVECs, we checked the viability of

cells after treatments by using Trypan blue dye exclusion assay. Our results showed that cell viability after 12 hrs of DMSO and RVX208 treatment was better than 24 hrs and 48 hrs (Fig. 3.3B).
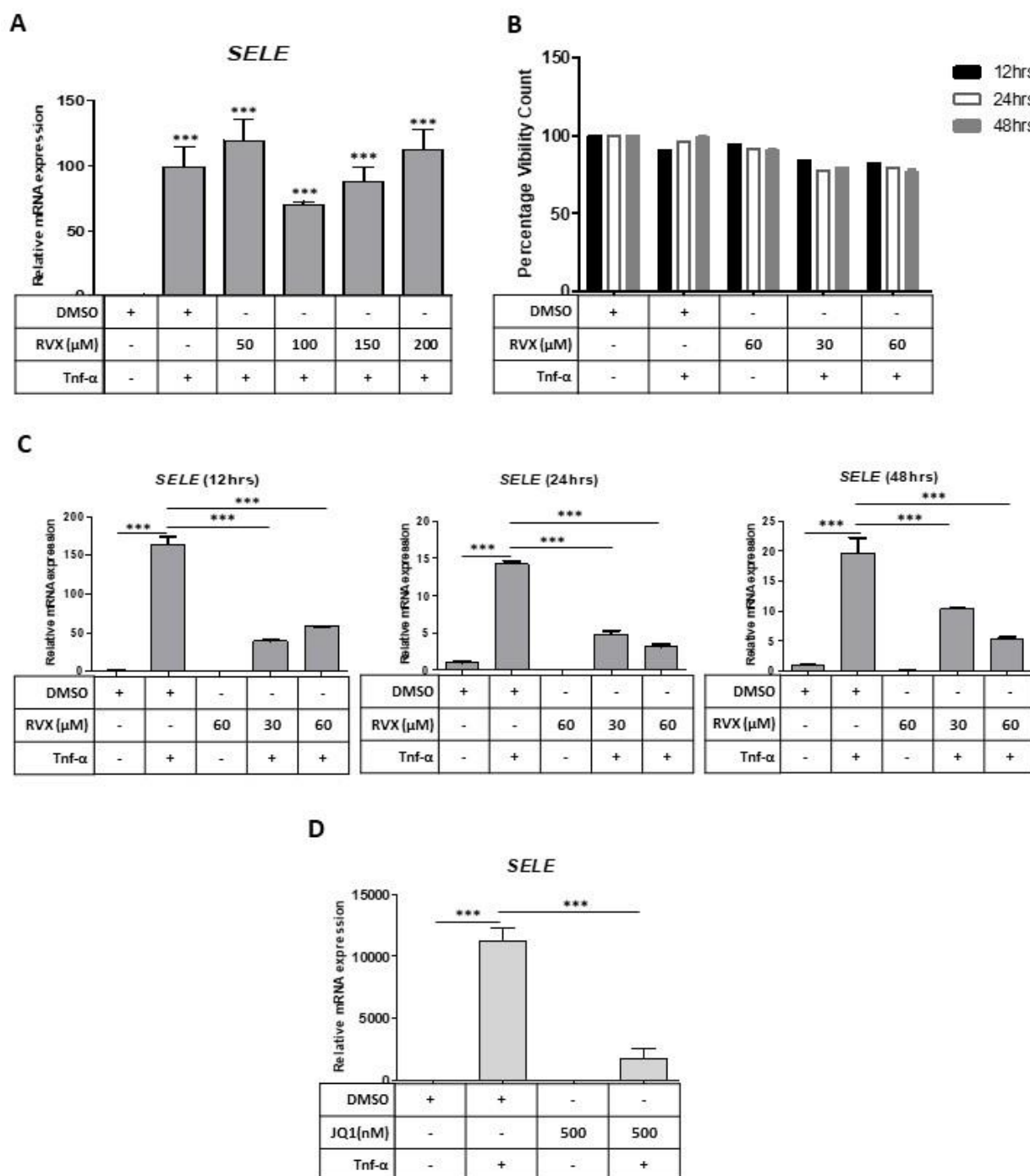
Figure 3.3. Optimization of RVX208 treatment for inhibition of BRD4 function. A, bar graph showing relative mRNA levels of *SELE* after normalisation to house-keeping gene *GAPDH* in DMSO (control), TNF-α treatment, RVX208 (50-, 100-, 150-, and 200 μM) followed by TNF-α treatment. **B,** bar graph shows percentage cell viability count in three different sets **1: 12 hrs set**. DMSO (control) 12 hrs, TNF-α-only 12 hrs, RVX208-only 12 hrs, RVX208 (30 and 60 μM) 12 hrs followed by TNF-α 12 hrs. **2: 24 hrs set.** DMSO (control) 24 hrs, TNF-α-only 12 hrs, RVX208-only 24 hrs, RVX208 (30 and 60 μM) 24 hrs followed by TNF-α 12 hrs. **3. 48 hrs set.** DMSO (control) 48 hrs, TNF-α-only 12 hrs, RVX208-only 48

hrs, RVX208 (30 and 60 µM) 48 hrs followed by TNF-α 12 hrs. **C,** bar graph showing relative mRNA levels of *SELE* after normalisation to house-keeping gene *GAPDH*, in DMSO control, TNF-α-only, RVX208-only 30 µM and 60 µM (12 hrs to 48 hrs), and RVX208 (30 µM and 60 µM) followed by TNF-α treatment. **D.** bar graph showing relative mRNA levels of *SELE* after normalisation to house-keeping gene *GAPDH*, in DMSO control, TNF-α-only, JQ1-only for 12 hrs, JQ1 12 hrs followed by TNF-α treatment for 12 hrs. **A,C, D,** values are mean ± SEM of three biological replicates and asterisks indicate statistical significance of *** p< 0.001.

RNA expression analysis indicated that the 12 hrs pre-treatment with RVX208 significantly reduces the expression of pro-inflammatory marker *SELE* by 4-fold, as compared to TNF-α treatment (Fig. 3.3C). Based on these results, we decided to use 60 µM of RVX208 for 12 hrs in all our further experiments, unless otherwise stated. As we wanted to perform the comparative studies on RVX208 and JQ1, we first established whether JQ1 could also be used at 500 nM for 12 hrs. We treated the cells with 500 nM of JQ1 for 12 hrs, TNF-α for 12 hrs, and JQ1 for 12 hrs followed by TNF-α 12 hrs. Then we performed the RNA expression analysis and found that pre-treatment with JQ1 for 12 hrs could reduce the expression of pro-inflammatory marker *SELE* by 5-fold (Fig. 3.3D).

After establishing both time and concentrations of RVX208 and JQ1 required to efficiently inhibit the inflammatory response, we designed the following experimental setup in which both RVX208 and JQ1 were compared simultaneously. **1: Control -**cells were treated with DMSO for 12 hrs. **2: TNF-α-only -** cells were treated with TNF-α for 12 hrs. **3: RVX/JQ1-only -** cells were treated with either RVX or JQ1 for 12 hrs. **4: RVX/JQ1+TNF-α -** cells were pre-treated with either RVX or JQ1 for 12 hrs then with TNF-α for 12 hrs. Here we would like to emphasize that, we used the above experimental setup to study the function of BRD4 in almost all treatments to HUVECs, unless otherwise stated. We firstly checked the cell viability of both sets of treatments to confirm that treatments do not have significant cytotoxic effect. This analysis indicates that treatments alone or in combinations were not significantly toxic for cells (Fig. 3.4 A and B).
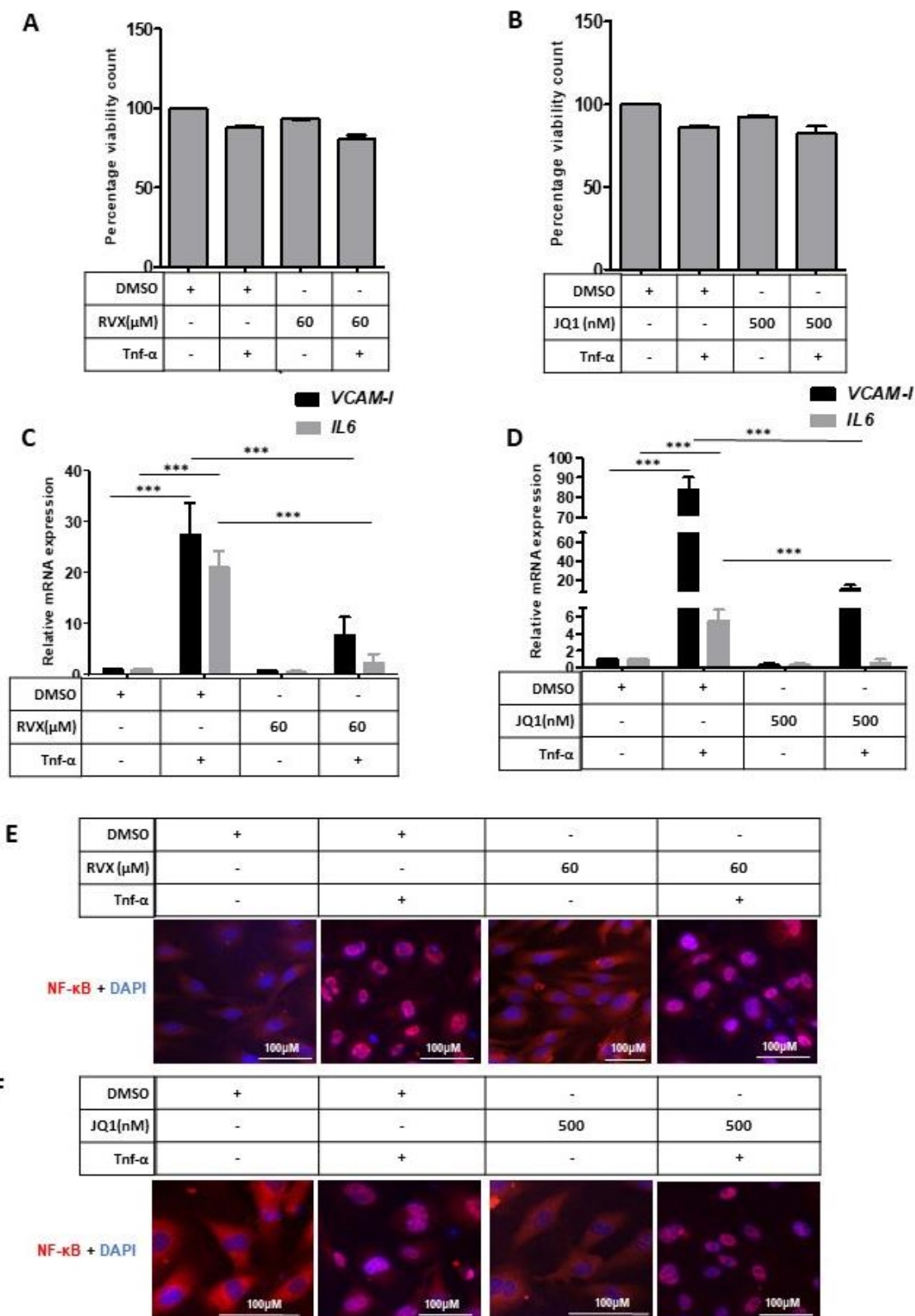
Figure 3.4 BRD4 inhibition using RVX208 and JQ1. A, bar graph shows percentage cell viability count in treatments with RVX208 after 12 hrs treatments. **B,** bar graph shows percentage cell viability count in treatments with JQ1 after 12 hrs treatments. **C,** bar graph showing relative mRNA levels of inflammatory markers *VCAM-I* and *IL6* after normalisation to house-keeping gene *GAPDH*, in HUVECs treated with DMSO, TNF-α-only, RVX208-only and RVX208+TNF-α **D,** bar graph showing relative mRNA levels of inflammatory markers *VCAM-I* and *IL6* after normalisation to house-keeping gene *GAPDH*, in HUVECs treated with DMSO, TNF-α-only, JQ1-only and JQ1+TNF-α. **C-D,** values are mean ± SEM of three

biological replicates and asterisks indicate statistical significance of *** p< 0.001. **E and F,** immunofluorescence images for the effect of RVX (E) and JQ1 (F) on the cellular localization of NF-κB in response to indicated treatments. HUVECs were stained with anti-NF-κB antibody (red) and DAPI (blue).

Then we performed the RNA expression analysis and found that pre-treatment with RVX208 could reduce the expression of inflammatory markers by 3-fold and 7-fold for *VCAM-1* and *IL6*, respectively, as compared to TNF-α treatment (Fig. 3.4 C). Similarly, pre-treatment with JQ1 could reduce the inflammatory markers by 8-fold and 10-fold for *VCAM-I* and *IL6*, respectively, as compared to TNF-α treatment (Fig. 3.4 D). This analysis indicates that both JQ1 and RVX208 could efficiently inhibit the inflammatory response. Moreover, we also noted that the basal expression levels of inflammatory markers *VCAM-1* and *IL6* were reduced by 3-fold and 5-fold, respectively, in JQ1-only treatment as compared to DMSO (Fig. 3.4 C and D). Similarly, RVX208-only treatment is also reducing the basal expression level of inflammatory markers *VCAM-1* and *IL6* by 1.4-fold and 2-fold, respectively, as compared to DMSO.

To confirm that longer incubation (12 hrs) with RVX208 or JQ1 does not have any effect on translocation of NF-κB into the nucleus, we performed the immunostaining for NF-κB localization after above mentioned treatments. This analysis showed that NF-κB is present in the cytoplasm of control and RVX208/JQ1-only treated cells, whereas it translocated into the nucleus in TNF-α treated as well as in RVX208/JQ1+TNF-α treated cells (Fig. 3.4 E and F). Hence, these results proved that RVX208/JQ1 pre-treatment followed by TNF-α does not affect the nuclear translocation of NF-κB.

Collectively, our results show that BRD4 inhibition with either RVX208 or JQ1 suppresses the inflammatory response in HUVECs. In this context, it is interesting to note that BRD4 has two different isoforms namely, BRD4-long (BRD4-L) and BRD4-short (BRD4-S), which have differential roles in different diseases. In particular, the differential expression of BRD4 isoforms is associated with metastasis in colon and breast cancers, in which BRD4-S isoform enhances the breast cancer metastasis whereas BRD4-L isoform inhibits metastasis (Alsarraj *et al.,* 2013; Hu *et al.,* 2015). We were interested to determine the expression of BRD4 isoforms in normal as well as in inflammatory states of ECs. Hence, we wanted to study the expression pattern of BRD4 isoforms not only in HUVECs in normal and inflammatory conditions but also during BRD4 inhibition studies and in CVDs models like cardiac hypertrophy and aging hearts.

3.3 Elucidating the role of BRD4 isoforms in endothelial dysfunction and in disease models

3.3.1 BRD4 isoform analysis in HUVECs

In order to determine the expression pattern of BRD4 isoforms in tissues of different diseases, we first decided to check the total mRNA levels of BRD4 (BRD4-Total) in our established system. HUVECs were treated as in above described experiments. We found that there is higher expression of *BRD4-Total* by 1.3-fold to 1.4-fold after 12 hrs of TNF-α treatment as compared control (DMSO). Treatments with either of RVX208 or JQ1 only, reveals a reduced expression of *BRD4-Total* by 1.6-fold and 1.8-fold in RVX208 and JQ1, respectively (Fig. 3.5A and B). These results led us to analyse the isoform specific expression of BRD4 during Inflammatory response or during treatment with RVX28 or JQ1. In order to analyse relative mRNA expression of *BRD4-L* and *BRD4-S* isoforms, Isoform specific primers were designed. *BRD4-L* and *BRD4-S* expression was first normalised to housekeeping gene *GAPDH* and then to *BRD4-Total* expression. Our data shows that there is no significant difference in expression levels of *BRD4-L* and *BRD4-S* isoforms during inflammatory response (TNF-α treatment) (Fig. 3.5 C and D). However, we observed that treatment with RVX208-only or JQ1-only results in reduced expression of *BRD4-L* by 1.75-fold and 2.5-fold, respectively (Fig. 3.5 C-D). These results suggest, that the observed reduction in expression levels of *BRD4-Total* could be due to the reduced expression of *BRD4-L*.

Figure 3.5. Expression analysis of *BRD4* isoforms in HUVECs. A and B, Bar graph showing relative mRNA levels of *BRD4-Total* normalised to house-keeping gene, *GAPDH* in cells treated with DMSO-only (control), TNF-α-only, RVX208-only, RVX208+TNF-α **(A)** or in cells treated with DMSO-only (control), TNF-α-only, JQ1-only , JQ1+TNF-α **(B). C and D,** Bar graph showing relative mRNA levels of *BRD4-L* and *BRD4-S* isoforms normalised first to house-keeping gene *GAPDH* and then normalised to *BRD4*-total in in cells treated with DMSO-only (control), TNF-α-only, RVX208-only, RVX208+TNF-α **(C) or** in cells treated with DMSO-only (control), TNF-α-only, JQ1-only , JQ1+TNF-α **(D).** Values are mean ± SEM of two biological replicates and asterisks indicate statistical significance of *** p< 0.001, ** p<0.01, and * p<0.05.

We have then analysed the expression of BRD4 isoforms at protein level. We treated the cells as mentioned above and performed the Western blot analysis using anti-BRD4 antibody. We found that the cells treated with TNF-α-only have higher expression of BRD4-S as compared to control. Similarly, we also found that HUVECs pre-treated with RVX208

or JQ1 followed by TNF-α treatment show higher expression of BRD4-S isoforms by 1.6-fold and 1.4-fold, respectively (Fig. 3.6A-B).
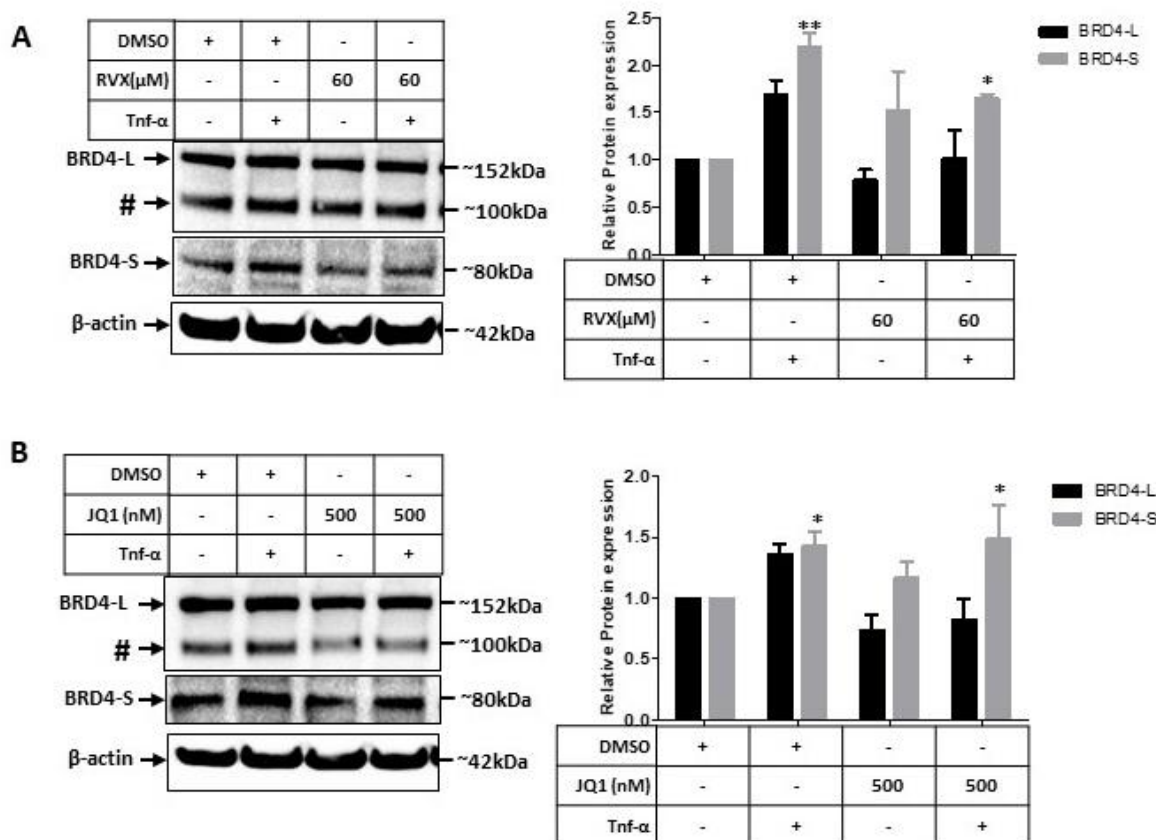
Figure 3.6. Expression analysis of BRD4 protein in HUVECs A-B. Western blot image (left Panels) and the corresponding relative quantification bar graph (right panels) showing the protein expression of BRD4-L and BRD4-S. Immunoblot was stripped and reprobed β-actin antibody. The β-actin (~42kDa) was used as a loading control. The band intensities of BRD4-L and BRD4-S were normalized to β-actin. The number symbol (#) indicates a band of ~100kDa with an un-known identity detected using BRD4 antibody. Values are mean ± SEM of two biological replicates and asterisks indicate statistical significance of *** p< 0.001, ** p<0.01 and * p<0.05.

Collectively, our results indicate that mRNA levels, but not protein levels, of *BRD4-L* are reduced when treated with either RVX208- or JQ1-only. In contrast to the RNA data, protein levels of BRD4-S isoform were slightly increased during inflammatory response and it was still high when there is pre-treatment with BRD4 inhibitors, RVX208 or JQ1. Hence, it would be interesting to analyse whether BRD4 isoforms show any specific expression pattern in long-term disease conditions/models as opposed to short-term *in vitro* studies. Towards this end, we wanted to study the BRD4 isoform expression in CVDs like aging mice hearts and in hypertrophic mice hearts.

3.3.2 BRD4 isoforms expression analysis in CVDs models

It is known that aging increases the risk of CVDs and about 90% of heart failures are associated with patient older than 70 years (Strait and Lakatta, 2012). Patients older than 65 years have high risk of inflammatory diseases. Expression analyses of inflammatory markers like *IL6* and *TNF-α* are elevated with aging (Kritchevsky *et al.,* 2005). Results showing a high expression levels of BRD4-S isoform during inflammation in HUVECs, led us to analyse expression pattern of BRD4 isoforms in hearts old aging mice. We collected hearts from wild-type C57BL/6 mice at age of 1-, 3-, 6-, 8-, 12-, 15-, and 18-months. Hearts were pulverized in liquid nitrogen and used for RNA isolation. We analysed mRNA expression levels of *Brd4-Total* (Fig. 3.7A) and Brd4 isoforms (Fig. 3.7B). We found that there is no significant difference of expression of *BRD4-Total* in hearts of 1- to 18-months-old mice (Fig. 3.7A). Analysis of isoform-specific expression revealed no significant difference in mRNA expression of both isoforms, except for 6-month-old mice heart, which showed significantly higher *Brd4-S* expression (Fig. 3.7B). At the protein level, BRD4-L expression was similar in all samples, but significantly higher in hearts of 18-month-old mice (Fig. 3.7C). However, BRD4-S expression is only detectable till 8-months old mice heart (Fig. 3.7C).

It is known that there is an increase in expression of inflammatory genes in pressure overloaded hearts (Chen *et al.,* 2015; Souders *et al.,* 2012). In this context, it would be interesting to analyse whether BRD4 has any expression changes in pressure overloaded TAC and its experimental control, SHAM, mice hearts. To this end, total proteins were isolated from TAC and SHAM mice hearts 20 weeks after surgery and subsequently subjected to western blotting analysis. We found that there was no significant expression difference in BRD4-L and BRD4-S isoforms in TAC and SHAM mice hearts (Fig. 3.7D).
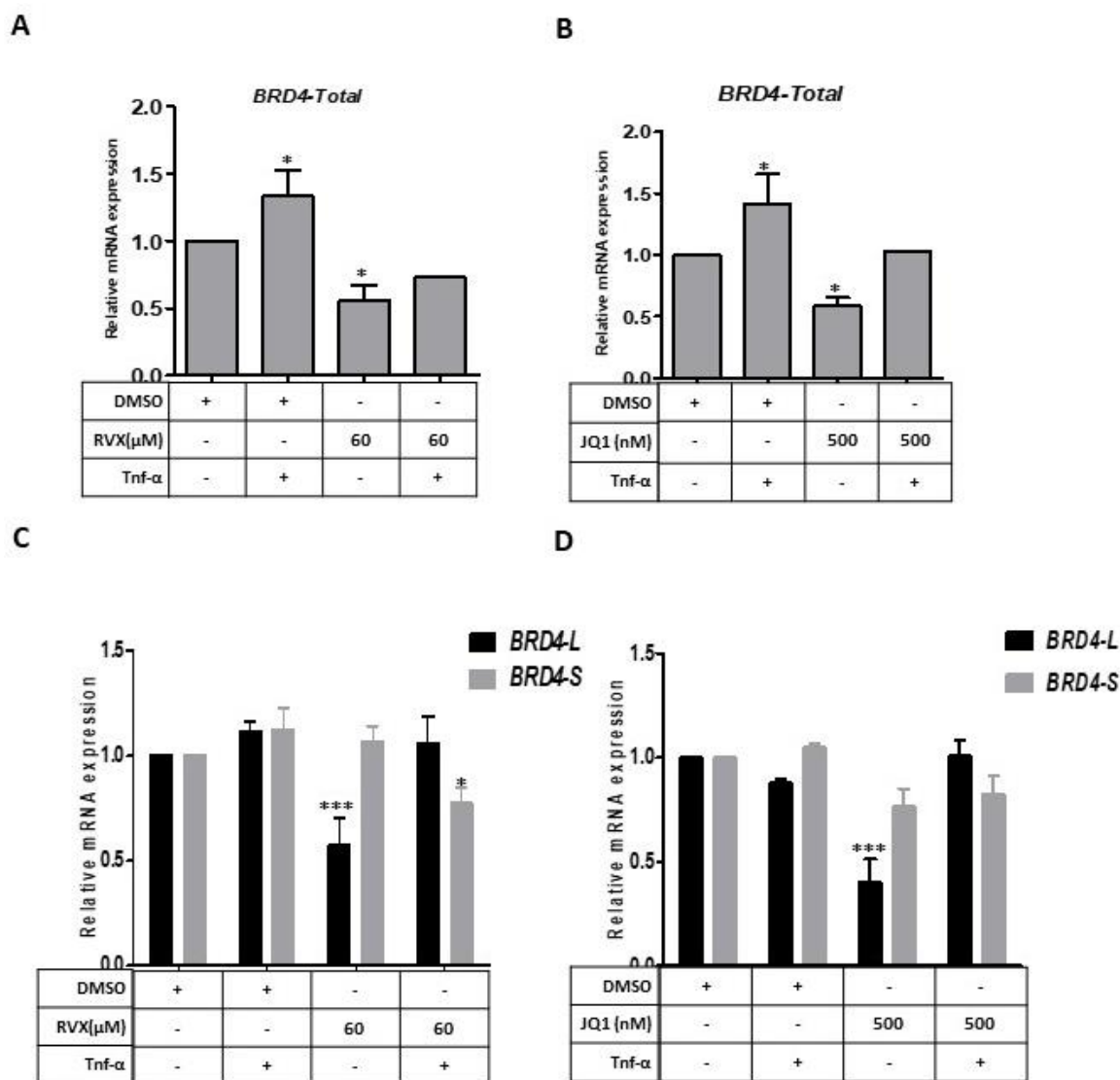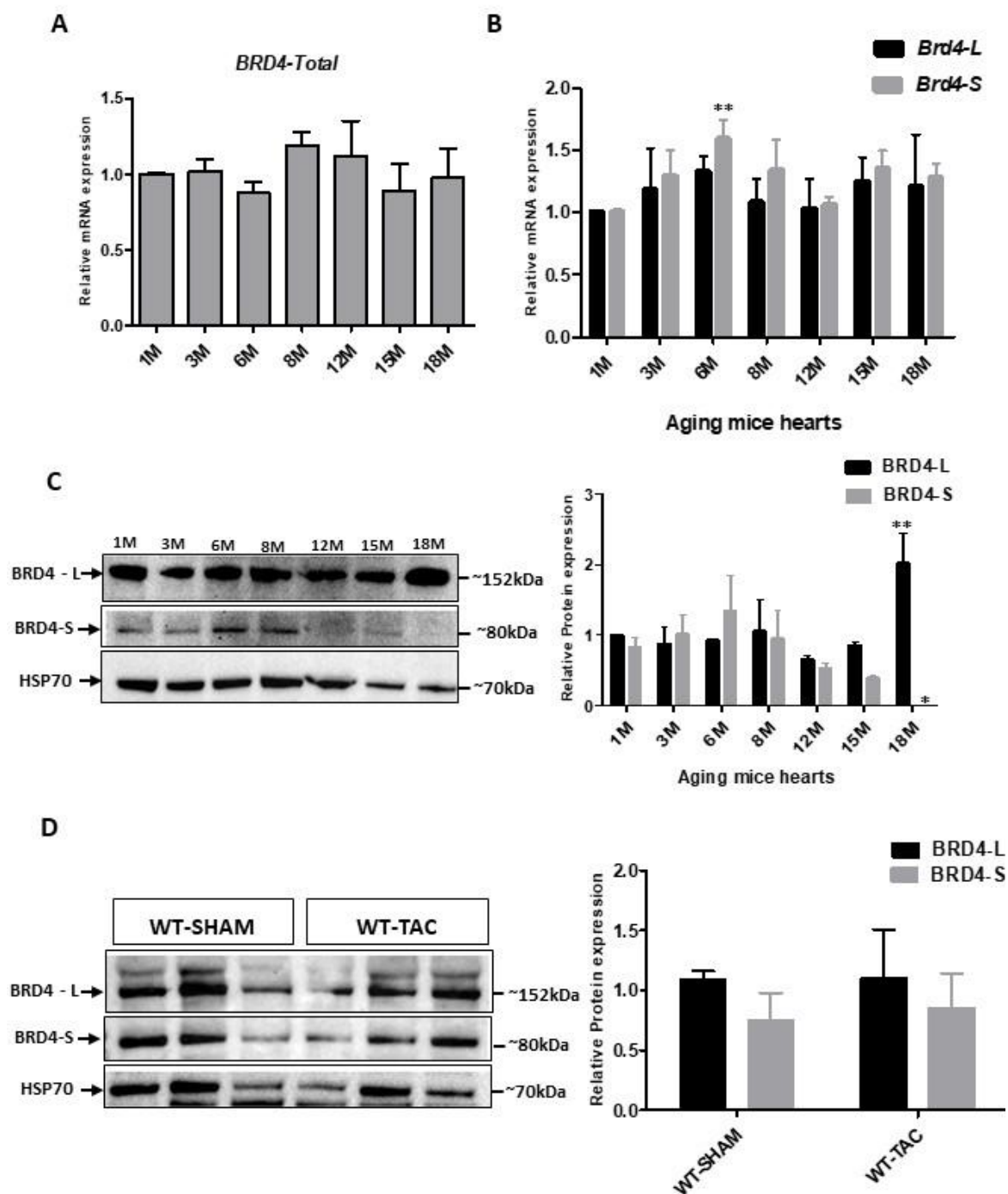
Figure 3.7. Expression of BRD4 isoforms in mice hearts. Bar graph showing relative mRNA level of Brd4-Total normalised to house-keeping gene, Gapdh (**A**) and, *Brd4-L* and *Brd4-S* isoforms normalised first to house-keeping gene *Gapdh* and then normalised to Brd4 total (**B**) in 1-, 3-, 6-, 8-, 12-, 15-, and 18- months old mice hearts. **C and D,** Western blot image (left Panels) and the corresponding relative quantification bar graph (right Panels) showing the protein expression of BRD4-L and BRD4-S in 1- to 18-months old mice (**C**) and in WT-SHAM and WT-TAC mice hearts (**D**). Immunoblotting for β-actin was used as a loading control. The band intensities of BRD4-L and BRD4-S were normalized to β-actin. Values are mean ± SEM of three (two in B) biological replicates and asterisks indicate statistical significance of ** $p<0.01$ and * $p<0.05$.

In mouse models of CVDs, we found indecisive results that BRD4-L isoform expression is

high in 18M old mice as compared to earlier stages. However, BRD4-S was not detectable

after 8-months of age. Likewise, there was no significant difference of BRD4-L and BRD4-S isoforms in cardiac hypertrophic mice hearts (TAC) as compared to SHAM mice. This data may indicate that BRD4 isoforms expression do not vary during cardiac remodelling of hearts in hypertrophy. After expression analysis of BRD4 isoforms, we further investigated the role of BRD4 in monolayer integrity of ECs.

3.4 Identifying the role of BRD4 and Midkine in monolayer integrity of endothelium

3.4.1 Effect of inflammatory phenotype on HUVECs monolayer integrity

It has been reported that TNF-α treatment results in increased permeability and monolayer disruption in vascular ECs (Friedl *et al.,* 2002; Royall *et al.,* 1989). Likewise, retinal ECs also lose monolayer integrity because of disruption of tight junctions via activation of NF-κB signalling (Aveleira *et al.,* 2010). In order to analyse the effect of TNF-α treatment on HUVECs monolayer integrity, we used Trans-Endothelial/Epithelial Electrical Resistance (TEER) measurement test and the change in electrical resistance as an indicator of monolayer integrity. To perform TEER measurements, HUVECs were grown on 0.4 µM pore size transwell membranes for 3-5 days until cells formed the monolayer and showed a reference value of ~80 $\Omega.cm^2$ (Callahan *et al.,* 2004; Kazakoff *et al.,* 1995; Man *et al.,* 2008; Srinivasan *et al.,* 2015). Afterwards, HUVEC monolayers were treated with either with DMSO or TNF-α for 12 hrs and measured for electrical resistance at different time intervals (0-, 3-, 6-, and 12 hrs). There was a significantly reduced electrical resistance across TNF-α treated monolayer compared to control (DMSO) treated monolayer, indicating increased permeability and loss of monolayer integrity in TNF-α treated cells (Fig. 3.8).
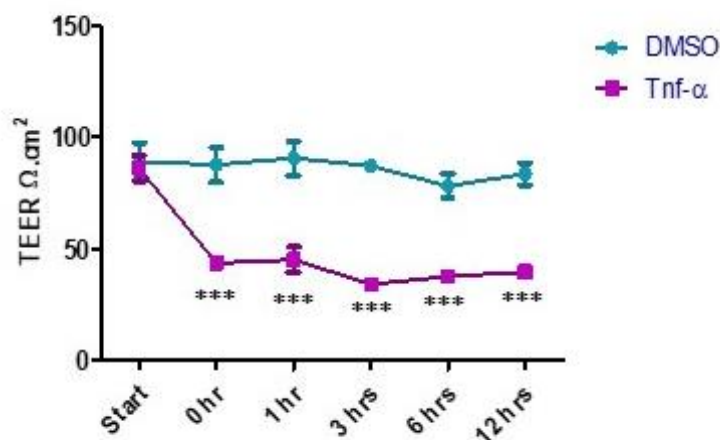
Figure 3.8. Disruption of monolayer integrity in HUVECs : HUVECs were grown on 0.45 µM transwell membrane for 5 days to establish the monolayer. Line graph shows Transepithelial/endothelial electrical resistance (TEER) measured in HUVECs monolayer treated with DMSO and TNF-α for 12 hrs. Values are mean ± SEM of three biological replicates and asterisks indicate statistical significance of *** $p < 0.001$.

Next, we were interested to study whether BRD4 inhibition could preserve the monolayer integrity in TNF-α treated monolayer as BRD4 inhibition is shown to reduce the inflammatory response, which is known to be associated with monolayer disruption.

3.4.2 BRD4 inhibition protects HUVECs monolayer integrity

To analyse the effect of BRD4 inhibition on monolayer integrity, HUVECs monolayers were treated with DMSO-only-, TNF-α-only-, RVX208-only-, and RVX208 followed by TNF-α. Similarly, the second set of monolayers was treated with JQ1 instead of RVX208. After the indicated treatments, the monolayers were subjected to TEER measurement at different time intervals. As expected, TNF-α treated cells showed significantly reduced electrical resistance as compared to control (DMSO). Surprisingly, when HUVEC monolayers were pre-treated with JQ1 or RVX208 followed by treatment with TNF-α, we found no change in

resistance across the monolayer (Fig. 3.9A-B). Hence, these results indicate that BRD4 inhibition is also protecting the HUVECs monolayer integrity from inflammatory response.
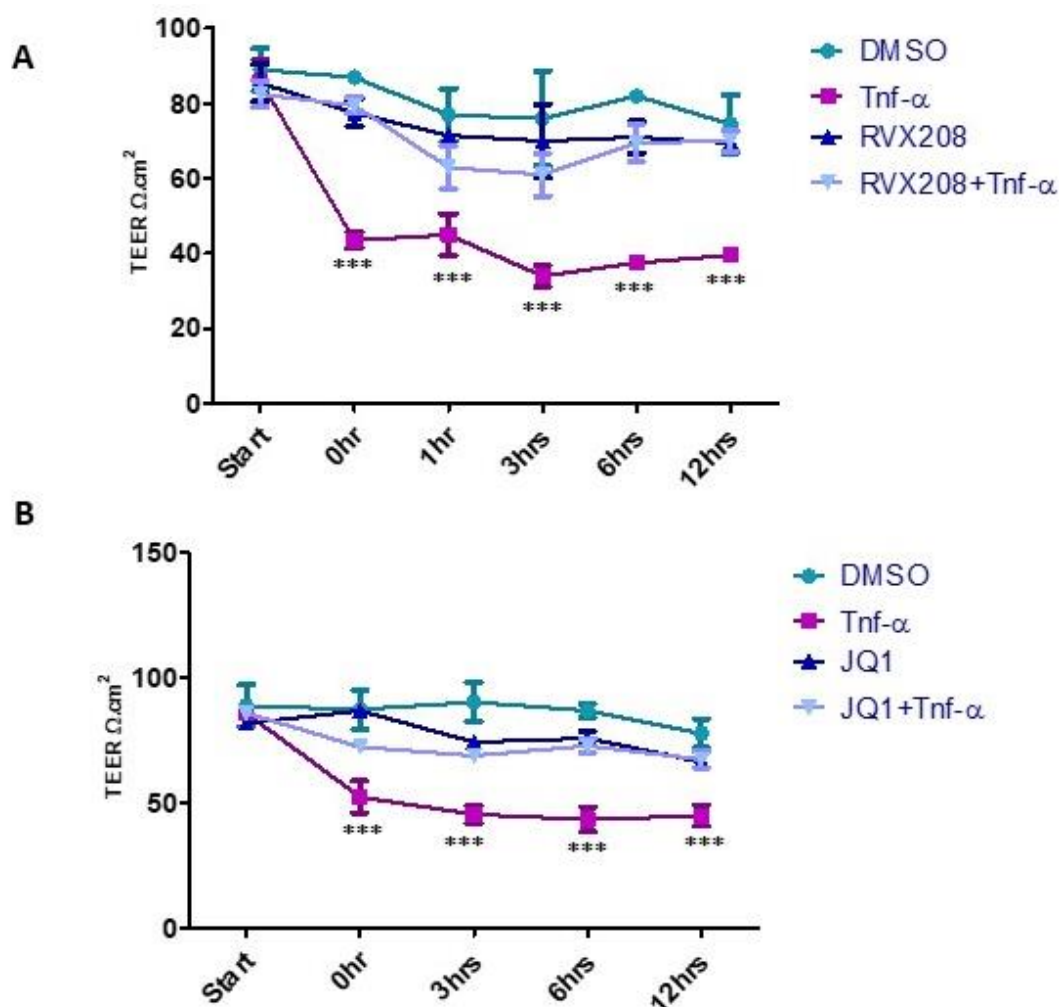
Figure 3.9. BRD4 inhibition, protects monolayer integrity in HUVECs. HUVECs were grown on 0.45 µM transwell membrane for 5 days to establish the monolayer Line graphs showing Transepithelial/endothelial electrical resistance (TEER) measured in HUVEC monolayers treated with DMSO, TNF-α-only, RVX208-only and RVX208+TNF-α (**A**), and with DMSO, TNF-α-only, JQ1-only and JQ1+TNF-α (**B**). Values are mean ± SEM of three biological replicates and asterisks indicate statistical significance of *** $p < 0.001$.

Next, we wanted to investigate the mechanism through which BRD4 inhibition is preserving the monolayer integrity. Here we would like to highlight that our group has previously shown that increased monolayer permeability is associated with Midkine/PI3K pathway in human epithelial colorectal adenocarcinoma cells (Caco-2 cells) (Khan *et al.,* 2017). To evaluate whether the same mechanism/pathway is responsible for the loss of monolayer integrity in HUVECs, we decided first to analyse mRNA expression of these genes during inflammation. HUVECs were grown for 4-5 days to attain monolayer and then were treated

with TNF-α for 2 and 12 hrs. Induced mRNA expression levels of pro-inflammatory gene (*SELE*) in TNF-α treated monolayers confirmed the inflammatory phenotype as compared to non-treated control monolayers (Fig. 3.10A). Then the expression of *p38MAP Kinase* (*p38MAPK*) and *MIDKINE* was measured (Fig. 3.10B). As our data indicated higher expression of *p38MAPK* and *MIDKINE* in TNF-α treated monolayers, we decided to explore the role of *MIDKINE*, which is an upstream regulator of p38MAPK, in conjunction with BRD4 in our experimental setup.
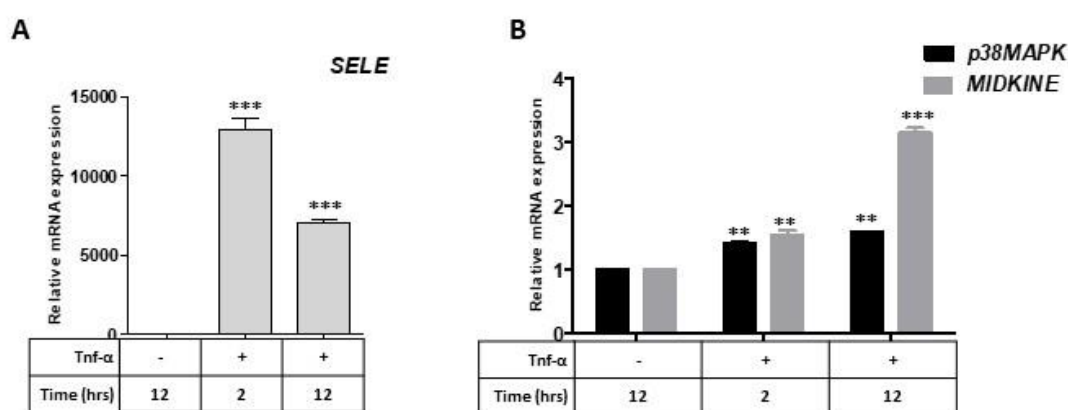
Figure 3.10. Induction of *MIDKINE* and *p38MAPK* expression in HUVECs: A, Bar graph showing mRNA levels of *SELE* after normalisation to house-keeping gene *GAPDH* in Control (non-treated) and in TNF-α treated (2hrs and 12hrs) monolayers. **B,** Bar graph showing mRNA levels of *P38MAPK* and *MIDKINE* after normalisation to house-keeping gene *GAPDH* in non-treated control and in TNF-α treated (2 hrs and 12 hrs) monolayers. Values are mean ± SEM of two biological replicates and asterisks indicate statistical significance of *** $p < 0.001$.

3.4.3 TNF-α induces the expression of Midkine

Endothelium releases a basal level of Midkine, a cytokine, in normal healthy state, where it is known to play a role in angiogenesis, apoptosis, growth and repair of damaged tissues (Kadomatsu *et al.,* 2014; Salaru *et al.,* 2016). Increased expression of Midkine has been reported in inflammatory kidney disease and atherosclerosis (Kadomatsu *et al.,* 2014; Salaru *et al.,* 2013; Salaru *et al.,* 2016). Hence, we decided to check Midkine expression in HUVEC monolayers treated with 20 ng/ml TNF-α for 6-, 12-, 24-, 48-, and 72- hrs. The mRNA expression of *MIDKINE* was significantly high after 6 hrs of TNF-α treatment and it steadily increased until 72hrs of treatment (Fig. 3.11A).

Western blot analysis on total protein extracts of above treatments failed to detect the band corresponding to MIDKINE (Fig. 3.11B). Midkine is released from cell and acts as a signalling molecule, so we checked the cell culture medium supernatants of HUVEC

monolayer for MIDKINE protein. This analysis indicated that Midkine protein secretion was significantly high in HUVECs treated with TNF-α for 48 hrs-72 hrs (Fig. 3.11C).
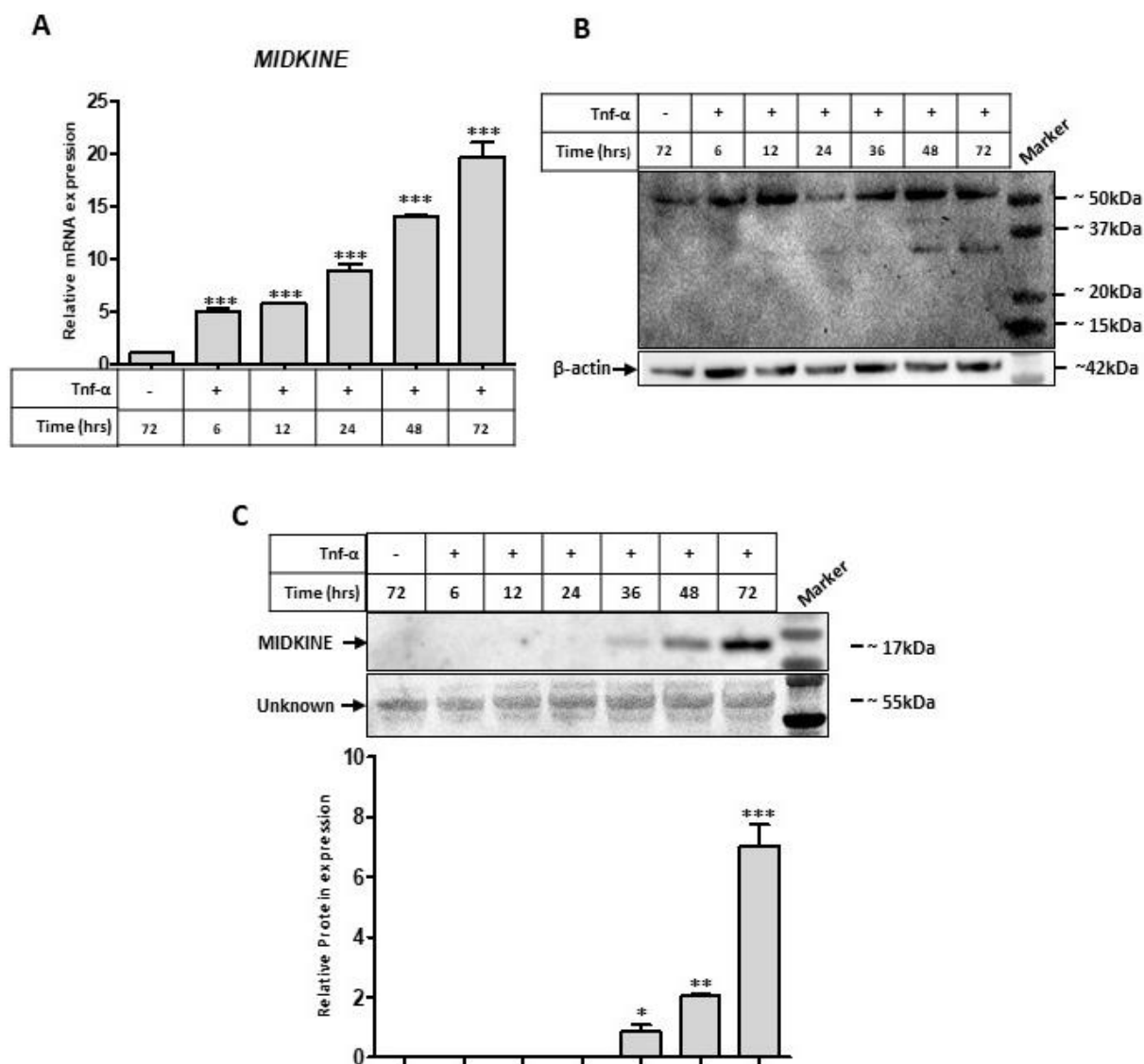
Figure 3.11. Midkine expression in HUVEC monolayer during TNF-α treatment: A, Bar graph showing relative mRNA levels of *MIDKINE* after normalization to house-keeping gene, *GAPDH*, in control and after different times of TNF-α treatments (6-, 12-, 24-, 48- and 72-hrs). **B,** Western Blot showing MIDKINE and β-actin expression in control and TNF-α treatments (6-, 12-, 24-, 48- and 72-hrs). **C,** Western blot image (upper panel) and the corresponding relative quantification bar graph showing the protein expression of MIDKINE secretion (lower panel) in control and TNF-α treatments (6-, 12-, 24-, 36-, 48-, and 72hrs). Ponceau staining of the Western blot membrane showing a band of unknown identity at ~55 kDa as a loading control. Values are mean ± SEM of three biological replicates and asterisks indicate statistical significance of *** $p < 0.001$ and ** $p < 0.01$.

This finding together with our previous observation that Midkine disrupts tight junctions and monolayer integrity in Caco-2 monolayer (Khan *et al.,* 2017), made us to conclude that

Midkine could be the reason for disruption of tight junctions in HUVEC monolayers, as well. Hence, it would be interesting to analyse the effect of BRD4 inhibition on MIDKINE expression and the monolayer integrity properties of HUVECs.

3.4.4 BRD4 inhibition reduces the expression of Midkine

To study the effect of BRD4 inhibition on Midkine expression, HUVEC monolayers were pre-treated either with or without RVX208 or JQ1 for 12 hrs before treating them with TNF-α for 6-, 12-, 24-, 36-, 48- and 72-hrs. RNA expression analysis showed significantly reduced expression of *MIDKINE* in monolayers pre-treated with Inhibitor (RVX208 or JQ1) followed by TNF-α treatment compared to TNF-α-only treated monolayers (Fig. 3.12A and B respectively).

A

MIDKINE

Tnf-α	-	+	+	+	+	+	-	+	+	+	+	+
Time (hrs)	72	6	12	24	48	72	-	6	12	24	48	72
RVX	-	-	-	-	-	-	+	+	+	+	+	+

B

C
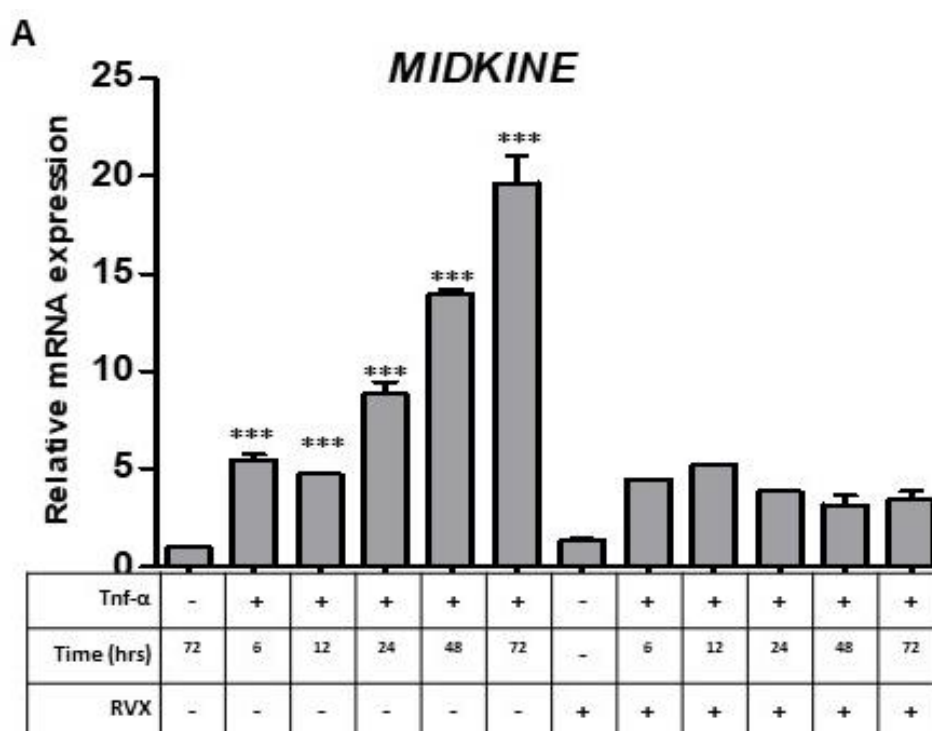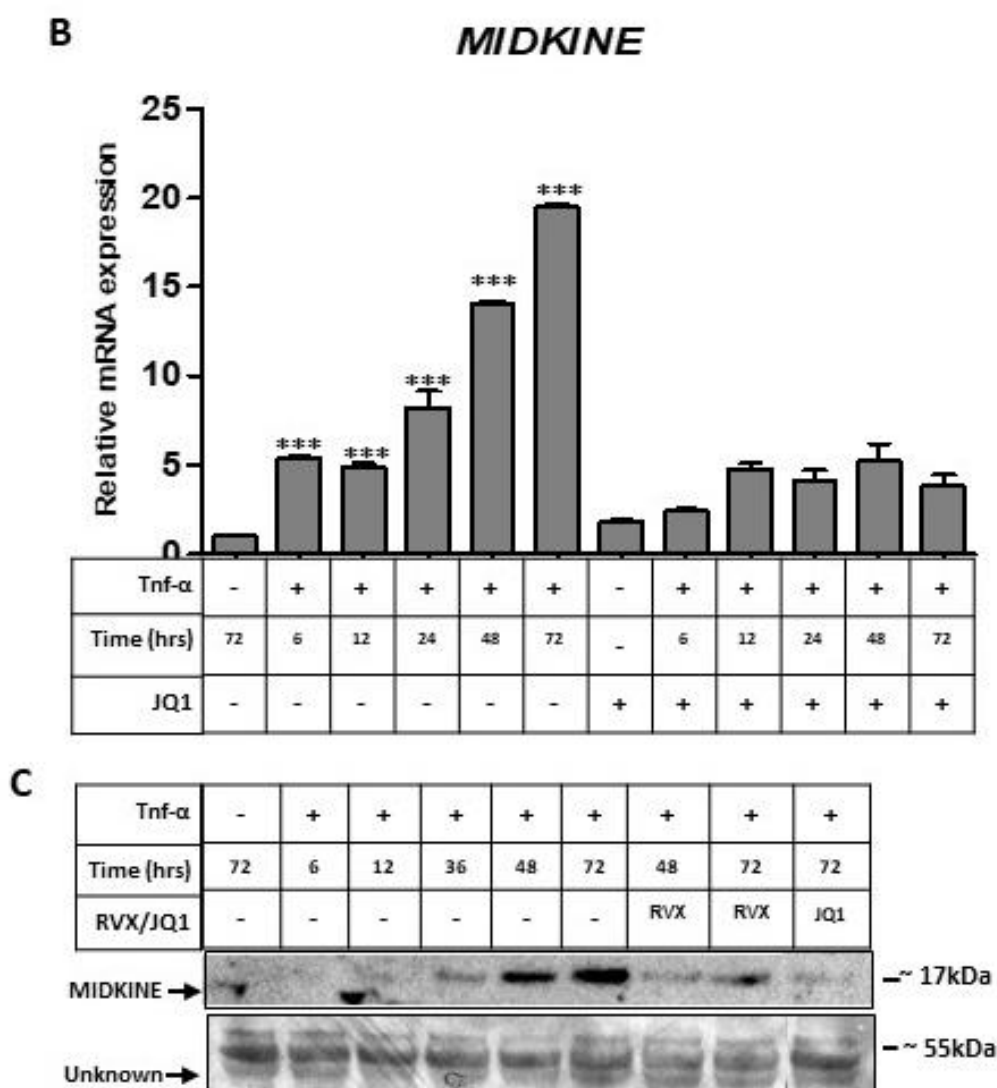
Figure 3.12. Midkine inhibition in HUVECs with BRD4 inhibitors A, Bar graph showing relative mRNA levels of *MIDKINE* after normalization to house-keeping gene *GAPDH*, in control and TNF-α treatments (6-, 12-, 24-, 48- and 72-hrs), RVX 208 treatment and pre-treatment with RVX208 followed by TNF-α (6-, 12-, 24-, 36-, 48-, and 72-hrs). **B,** Bar graph showing relative mRNA levels of *MIDKINE* after normalization to house-keeping gene *GAPDH*, in control and TNF-α treatments (6-, 12-, 24-, 48- and 72-hrs), JQ1 treatment and pre-treatment with JQ1 followed by TNF-α (6-, 12-, 24-, 36-, 48-, and 72-hrs) .**C,** Western blot image showing the protein expression of MIDKINE secretion (upper panel) in control, TNF-α treatments (36-, 48-, and 72-hrs), Pre-treatment with RVX208 or JQ1 followed by 48- and 72-hrs of TNF-α treatment. Ponceau staining (lower panel) of the Western blot membrane showing a band of unknown identity at ~55kDa as a loading control. Values are mean ± SEM of three biological replicates and asterisks indicate statistical significance of *** $p < 0.001$, ** $p < 0.01$ and * $p < 0.05$.

Next, we checked the supernatants of HUVEC monolayer cultures for secreted Midkine protein. Monolayers were treated either with RVX208 or JQ1 or were treated with RVX208 or JQ1 followed by TNF-α treatment for 48 and 72 hrs. Protein secretion of MIDKINE was significantly reduced in cells pre-treated with BRD4 inhibitor followed by TNF-α treatment, as compared to TNF-α-only treatment (Fig. 3.12C). Our results indicate that Midkine

expression and secretion was significantly high in response to TNF-α treatment. However, BRD4 inhibition via JQ1 or RVX208, decreases the expression of Midkine during TNF-α treatment. These results indicate that MIDKINE might be another target of BRD4 during inflammatory response in HUVECs and inhibition of BRD4 results in decreased expression of MIDKINE.

Collectively, we can conclude that BRD4 inhibition not only alleviates the inflammatory response in HUVECs but also preserves endothelial monolayer integrity via reducing the Midkine expression.

3.5 Expression of PTP1B increases in ECs during inflammation

Protein Tyrosine Phosphatase 1B (PTP1B) is another protein which has higher expression during inflammation (Zabolotny *et al.,* 2008). And enhanced expression of PTP1B in ECs is associated with reduced angiogenesis and reduced expression of endothelial specific nitric oxide synthase (eNOS) (Besnier *et al.,* 2014; Lanahan *et al.,* 2014). Then we want to analyse whether PTP1B is highly expressed also in our *in-vitro* inflammatory model. For this reason, we treated the HUVECs with TNF-α for 2 hrs and analysed the mRNA level of PTP1B. We found no significant expression difference of *PTP1B* in control and TNF-α treated cells. So, then we treated HUVECs with TNF-α for various time points (6-,12-, and 24-hrs) and found significant up-regulation of *PTP1B* mRNA levels already by 6 hrs of treatment, which is further increased by 24 hrs (Fig. 3.13 A).

Next, we performed the western blot analysis using anti-PTP1B antibody and found significantly increase in expression of PTP1B protein only after 24 hrs of TNF-α treatment (Fig. 3.13B). These results highlight that PTP1B is up-regulated during inflammatory response in ECs.
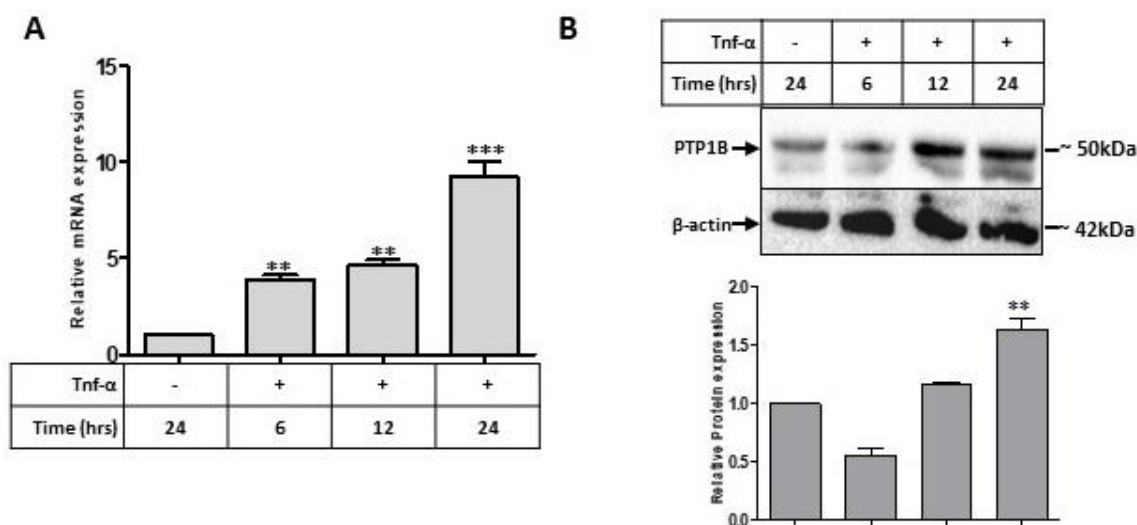
Figure 3.13. Induction of PTP1B expression in HUVECs. A, Bar graph showing relative mRNA levels of *PTP1B* after normalization to house-keeping gene *GAPDH* in control, and TNF-α treatments (6-, 12- and 24-hrs). **B,** Western blot image (upper panel) and the corresponding relative quantification bar graph (lower panel) showing the protein expression of PTP1B in control and TNF-α treated (6-, 12- and 24-hrs). Immunoblotting for β-actin was used as a loading control. The band intensities of Midkine were normalized to β-actin. Values are mean ± SEM of two biological replicates and asterisks indicate statistical significance of *** $p < 0.001$ and ** $p < 0.01$

In this context it is interesting to note that deletion or pharmacological inhibition of PTP1B in mice protects them against diabetes and obesity (Ali *et al.,* 2009) and hypertension (Bruder-Nascimento *et al.,* 2015). It has been reported that PTP1B deletion reduces endothelial dysfunction by improving Nitric oxide (NO) production, improves cardiac dysfunction and cardiac inflammation (Coquerel *et al.,* 2014). Importantly endothelial specific PTP1B deletion in mice (Endo.*Ptp1b.*KO) protected them against induced cardiac hypertrophy and fibrosis in TAC model (Gogiraju *et al.,* 2016). This finding prompted us to analyse the global proteome of heart tissues derived from Endo.*Ptp1b.*KO to identify possible targets/pathways of Ptp1b, which are responsible for the observed rescue.

3.6 Global Proteome analysis

In order to achieve a comparative global proteome profiling between Endo.*Ptp1b.*KO and Wild type (Endo.*Ptp1b.*WT) mouse hearts, the strategy illustrated in figure 3.11 was employed. Briefly, mice with *loxP* flanked *Ptp1b* allele (*Ptp1b^{fl/fl}*) were bred either with Wild type mice or with transgenic mice expressing a fusion protein of *Cre* recombinase-estrogen receptor under the control of endothelial receptor tyrosine kinase promoter

(*Tie2.ERT2.Cre*). The off-spring were then fed with Tamoxifen diet to induce Cre recombinase activity. Afterwards, 10-12 weeks-old females WT and KO females were subjected to TAC or SHAM surgery (Fig. 3.14). In TAC group, a band is placed around the aorta of mice to induce pressure on heart, while SHAM mice (an experimental control) group also underwent surgery although aortic arch was exposed but no band was placed around the aorta. This strategy gave rise to four groups of animals namely: 1. Wild-type SHAM (WT-SHAM), 2. Wild-type TAC (WT-TAC), 3. Endothelial-specific *Ptp1b* knockout SHAM (KO-SHAM), and 4, Endothelial-specific *Ptp1b* knockout TAC (KO-TAC). After 20 weeks of TAC/SHAM surgery, five independent animals were taken from each group as biological replicates and whole heart tissue lysates were prepared in the presence of protease and phosphatase inhibitors (Fig. 3.14). Afterwards, 50 µg of proteins were tryptic digested and the resulting peptides were subjected to liquid chromatography-tandem mass spectrometry (LC-MS/MS) analysis.
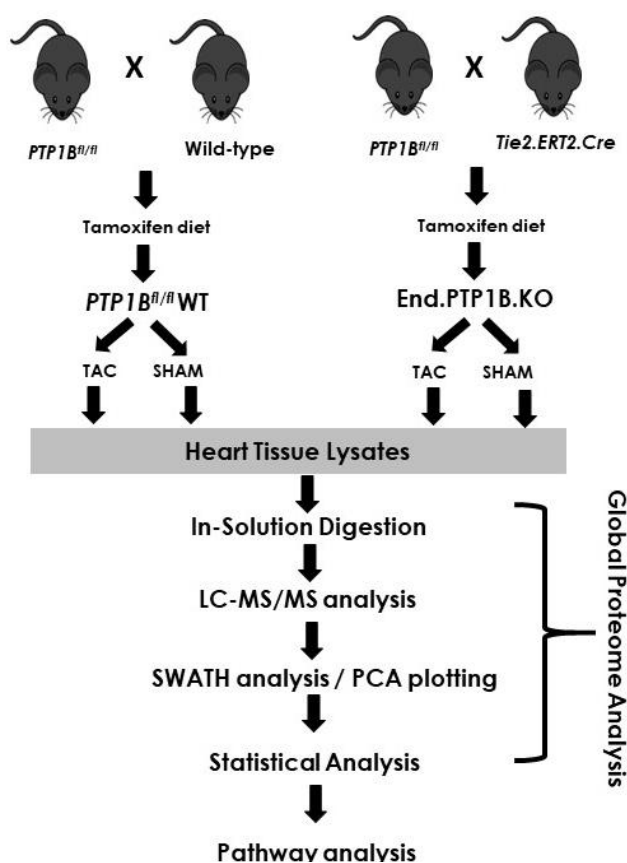
Fig. 3.14. Schematic illustration of strategy for global proteome analysis. *Ptp1b*fl/fl mice were either crossed with Wild type or with transgenic Tie2.ERT2.Cre mice and the resulting off-spring (6-week-old) were fed with tamoxifen diet for other 6-weeks to induce Cre-recombinase activity and to obtain Endo.*Ptp1b*.WT or Endo.*Ptp1b*.KO mice, respectively. Both animal groups underwent the TAC or SHAM surgery and gave rise to four groups: WT-TAC, WT-SHAM, KO-SHAM and KO-TAC. Total heart proteins were tryptic digested and identified by LC-MS/MS analysis and quantified by SWATH

analysis. Then Perseus based statistical analysis was employed to identify the significant proteins. STRING pathway analysis was performed to identify the sub-cellular localization of proteins for better understanding of their functions.

Following the data acquisition, we performed quantitative proteome analysis by using **S**equential **W**indow **A**cquisition of all **TH**eoretical fragment ion spectra (SWATH) in data independent acquisition (DIA) mode. Overall, we identified a total of 899 common proteins in all four groups and quantified 697 proteins with 1% False Discovery Rate (FDR). Then, we analysed all 697 proteins by using directed Principal Component Analysis (PCA) to get an overview of variability in our data. We observed four clusters representing four analysed groups with all the biological and technical replicates falling into their respective clusters (Fig. 3.15). WT-SHAM and KO-SHAM were more closely clustered to each other, indicating less variability among the SHAM groups. Interestingly, TAC groups (KO-TAC and WT TAC) represented two distinct clusters, highlighting that the rescue of cardiac overload has a different proteome (Fig. 3.15).
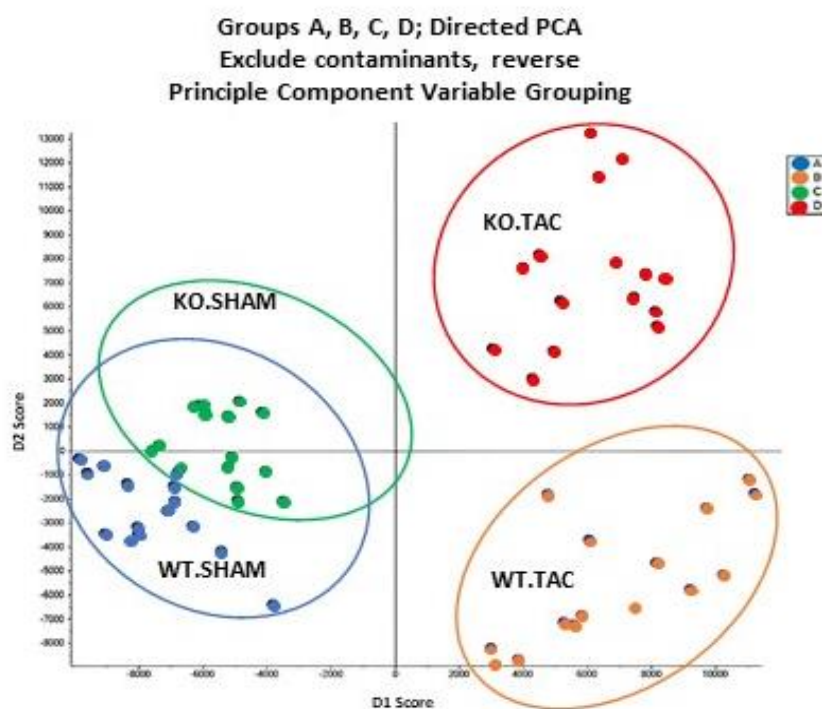
Fig. 3.15. Global proteome analysis: PCA analysis based on whole-proteome levels, which confirmed the presence of the 4 different groups. Different groups were assigned to proteins on basis of differential expression Blue colour represents WT-SHAM group, Orange colour represents WT-TAC, Green colour represents KO-SHAM and Red colour represents KO-TAC group.

3.6.1 Statistical Analysis using Perseus Software

After-knowing that KO-TAC and WT-TAC mice had a different proteome compared to SHAM groups, we decided to perform statistical analysis using Perseus software to identify proteins that have significant expression differences. For this reason, we compared the following groups:

Group A: WT-SHAM and KO-SHAM   **Group B:** WT-SHAM and WT-TAC

Group C: KO-SHAM and KO-TAC **Group D**: WT-TAC and KO-TAC

Next, we calculated p-values for all four groups followed by fold change calculation. We considered proteins with p values < 0.05 and fold change cut-off value of 1.5 as significantly different and used them for further analysis. In **Group A**, we found 8 proteins to be up-regulated, while 58 proteins to be down-regulated in KO-SHAM as compared to WT-SHAM (Table 3.1, 3.2, and Fig. 3.16) **In Group B**, 60 and 70 proteins were up- and down-regulated, respectively, (Table 3.3, 3.4, and Fig. 3.16) in WT-TAC as compared to WT-SHAM. **In Group C**, 150 proteins were up-regulated while 53 proteins were down-regulated in KO-TAC as compared to KO-SHAM, (Tables 3.5, 3.6, and Fig. 3.16). **In Group D:** 43 proteins were up-regulated while 36 were down-regulated in KO-TAC as WT-TAC (Table 3.7, 3.8, and Fig. 3.16).
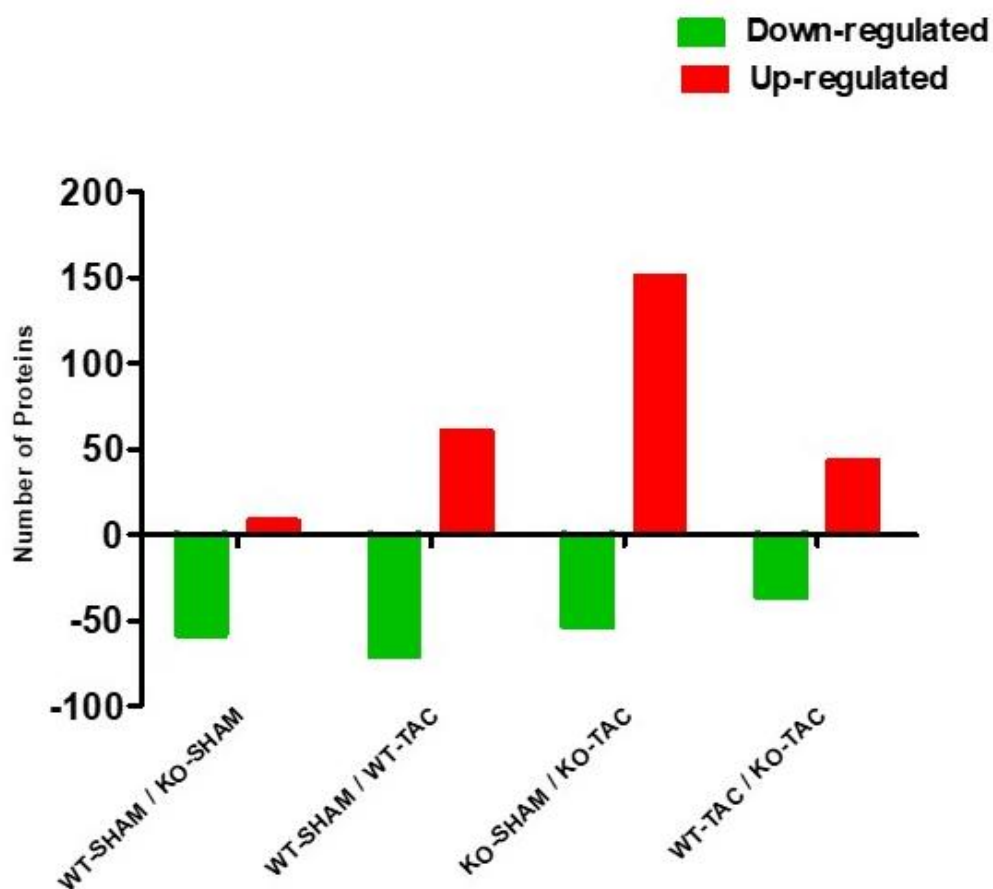
Figure 3.16. Statistical summary of Global proteome analysis: Bar graph indicating number of up-regulated (red) and down-regulated (green) proteins in all four groups. The number of proteins in bar graph denote those that reached statistical significance using Welch's T-test.

Next, we converted the p-values into -log10 (p-values) and fold change was converted in log2 (log2 FC) and volcano plots were plotted using -log10 of p-values against log2 of fold change (Fig. 3.17A-D).

Table 3.1

Group A: Up-regulated Proteins in KO-SHAM vs WT-SHAM		
Uniprot Accession	**Protein**	**Fold Change**
NDUA3_MOUSE	NADH dehydrogenase 1 alpha subcomplex subunit 3	9.261803
CXA1_MOUSE	Gap junction alpha-1 protein	2.333574
2AAA_MOUSE	Serine/threonine-protein phosphatase 2A 65 kDa regulatory subunit A alpha isoform	2.271057
Q7JCZ3_MOUSE	Cytochrome b	2.19333
A0A0G2JH00_MOUSE	Protein Igkv4-61	2.1896
MYL6_MOUSE	Myosin light polypeptide 6	1.99142

| NDUA7_MOUSE | NADH dehydrogenase 1 alpha subcomplex subunit 7 | 1.679112 |
| ACADS_MOUSE | Short-chain specific acyl-CoA dehydrogenase, mitochondrial | 1.588391 |

Table 3.2

Group A: Down-regulated Proteins in KO-SHAM vs WT-SHAM		
Uniprot Accession	**Protein**	**Fold Change**
SPA3K_MOUSE	Serine protease inhibitor A3K	5.724768
Q3UER8_MOUSE	Fibrinogen gamma chain	5.59055
Q58E64_MOUSE	Elongation factor 1-alpha	4.41397
Q9CPX4_MOUSE	Ferritin	4.184854
Q52L87_MOUSE	Tubulin alpha-1C chain	3.284082
Q58E35_MOUSE	60S acidic ribosomal protein P1	3.249365
E9Q5L2_MOUSE	Inter alpha-trypsin inhibitor, heavy chain 4	3.172823
Q149V4_MOUSE	Histone H2A	2.851051
AN32A_MOUSE	Acidic leucine-rich nuclear phosphoprotein 32 family member A	2.690346
D3Z576_MOUSE	Filamin-C	2.55819
FIBA_MOUSE	Fibrinogen alpha chain	2.505103
COF1_MOUSE	Cofilin-1	2.465072
Q5DQJ3_MOUSE	Capping protein (Actin filament) muscle Z-line, alpha 2, isoform CRA_c	2.453384
GNAS1_MOUSE	Guanine nucleotide-binding protein G(s) subunit alpha isoforms XLas	2.332206
A2AFJ1_MOUSE	Histone-binding protein RBBP7	2.283441
Q546K1_MOUSE	Cytoglobin	2.23178
RTN2_MOUSE	Isoform 2 of Reticulon-2	2.221354
PP1B_MOUSE	Serine/threonine-protein phosphatase PP1-beta catalytic subunit	2.218909
Q8BVQ9_MOUSE	26S protease regulatory subunit 7	2.188379
SDCG8_MOUSE	Serologically defined colon cancer antigen 8 homolog	2.157165
RS9_MOUSE	40S ribosomal protein S9	2.09963
A4FUS1_MOUSE	40S ribosomal protein S16	2.052678
Q8C5G6_MOUSE	Toll-interacting protein	2.029818
Q5SUC3_MOUSE	Calnexin	2.009529
A0A075B6A0_MOUSE	Ig mu chain C region	2.008865
S4R1E5_MOUSE	Glutathione peroxidase	2.006824
ANXA3_MOUSE	Annexin A3	1.970541
TERA_MOUSE	Transitional endoplasmic reticulum ATPase	1.908613
Q499X4_MOUSE	Synaptic vesicle membrane protein VAT-1 homolog	1.900839
A3KGQ6_MOUSE	Actin-related protein 2/3 complex subunit 5	1.857499
Q3U4U6_MOUSE	T-complex protein 1 subunit gamma	1.843001
Q792A4_MOUSE	Cox7ah	1.834669
A0A087WS46_MOUSE	Elongation factor 1-beta	1.830365

HSPB2_MOUSE	Heat shock protein beta-2	1.825187
Q564E8_MOUSE	60S ribosomal protein L4	1.806892
Q545X8_MOUSE	40S ribosomal protein S4	1.798365
DNJB4_MOUSE	DNA homolog subfamily B member 4	1.794935
TM14C_MOUSE	Transmembrane protein 14C	1.781072
Q3U367_MOUSE	4-trimethylaminobutyraldehyde dehydrogenase	1.756965
GRPE1_MOUSE	GrpE protein homolog 1, mitochondrial	1.749118
A0A0H2UH17_MOUSE	Ubiquitin associated protein 2-like, isoform CRA_b	1.72855
Q5M8M8_MOUSE	60S ribosomal protein L29	1.704919
G5E8J6_MOUSE	Histidine rich calcium binding protein, isoform CRA_a	1.694952
Q543B9_MOUSE	Prolyl endopeptidase	1.684433
CAND1_MOUSE	Cullin-associated NEDD8-dissociated protein 1	1.678813
Q5M9J2_MOUSE	Histidine triad nucleotide binding protein 2	1.663793
CD47_MOUSE	Leukocyte surface antigen CD47	1.662129
RL27A_MOUSE	60S ribosomal protein L27a	1.648814
TNNC1_MOUSE	Troponin C, slow skeletal and cardiac muscles	1.632444
USMG5_MOUSE	Up-regulated during skeletal muscle growth protein 5	1.60865
Q3UCD9_MOUSE	Cathepsin D	1.604517
A0A0U1RQ27_MOUSE	Methylmalonyl CoA epimerase, isoform CRA_c	1.573786
B9EHN0_MOUSE	Ubiquitin-activating enzyme E1, Chr X	1.573732
Q3TJY2_MOUSE	WD repeat domain 1	1.573184
E9Q7N5_MOUSE	Ribosome-releasing factor 2, mitochondrial	1.551304
VTDB_MOUSE	Vitamin D-binding protein	1.543408
GDIR1_MOUSE	Rho GDP-dissociation inhibitor 1	1.542594
Q3UL22_MOUSE	Chaperonin subunit 8 (Theta), isoform CRA_a	1.524054

Table 3.3

Group B: Up-regulated Proteins in WT-TAC vs WT-SHAM		
Uniprot Accession	**Protein**	**Fold Change**
B2RXX9_MOUSE	Myosin, heavy polypeptide 7, cardiac muscle, beta	22.46804
A2AEX8_MOUSE	Four and a half LIM domains 1, isoform CRA_b	4.475918
Q8BFQ1_MOUSE	Prosaposin	3.895401
APOA2_MOUSE	Apolipoprotein A-II	3.506413
Q546K1_MOUSE	Cytoglobin	3.194436
NDUA3_MOUSE	NADH dehydrogenase 1 alpha subcomplex subunit 3	2.944347
D9J302_MOUSE	ENH isoform 1e	2.922764
TBB5_MOUSE	Tubulin beta	2.672675
NDUB2_MOUSE	NADH dehydrogenase 1 beta subcomplex subunit 2, mitochondrial	2.565567
Q4FJQ6_MOUSE	Serine (Or cysteine) peptidase inhibitor, clade B, member 6a, isoform CRA_a	2.548441
H7BX64_MOUSE	Sarcolemmal membrane-associated protein	2.520141
G5E8T9_MOUSE	Hydroxyacyl glutathione hydrolase	2.472386

Q7JCZ3_MOUSE	Cytochrome b	2.44693
E9QLZ9_MOUSE	Protein enabled homolog	2.410786
G3X9L6_MOUSE	MCG55033	2.36428
A0A0A6YWR2_MOUSE	Ig gamma-1 chain C region secreted form	2.243095
UGPA_MOUSE	UTP--glucose-1-phosphate uridylyltransferase	2.227797
TXD17_MOUSE	Thioredoxin domain-containing protein 17	2.17689
F6ZFU0_MOUSE	Elongation factor 1-delta	2.131331
HEMO_MOUSE	Hemopexin	2.129784
HDHD2_MOUSE	Haloacid dehalogenase-like hydrolase domain-containing protein 2	2.074073
ANXA7_MOUSE	Annexin A7	2.073107
Q6YJU1_MOUSE	Fetuin-B	1.985978
STIP1_MOUSE	Stress-induced-phosphoprotein 1	1.984306
CAH1_MOUSE	Carbonic anhydrase 1	1.964014
S4R1E5_MOUSE	Glutathione peroxidase	1.961202
TOM70_MOUSE	Mitochondrial import receptor subunit TOM70	1.925854
OBSCN_MOUSE	Obscurin	1.912945
PSA6_MOUSE	Proteasome subunit alpha type-6	1.904566
F6TCV0_MOUSE	Serine protease HTRA2, mitochondrial	1.896703
Q3T9Z2_MOUSE	Glyoxylate reductase/hydroxypyruvate reductase	1.882532
SLIRP_MOUSE	SRA stem-loop-interacting RNA-binding protein, mitochondrial	1.877301
GCAM_MOUSE	Ig gamma-2A chain C region, membrane-bound form	1.873636
TIM13_MOUSE	Mitochondrial import inner membrane translocase subunit Tim13	1.869761
Q543M7_MOUSE	Importin subunit alpha	1.850016
Q545C7_MOUSE	Cysteine and glycine-rich protein 3	1.848998
Q542Y0_MOUSE	NAD(P)H dehydrogenase [quinone] 1	1.803744
ENOB_MOUSE	Beta-enolase	1.801966
Z4YK42_MOUSE	NAD kinase 2, mitochondrial	1.786285
MIRO1_MOUSE	Isoform 4 of Mitochondrial Rho GTPase 1	1.779831
F6WYM0_MOUSE	Septin-2	1.776692
A0A0G2JH00_MOUSE	Protein Igkv4-61	1.770807
HSPB6_MOUSE	Heat shock protein beta-6	1.759373
MYL1_MOUSE	Myosin light chain 1/3, skeletal muscle isoform	1.757874
E9Q616_MOUSE	Protein Ahnak	1.751377
OLA1_MOUSE	Obg-like ATPase 1	1.74836
PYRD_MOUSE	Dihydroorotate dehydrogenase (quinone), mitochondrial	1.735936
GPD1L_MOUSE	Isoform 2 of Glycerol-3-phosphate dehydrogenase 1-like protein	1.702011
A2AIW9_MOUSE	Mitochondrial-processing peptidase subunit alpha	1.684361
A0A0G2JFH2_MOUSE	Microtubule-associated protein	1.681806
2AAA_MOUSE	Serine/threonine-protein phosphatase 2A 65 kDa regulatory subunit A alpha isoform	1.677898
F2Z456_MOUSE	NADH-cytochrome b5 reductase	1.657675
PDC6I_MOUSE	Programmed cell death 6-interacting protein	1.656956
BDH_MOUSE	D-beta-hydroxybutyrate dehydrogenase, mitochondrial	1.64578
D2KHZ9_MOUSE	Glyceraldehyde-3-phosphate dehydrogenase	1.633885

Q3TJY2_MOUSE	WD repeat domain 1	1.600595
DNJA2_MOUSE	DnaJ homolog subfamily A member 2	1.588696
B7ZCI2_MOUSE	Nebulette	1.584902
F8WIA1_MOUSE	CAP-Gly domain-containing linker protein 1	1.575521
E9Q3X0_MOUSE	Major vault protein	1.567592
LEG1_MOUSE	Galectin-1	1.566273

Table 3.4

Group B: Down-regulated Proteins in WT-TAC vs WT-SHAM		
Uniprot Accession	**Protein**	**Fold Change**
Q58E35_MOUSE	60S acidic ribosomal protein P1	7.177066
Q9CPX4_MOUSE	Ferritin	4.297613
A1BG_MOUSE	Alpha-1B-glycoprotein	4.065593
Q8BTU6_MOUSE	Eukaryotic initiation factor 4A-II	3.96271
G5E8J6_MOUSE	Histidine rich calcium binding protein, isoform CRA_a	3.869917
FRIH_MOUSE	Ferritin heavy chain	3.731264
Q52L87_MOUSE	Tubulin alpha-1C chain	3.45146
ABCB8_MOUSE	ATP-binding cassette sub-family B member 8, mitochondrial	3.345933
Q3U367_MOUSE	4-trimethylaminobutyraldehyde dehydrogenase	3.233596
KV3A4_MOUSE	Ig kappa chain V-III region 50S10.1	2.888454
SPA3K_MOUSE	Serine protease inhibitor A3K	2.837102
E9QMK9_MOUSE	Protein 9030617O03Rik	2.813919
THIM_MOUSE	3-ketoacyl-CoA thiolase, mitochondrial	2.793903
B2RUK5_MOUSE	Methylcrotonoyl-CoA carboxylase beta chain, mitochondrial	2.621667
CES1D_MOUSE	Carboxylesterase 1D	2.557144
A0A075B6A0_MOUSE	Ig mu chain C region	2.486141
RLA2_MOUSE	60S acidic ribosomal protein P2	2.451661
Q5DQJ3_MOUSE	Capping protein (Actin filament) muscle Z-line, alpha 2, isoform CRA_c	2.363354
ECI1_MOUSE	Enoyl-CoA delta isomerase 1, mitochondrial	2.353803
NDUB4_MOUSE	NADH dehydrogenase 1 beta subcomplex subunit 4	2.310692
Q4FK74_MOUSE	ATP synthase subunit delta, mitochondrial	2.270961
Q0PD66_MOUSE	RAB1B, member RAS oncogene family, isoform CRA_c	2.267102
CXA1_MOUSE	Gap junction alpha-1 protein	2.243188
NIT2_MOUSE	Omega-amidase NIT2	2.156661
Q32P04_MOUSE	Keratin 5	2.149984
A0A0U1RPI1_MOUSE	Phospholemman	2.125259
Q7JCX7_MOUSE	Cytochrome c oxidase subunit 3	2.097943
G3X9J1_MOUSE	Sodium/calcium exchanger 1	2.091153
LDHB_MOUSE	L-lactate dehydrogenase B chain	2.079872
NDUB1_MOUSE	NADH dehydrogenase 1 beta subcomplex subunit 1	2.04942
COQ3_MOUSE	Ubiquinone biosynthesis O-methyltransferase, mitochondrial	2.02944
Q3U7Z6_MOUSE	MCG113582	2.011059

LAMA2_MOUSE	Laminin subunit alpha-2	1.985002
ADCK3_MOUSE	Atypical kinase ADCK3, mitochondrial	1.960187
HHATL_MOUSE	Protein-cysteine N-palmitoyltransferase HHAT-like protein	1.927543
A0A0A0MQ68_MOUSE	Glutaryl-CoA dehydrogenase, mitochondrial	1.866263
ACOT2_MOUSE	Acyl-coenzyme A thioesterase 2, mitochondrial	1.865219
TERA_MOUSE	Transitional endoplasmic reticulum ATPase	1.861359
TACO1_MOUSE	Translational activator of cytochrome c oxidase 1	1.841498
TRAP1_MOUSE	Heat shock protein 75 kDa, mitochondrial	1.810444
CAD13_MOUSE	Cadherin-13	1.796888
ECHD2_MOUSE	Enoyl-CoA hydratase domain-containing protein 2, mitochondrial	1.775955
HCDH_MOUSE	Hydroxyacyl-coenzyme A dehydrogenase, mitochondrial	1.769064
PYGM_MOUSE	Glycogen phosphorylase, muscle form	1.768924
RM12_MOUSE	39S ribosomal protein L12, mitochondrial	1.757314
IVD_MOUSE	Isovaleryl-CoA dehydrogenase, mitochondrial	1.751905
RL14_MOUSE	60S ribosomal protein L14	1.72281
CD47_MOUSE	Leukocyte surface antigen CD47	1.714945
ECHB_MOUSE	Trifunctional enzyme subunit beta, mitochondrial	1.709272
CAV1_MOUSE	Caveolin-1	1.707292
Q80ZZ0_MOUSE	EH domain-containing protein 1	1.685678
USMG5_MOUSE	Up-regulated during skeletal muscle growth protein 5	1.670951
B2RS41_MOUSE	Aldhehyde dehydrogenase family 5, subfamily A1	1.670343
TMM65_MOUSE	Transmembrane protein 65	1.664084
CACP_MOUSE	Carnitine O-acetyltransferase	1.659263
NNRE_MOUSE	NAD(P)H-hydrate epimerase	1.647341
GSTK1_MOUSE	Glutathione S-transferase kappa 1	1.64678
Q14AZ9_MOUSE	Zinc binding alcohol dehydrogenase, domain containing 2	1.633292
CPT2_MOUSE	Carnitine O-palmitoyltransferase 2, mitochondrial	1.616862
MTFP1_MOUSE	Mitochondrial fission process protein 1	1.613282
ACADM_MOUSE	Medium-chain specific acyl-CoA dehydrogenase, mitochondrial	1.598459
F8WIT2_MOUSE	Annexin	1.589367
TNNC1_MOUSE	Troponin C, slow skeletal and cardiac muscles	1.584537
ECHA_MOUSE	Trifunctional enzyme subunit alpha, mitochondrial	1.576044
Q497X4_MOUSE	Cathepsin R	1.570785
Q569W4_MOUSE	Acetyl-coenzyme A synthetase	1.554089
B1AR28_MOUSE	Very long-chain-specific acyl-CoA dehydrogenase, mitochondrial	1.537874
E9Q800_MOUSE	MICOS complex subunit MIC60	1.527675
PDK2_MOUSE	[Pyruvate dehydrogenase (acetyl-transferring)] kinase isozyme 2, mitochondrial	1.523358

Table 3.5

Group C: Up-regulated Proteins in KO-TAC vs KO-SHAM		
Uniprot Accession	**Protein**	**Fold Change**

Q546K1_MOUSE	Cytoglobin	8.179658
B2RXX9_MOUSE	Myosin, heavy polypeptide 7, cardiac muscle, beta	7.751299
Q3UER8_MOUSE	Fibrinogen gamma chain	6.92076
NNTM_MOUSE	NAD(P) transhydrogenase, mitochondrial	6.404869
Q8C5G6_MOUSE	Toll-interacting protein	4.803583
S4R1E5_MOUSE	Glutathione peroxidase	4.76199
RTN2_MOUSE	Isoform 2 of Reticulon-2	4.211308
GNAS1_MOUSE	Guanine nucleotide-binding protein G(s) subunit alpha isoforms XLas	4.191142
Q58E64_MOUSE	Elongation factor 1-alpha	4.157227
Q792A4_MOUSE	Cox7ah	4.135588
F6TCV0_MOUSE	Serine protease HTRA2, mitochondrial	4.06327
Q3UP42_MOUSE	Protein S100-A9	3.921346
Q542X7_MOUSE	Chaperonin subunit 2 (Beta), isoform CRA_a	3.866951
Q8BH80_MOUSE	Vesicle-associated membrane protein, associated protein B and C	3.813203
A3KGQ6_MOUSE	Actin-related protein 2/3 complex subunit 5	3.709066
TM14C_MOUSE	Transmembrane protein 14C	3.630261
Q542I9_MOUSE	26S protease regulatory subunit 4	3.286168
PDIA1_MOUSE	Protein disulfide-isomerase	3.276221
SPA3K_MOUSE	Serine protease inhibitor A3K	3.256386
Q3UW66_MOUSE	Sulfurtransferase	3.194263
A2AFJ1_MOUSE	Histone-binding protein RBBP7	3.132479
A2AEX8_MOUSE	Four and a half LIM domains 1, isoform CRA_b	3.085688
E9Q5L2_MOUSE	Inter alpha-trypsin inhibitor, heavy chain 4	3.072361
E9Q7N5_MOUSE	Ribosome-releasing factor 2, mitochondrial	2.989694
D3Z576_MOUSE	Filamin-C	2.882748
ANXA3_MOUSE	Annexin A3	2.876219
TKT_MOUSE	Transketolase	2.855865
Q4FJQ6_MOUSE	Serine (Or cysteine) peptidase inhibitor, clade B, member 6a, isoform CRA_a	2.822981
Q6YJU1_MOUSE	Fetuin-B	2.779361
PYRD_MOUSE	Dihydroorotate dehydrogenase (quinone), mitochondrial	2.772408
DNJB4_MOUSE	DnaJ homolog subfamily B member 4	2.739464
HSPB2_MOUSE	Heat shock protein beta-2	2.739235
OLA1_MOUSE	Obg-like ATPase 1	2.72664
A2AIW9_MOUSE	Mitochondrial-processing peptidase subunit alpha	2.687923
Q5SUC3_MOUSE	Calnexin	2.665787
B1AX58_MOUSE	Plastin-3	2.637293
Q3TJY2_MOUSE	WD repeat domain 1	2.619171
D9J302_MOUSE	ENH isoform 1e	2.592252
HDHD2_MOUSE	Haloacid dehalogenase-like hydrolase domain-containing protein 2	2.579931
Q3UCD9_MOUSE	Cathepsin D	2.520039
Q5SW88_MOUSE	Protein Rab1a	2.514497
Z4YK42_MOUSE	NAD kinase 2, mitochondrial	2.498911

A0A0H2UH17_MOUSE	Ubiquitin associated protein 2-like, isoform CRA_b	2.497335
B2RTM0_MOUSE	Histone H4	2.495948
Q5M9J2_MOUSE	Histidine triad nucleotide binding protein 2	2.442678
ATOX1_MOUSE	Copper transport protein ATOX1	2.436779
Q91XH5_MOUSE	Sepiapterin reductase	2.39974
MIRO1_MOUSE	Isoform 4 of Mitochondrial Rho GTPase 1	2.379248
PP1B_MOUSE	Serine/threonine-protein phosphatase PP1-beta catalytic subunit	2.369575
Q3U4U6_MOUSE	T-complex protein 1 subunit gamma	2.3335
A0A0R4J093_MOUSE	UMP-CMP kinase	2.320654
QCR10_MOUSE	Cytochrome b-c1 complex subunit 10	2.277176
COX7C_MOUSE	Cytochrome c oxidase subunit 7C, mitochondrial	2.270833
CAND1_MOUSE	Cullin-associated NEDD8-dissociated protein 1	2.261506
Q543M7_MOUSE	Importin subunit alpha	2.232002
Q8BVQ9_MOUSE	26S protease regulatory subunit 7	2.208435
STIP1_MOUSE	Stress-induced-phosphoprotein 1	2.197041
TXD17_MOUSE	Thioredoxin domain-containing protein 17	2.165337
Q9CPX4_MOUSE	Ferritin	2.161834
F8WIA1_MOUSE	CAP-Gly domain-containing linker protein 1	2.122414
SDCG8_MOUSE	Serologically defined colon cancer antigen 8 homolog	2.121559
Q8BFQ1_MOUSE	Prosaposin	2.119551
PDIA6_MOUSE	Protein disulfide-isomerase A6	2.068221
Q499X4_MOUSE	Synaptic vesicle membrane protein VAT-1 homolog	2.05867
Q561N5_MOUSE	40S ribosomal protein S18	2.053017
ES1_MOUSE	ES1 protein homolog, mitochondrial	2.051459
Q3U6L3_MOUSE	Glutaredoxin, isoform CRA_a	2.049559
PSA6_MOUSE	Proteasome subunit alpha type-6	2.049024
NDUC2_MOUSE	NADH dehydrogenase 1 subunit C2	2.047106
H7BX64_MOUSE	Sarcolemmal membrane-associated protein	2.045809
CO6A1_MOUSE	Collagen alpha-1(VI) chain	2.038665
COMT_MOUSE	Catechol O-methyltransferase	2.035218
ANXA7_MOUSE	Annexin A7	2.034
NDUS3_MOUSE	NADH dehydrogenase iron-sulfur protein 3, mitochondrial	2.0308
Q545S0_MOUSE	Sulfurtransferase	2.007492
UGPA_MOUSE	UTP--glucose-1-phosphate uridylyltransferase	2.00286
G5E8T9_MOUSE	Hydroxyacyl glutathione hydrolase	1.99599
GTR4_MOUSE	Solute carrier family 2, facilitated glucose transporter member 4	1.990184
PDC6I_MOUSE	Programmed cell death 6-interacting protein	1.981432
ANXA5_MOUSE	Annexin A5	1.964818
MAOX_MOUSE	NADP-dependent malic enzyme	1.933061
CD47_MOUSE	Leukocyte surface antigen CD47	1.93226
Q3TV21_MOUSE	Frataxin	1.929493
ODB2_MOUSE	Lipoamide acyltransferase component of branched-chain alpha-keto acid dehydrogenase complex, mitochondrial	1.928248
VAPA_MOUSE	Vesicle-associated membrane protein-associated protein A	1.90772
PA1B2_MOUSE	Platelet-activating factor acetylhydrolase IB subunit beta	1.895529

NDUAD_MOUSE	NADH dehydrogenase 1 alpha subcomplex subunit 13	1.890973
MCAT_MOUSE	Mitochondrial carnitine/acylcarnitine carrier protein	1.889925
BACH_MOUSE	Isoform C of Cytosolic acyl coenzyme A thioester hydrolase	1.876667
Q5ND36_MOUSE	Alpha-2-antiplasmin	1.863565
F2Z456_MOUSE	NADH-cytochrome b5 reductase	1.861127
HSPB6_MOUSE	Heat shock protein beta-6	1.847715
COF1_MOUSE	Cofilin-1	1.828459
PLIN4_MOUSE	Perilipin-4	1.827155
Q5HZK3_MOUSE	Proteasome (Prosome, macropain) 28 subunit, alpha	1.816172
E9Q1W0_MOUSE	Calcium/calmodulin-dependent protein kinase type II subunit delta	1.814084
SYDC_MOUSE	Aspartate--tRNA ligase, cytoplasmic	1.807108
E9PUD2_MOUSE	Dynamin-1-like protein	1.799964
Q3TX38_MOUSE	Voltage-dependent anion-selective channel protein 3	1.778391
B3AT_MOUSE	Band 3 anion transport protein	1.77496
Q542G9_MOUSE	Annexin	1.772496
Q80Y52_MOUSE	Heat shock protein 90, alpha (Cytosolic), class A member 1	1.764213
LAMP2_MOUSE	Lysosome-associated membrane glycoprotein 2	1.761354
B7ZCF1_MOUSE	26S protease regulatory subunit 6A	1.743877
Q497I3_MOUSE	Fatty acid binding protein 5, epidermal	1.740813
Q3TPZ5_MOUSE	Dynactin 2	1.713427
OXND1_MOUSE	Oxidoreductase NAD-binding domain-containing protein 1	1.710108
TBA8_MOUSE	Tubulin alpha-8 chain	1.694346
BZW2_MOUSE	Basic leucine zipper and W2 domain-containing protein 2	1.690544
VWA8_MOUSE	von Willebrand factor A domain-containing protein 8	1.690259
NDRG2_MOUSE	Protein NDRG2	1.671721
Q544D4_MOUSE	Delta-sarcoglycan	1.671108
GSTO1_MOUSE	Glutathione S-transferase omega-1	1.670085
BAG3_MOUSE	BAG family molecular chaperone regulator 3	1.664661
E9Q3X0_MOUSE	Major vault protein	1.661372
PSMD6_MOUSE	26S proteasome non-ATPase regulatory subunit 6	1.649079
Q7JCZ1_MOUSE	Cytochrome c oxidase subunit 2	1.648254
NDUB2_MOUSE	NADH dehydrogenase 1 beta subcomplex subunit 2, mitochondrial	1.645909
Q8CBB6_MOUSE	Histone H2B	1.645206
NDUA6_MOUSE	NADH dehydrogenase 1 alpha subcomplex subunit 6	1.643343
Q4FJU3_MOUSE	Crip2 protein	1.642117
CATB_MOUSE	Cathepsin B	1.640215
ETHE1_MOUSE	Persulfide dioxygenase ETHE1, mitochondrial	1.634732
B0QZL1_MOUSE	Alpha-enolase	1.633795
Q6GT24_MOUSE	Peroxiredoxin 6	1.626017
TIM13_MOUSE	Mitochondrial import inner membrane translocase subunit Tim13	1.615049
Q3T9Z2_MOUSE	Glyoxylate reductase/hydroxypyruvate reductase	1.610213
G5E8R3_MOUSE	Pyruvate carboxylase	1.597556
NDUS2_MOUSE	NADH dehydrogenase iron-sulfur protein 2, mitochondrial	1.596723
D3Z636_MOUSE	Inorganic pyrophosphatase 2, mitochondrial	1.59351

KAD1_MOUSE	Adenylate kinase isoenzyme 1	1.593473
ATAD3_MOUSE	ATPase family AAA domain-containing protein 3	1.586299
NDUV2_MOUSE	NADH dehydrogenase flavoprotein 2, mitochondrial	1.569232
GDIR1_MOUSE	Rho GDP-dissociation inhibitor 1	1.563698
Q9MD82_MOUSE	NADH-ubiquinone oxidoreductase chain 5	1.562489
A2RTT4_MOUSE	MCG4297	1.558157
ENOB_MOUSE	Beta-enolase	1.554284
Q3TS44_MOUSE	Proteasome subunit alpha type	1.552829
G3X9J1_MOUSE	Sodium/calcium exchanger 1	1.550129
ARPC2_MOUSE	Actin-related protein 2/3 complex subunit 2	1.542713
GRPE1_MOUSE	GrpE protein homolog 1, mitochondrial	1.538649
Q91V77_MOUSE	Protein S100	1.537994
F6WYM0_MOUSE	Septin-2	1.530294
HSPB1_MOUSE	Heat shock protein beta-1	1.52291
TLN1_MOUSE	Talin-1	1.52168
Q545X8_MOUSE	40S ribosomal protein S4	1.519066
A0A087WS46_MOUSE	Elongation factor 1-beta	1.514587
B9EHN0_MOUSE	Ubiquitin-activating enzyme E1, Chr X	1.514322
A0A0G2JFH2_MOUSE	Microtubule-associated protein	1.510462
Q9DCY1_MOUSE	Peptidyl-prolyl cis-trans isomerase	1.504742

Table 3.6

Group C: Down-regulated Proteins KO-TAC vs KO-SHAM		
Uniprot accession	**Protein**	**Fold Change**
NDUA3_MOUSE	NADH dehydrogenase 1 alpha subcomplex subunit 3	7.130738
DHSD_MOUSE	Succinate dehydrogenase cytochrome b small subunit, mitochondrial	5.199991
A1BG_MOUSE	Alpha-1B-glycoprotein	4.615402
CXA1_MOUSE	Gap junction alpha-1 protein	4.604655
NDUB3_MOUSE	NADH dehydrogenase 1 beta subcomplex subunit 3	2.99022
68MP_MOUSE	6.8 kDa mitochondrial proteolipid	2.836409
Q8BTU6_MOUSE	Eukaryotic initiation factor 4A-II	2.696546
G5E8J6_MOUSE	Histidine rich calcium binding protein, isoform CRA_a	2.535813
Q58E35_MOUSE	60S acidic ribosomal protein P1	2.5039
RL8_MOUSE	60S ribosomal protein L8	2.355288
A1AT4_MOUSE	Alpha-1-antitrypsin 1-4	2.341611
FRIH_MOUSE	Ferritin heavy chain	2.261752
ILK_MOUSE	Integrin-linked protein kinase	2.200704
Q6P5I3_MOUSE	S-(hydroxymethyl)glutathione dehydrogenase	2.184623
RLA2_MOUSE	60S acidic ribosomal protein P2	2.169577
NDUB4_MOUSE	NADH dehydrogenase 1 beta subcomplex subunit 4	2.161729
2AAA_MOUSE	Serine/threonine-protein phosphatase 2A 65 kDa regulatory subunit A alpha isoform	2.154025

Q497X4_MOUSE	Cathepsin R	2.131074
Q3U367_MOUSE	4-trimethylaminobutyraldehyde dehydrogenase	2.036147
Q3UX28_MOUSE	Brain protein 44-like	2.023577
K22O_MOUSE	Keratin, type II cytoskeletal 2 oral	1.984574
Q91VA7_MOUSE	Isocitrate dehydrogenase [NAD] subunit, mitochondrial	1.982698
Q544X6_MOUSE	Ferrochelatase	1.94918
E9QMK9_MOUSE	Protein 9030617O03Rik	1.948365
MTX2_MOUSE	Metaxin-2	1.925818
E9Q7L0_MOUSE	Protein Ogdhl	1.919471
KV3A4_MOUSE	Ig kappa chain V-III region 50S10.1	1.917761
TRAP1_MOUSE	Heat shock protein 75 kDa, mitochondrial	1.910707
RL14_MOUSE	60S ribosomal protein L14	1.89362
APOH_MOUSE	Beta-2-glycoprotein 1	1.887297
B1AU25_MOUSE	Apoptosis-inducing factor 1, mitochondrial	1.839261
Q921R2_MOUSE	40S ribosomal protein S13	1.827666
ARF5_MOUSE	ADP-ribosylation factor 5	1.821445
MYL6_MOUSE	Myosin light polypeptide 6	1.812493
CES1D_MOUSE	Carboxylesterase 1D	1.801977
Q497F1_MOUSE	Troponin I, cardiac 3	1.796747
ABCB8_MOUSE	ATP-binding cassette sub-family B member 8, mitochondrial	1.787346
PPIF_MOUSE	Peptidyl-prolyl cis-trans isomerase F, mitochondrial	1.75551
LDHB_MOUSE	L-lactate dehydrogenase B chain	1.730964
DYL2_MOUSE	Dynein light chain 2, cytoplasmic	1.729737
IVD_MOUSE	Isovaleryl-CoA dehydrogenase, mitochondrial	1.698572
Q58EV5_MOUSE	High mobility group box 1	1.66142
ADCK3_MOUSE	Atypical kinase ADCK3, mitochondrial	1.616159
Q3TGZ3_MOUSE	Isocitrate dehydrogenase [NAD] subunit, mitochondrial	1.608976
CAD13_MOUSE	Cadherin-13	1.603548
Q6ZWZ6_MOUSE	40S ribosomal protein S12	1.601422
B2RS41_MOUSE	Aldhehyde dehydrogenase family 5, subfamily A1	1.598923
RM12_MOUSE	39S ribosomal protein L12, mitochondrial	1.596099
PLIN5_MOUSE	Perilipin-5	1.58571
RTN3_MOUSE	Reticulon-3	1.555692
SDHA_MOUSE	Succinate dehydrogenase flavoprotein subunit, mitochondrial	1.534129
TPM1_MOUSE	Tropomyosin alpha-1 chain	1.52837

Table 3.7

Group D: Up-regulated Proteins in KO-TAC vs WT-TAC		
Uniprot Accession	**Protein**	**Fold Change**
Q542X7_MOUSE	Chaperonin subunit 2 (Beta), isoform CRA_a	4.011262
QCR10_MOUSE	Cytochrome b-c1 complex subunit 10	2.610662
G3X9J1_MOUSE	Sodium/calcium exchanger 1	2.551344

PSMD6_MOUSE	26S proteasome non-ATPase regulatory subunit 6	2.527684
NDUF4_MOUSE	NADH dehydrogenase 1 alpha subcomplex assembly factor 4	2.488534
Q91XH5_MOUSE	Sepiapterin reductase	2.382154
Q9CPX4_MOUSE	Ferritin	2.220084
NDUC2_MOUSE	NADH dehydrogenase 1 subunit C2	2.129968
GTR4_MOUSE	glucose transporter member 4	2.048086
NDUA6_MOUSE	NADH dehydrogenase 1 alpha subcomplex subunit 6	2.046164
Q5M9J2_MOUSE	Histidine triad nucleotide binding protein 2	2.004136
CD47_MOUSE	Leukocyte surface antigen CD47	1.993659
Q8BH80_MOUSE	Vesicle-associated membrane protein, associated protein B and C	1.94817
A3KGQ6_MOUSE	Actin-related protein 2/3 complex subunit 5	1.892679
QCR8_MOUSE	Cytochrome b-c1 complex subunit 8	1.850327
NDUV2_MOUSE	NADH dehydrogenase flavoprotein 2, mitochondrial	1.801866
NDUS3_MOUSE	NADH dehydrogenase iron-sulfur protein 3, mitochondrial	1.794648
Q80ZZ0_MOUSE	EH domain-containing protein 1	1.786371
TM14C_MOUSE	Transmembrane protein 14C	1.77977
Q5SW88_MOUSE	Protein Rab1a	1.767473
CATB_MOUSE	Cathepsin B	1.757032
NDUAD_MOUSE	NADH dehydrogenase 1 alpha subcomplex subunit 13	1.752319
THIM_MOUSE	3-ketoacyl-CoA thiolase, mitochondrial	1.74534
Q7JCZ1_MOUSE	Cytochrome c oxidase subunit 2	1.739015
Q4FK74_MOUSE	ATP synthase subunit delta, mitochondrial	1.726552
OXND1_MOUSE	Oxidoreductase NAD-binding domain-containing protein 1	1.715566
Z4YK42_MOUSE	NAD kinase 2, mitochondrial	1.703483
Q5NCJ9_MOUSE	Cytochrome b-c1 complex subunit 9	1.680291
CY1_MOUSE	Cytochrome c1, heme protein, mitochondrial	1.673262
B2RTM0_MOUSE	Histone H4	1.663071
Q792A4_MOUSE	Cox7ah	1.659221
CPT2_MOUSE	Carnitine O-palmitoyltransferase 2, mitochondrial	1.658698
Q8C5G6_MOUSE	Toll-interacting protein	1.640463
A0A0R3P9C8_MOUSE	NADH dehydrogenase 1 alpha subcomplex subunit 9, mitochondr	1.637799
VWA8_MOUSE	von Willebrand factor A domain-containing protein 8	1.63688
Q4FJU3_MOUSE	Crip2 protein	1.623828
TACO1_MOUSE	Translational activator of cytochrome c oxidase 1	1.604731
HHATL_MOUSE	Protein-cysteine N-palmitoyltransferase HHAT-like protein	1.593732
HCDH_MOUSE	Hydroxyacyl-coenzyme A dehydrogenase, mitochondrial	1.580108
F6TCV0_MOUSE	Serine protease HTRA2, mitochondrial	1.580029
Q9MD82_MOUSE	NADH-ubiquinone oxidoreductase chain 5	1.575971
RTN2_MOUSE	Isoform 2 of Reticulon-2	1.57565
Q3UAI3_MOUSE	CD36 antigen, isoform CRA_a	1.563316
NDUS7_MOUSE	NADH dehydrogenase iron-sulfur protein 7, mitochondrial	1.562736

Table 3.8

| Group D: Down-regulated Proteins in KO-TAC vs WT-TAC		
Uniprot Accession	**Protein**	**Fold Change**
TBB5_MOUSE	Tubulin beta-5 chain	2.981927
DHSD_MOUSE	Succinate dehydrogenase cytochrome b small subunit, mitochondrial	2.481798
F6ZFU0_MOUSE	Elongation factor 1-delta	2.425279
Q8BFQ1_MOUSE	Prosaposin	2.378969
CAH2_MOUSE	Carbonic anhydrase 2	2.376344
GCAM_MOUSE	Ig gamma-2A chain C region, membrane-bound form	2.374465
APOH_MOUSE	Beta-2-glycoprotein 1	2.372747
NDUA3_MOUSE	NADH dehydrogenase 1 alpha subcomplex subunit 3	2.266877
68MP_MOUSE	6.8 kDa mitochondrial proteolipid	2.150122
CAH1_MOUSE	Carbonic anhydrase 1	2.136464
RL8_MOUSE	60S ribosomal protein L8	2.089221
Q52L67_MOUSE	Gpsn2 protein	2.083124
Q544X6_MOUSE	Ferrochelatase	2.051581
B2RXX9_MOUSE	Myosin, heavy polypeptide 7, cardiac muscle, beta	2.026056
ARF5_MOUSE	ADP-ribosylation factor 5	1.889291
E9QLZ9_MOUSE	Protein enabled homolog	1.845804
Q545I9_MOUSE	Protein S100	1.809239
Q921R2_MOUSE	40S ribosomal protein S13	1.805659
MTX2_MOUSE	Metaxin-2	1.787365
A2AEX8_MOUSE	Four and a half LIM domains 1, isoform CRA_b	1.778477
K22O_MOUSE	Keratin, type II cytoskeletal 2 oral	1.770453
Q6P5I3_MOUSE	S-(hydroxymethyl)glutathione dehydrogenase	1.725549
Q91VB8_MOUSE	Alpha globin 1	1.700586
E9Q616_MOUSE	Protein Ahnak	1.698923
TPM1_MOUSE	Tropomyosin alpha-1 chain	1.659611
B2MWM9_MOUSE	Calreticulin	1.6296
2AAA_MOUSE	Serine/threonine-protein phosphatase 2A 65 kDa regulatory subunit A alpha isoform	1.591433
Q497F1_MOUSE	Troponin I, cardiac 3	1.588601
PLAK_MOUSE	Junction plakoglobin	1.587987
Q543J5_MOUSE	Antithrombin	1.53439
CO3_MOUSE	Complement C3	1.530253
MLRV_MOUSE	Myosin regulatory light chain 2, ventricular/cardiac muscle isoform	1.528094
DYL2_MOUSE	Dynein light chain 2, cytoplasmic	1.52776
TMOD1_MOUSE	Tropomodulin-1	1.517943
Q549A5_MOUSE	Clusterin	1.516287
Q564F3_MOUSE	40S ribosomal protein S3a	1.494773
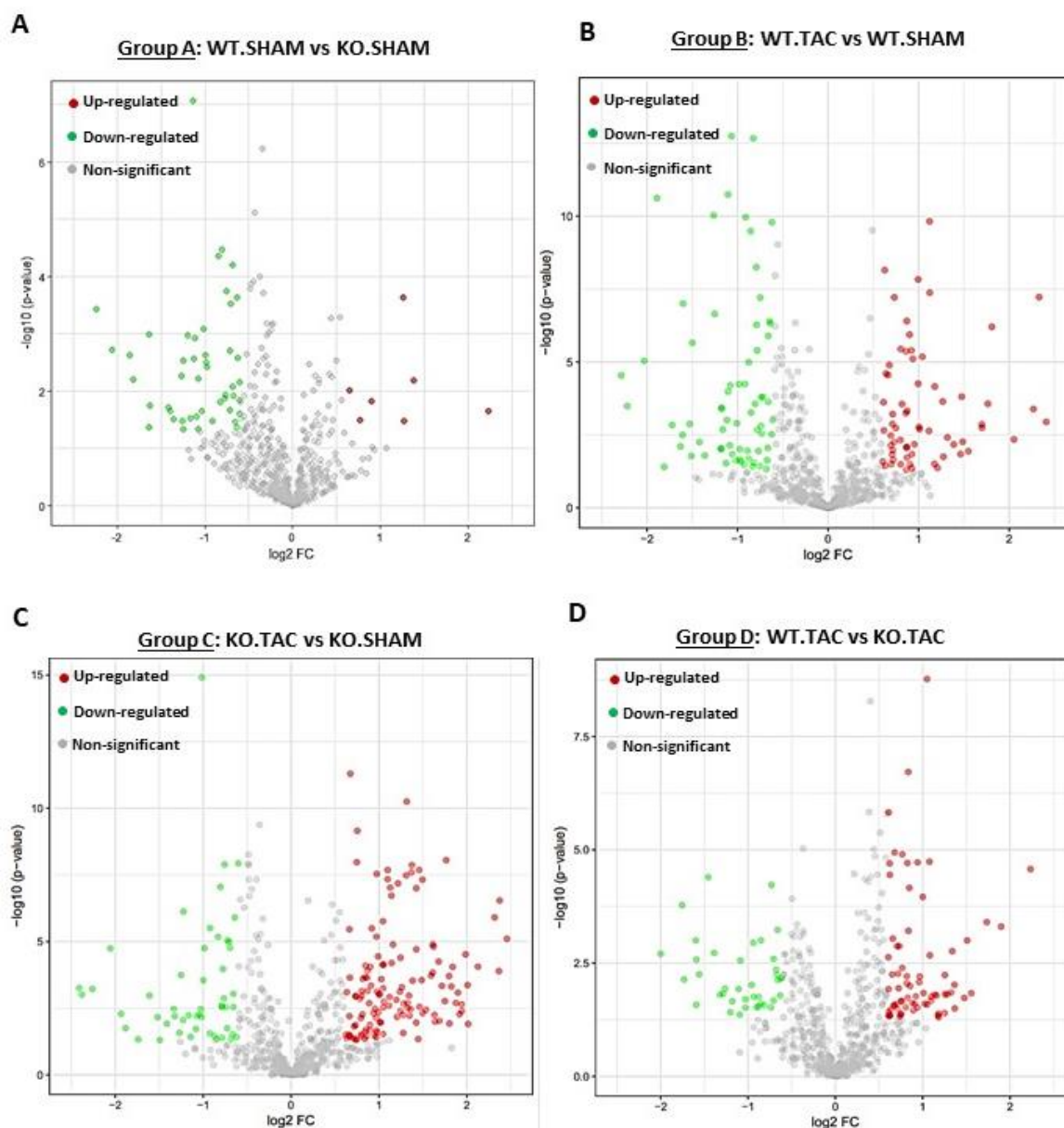
Fig. 3.17. Distribution of identified proteins in global proteome analysis: A-D Volcano plots illustrating the proteomic data log2 fold-change (log2 FC) on X axis and statistical significance distribution log10 of p values (-log10 (p-value)) on Y-axis of the proteomic data. Data points in red and green indicate proteins defined to be significantly differentially expressed based upon 1.5-fold change and p value of 0.005. Proteins in red denote those that reached statistical significance using Welch's T-test and are up-regulated while Proteins in green shows significant down-regulation.

3.6.2 Functional characterization of proteome data using STRING analysis

For detailed characterization of proteome, we used STRING analysis to categorize differentially expressed proteins according to their subcellular localization as assigned by Gene ontology (GO) annotations for better understanding of protein functions.

3.6.2.1 Characterization of Group A (WT-SHAM vs KO-SHAM) proteome

Previously, we observed in PCA plot (Fig. 3.15) that WT-SHAM and KO-SHAM are closely clustered to each other showing less variability. Perseus analysis showed there were only 8 up-regulated proteins in KO-SHAM as compared to WT-SHAM while there were 58 down-regulated proteins. We analysed these up and down- regulated proteins using STRING analysis. We observed 5 proteins belonging to (cytosol, 63%) while 3 proteins belong to mitochondria (37%) in KO-SHAM (Fig. 3.18A). Up-regulated proteins are showing a small cluster of mitochondrial proteins based on their function and localisation while cytoplasmic proteins are not showing any significant link (Fig. 3.18B). Similarly, we observed out of 58 down-regulated proteins in KO-SHAM, 73% proteins belonging to cytoplasm, 17% proteins to cytoskeleton while 10% to ribosome in (Fig. 3.18C). The STRING analysis revealed a functional link between down-regulated proteins in KO-SHAM based on their function and localisation one cluster of proteins belong to ribosomal proteins (Fig. 3.18D). Some other proteins are also linked but they do not form a major interconnecting cluster.
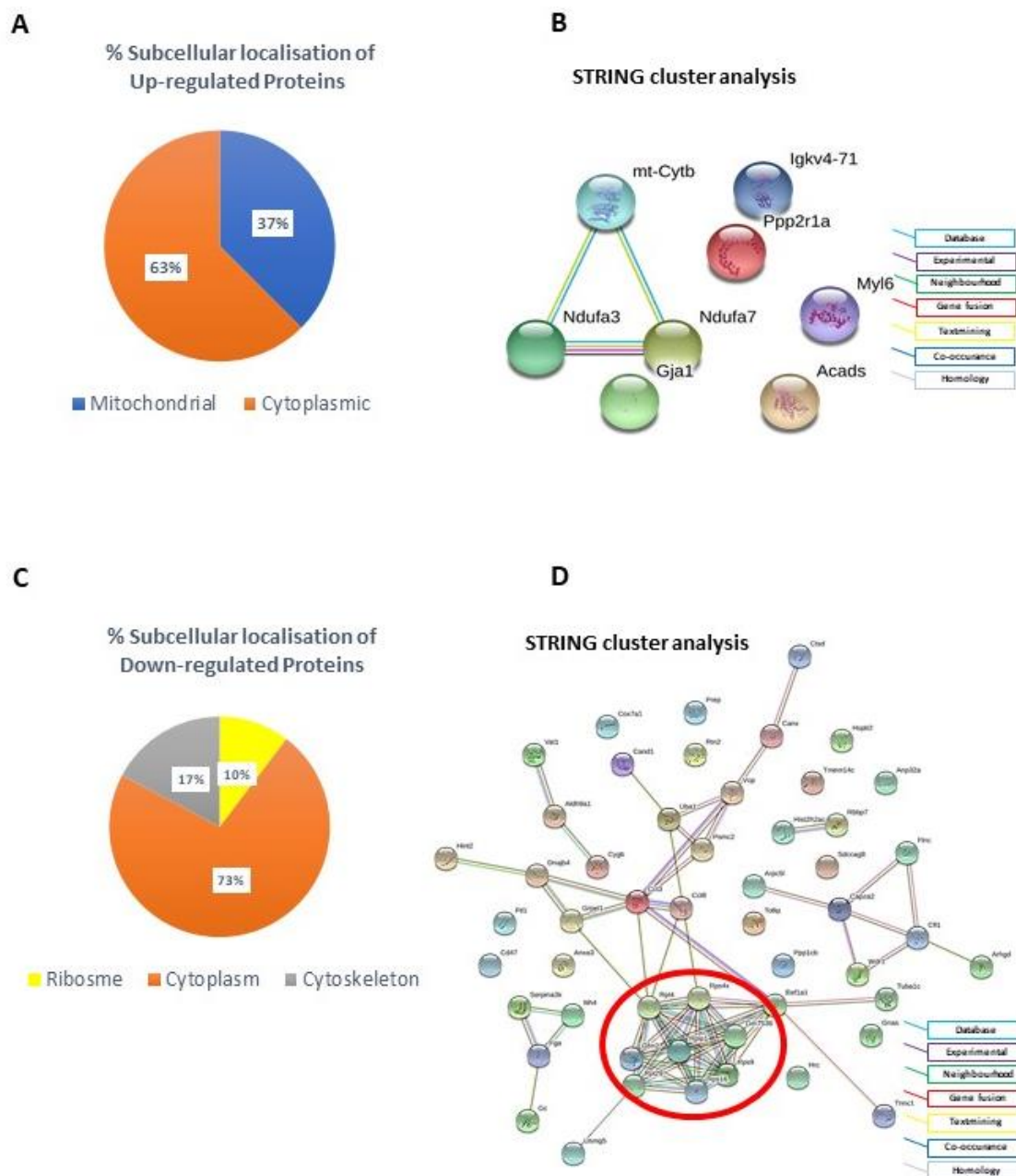
Fig. 3.18. Characterization for Group A, WT-SHAM vs KO-SHAM proteome. Pie chart shows proteins according to their subcellular location assigned by STRING and Gene-ontology (GO). Percentage of up-regulated proteins (**A**) and down-regulated proteins (**C**), Orange colour shows localised in cytoplasm, blue colour represents proteins localised in mitochondria, yellow colour represents ribosomal proteins and grey colour represents cytoskeleton proteins. Analysis of protein interaction network by STRING (B & D), Coloured lines between the proteins indicate the protein co-occurrence, co-expression, known interactions and predicted interactions. Up-regulated proteins do not present any specific interaction or cluster (**B**) however Interconnecting ribosomal proteins (red circle) represents a functionally associated protein cluster in down-regulated proteins (**D**). B and D full view available as Supplementary Fig. S1.

3.6.2.2 Characterization of Group B (WT-SHAM vs WT-TAC) proteome

Next, we analysed group B: WT-SHAM comparison with WT-TAC. Previously, we observed in PCA plot (Fig. 3.15) that WT-SHAM and WT -TAC are showing clusters variability which would be interesting to analyse. Perseus analysis showed there were 60 up-regulated and 70 down-regulated proteins in WT-TAC as compared to WT-SHAM.
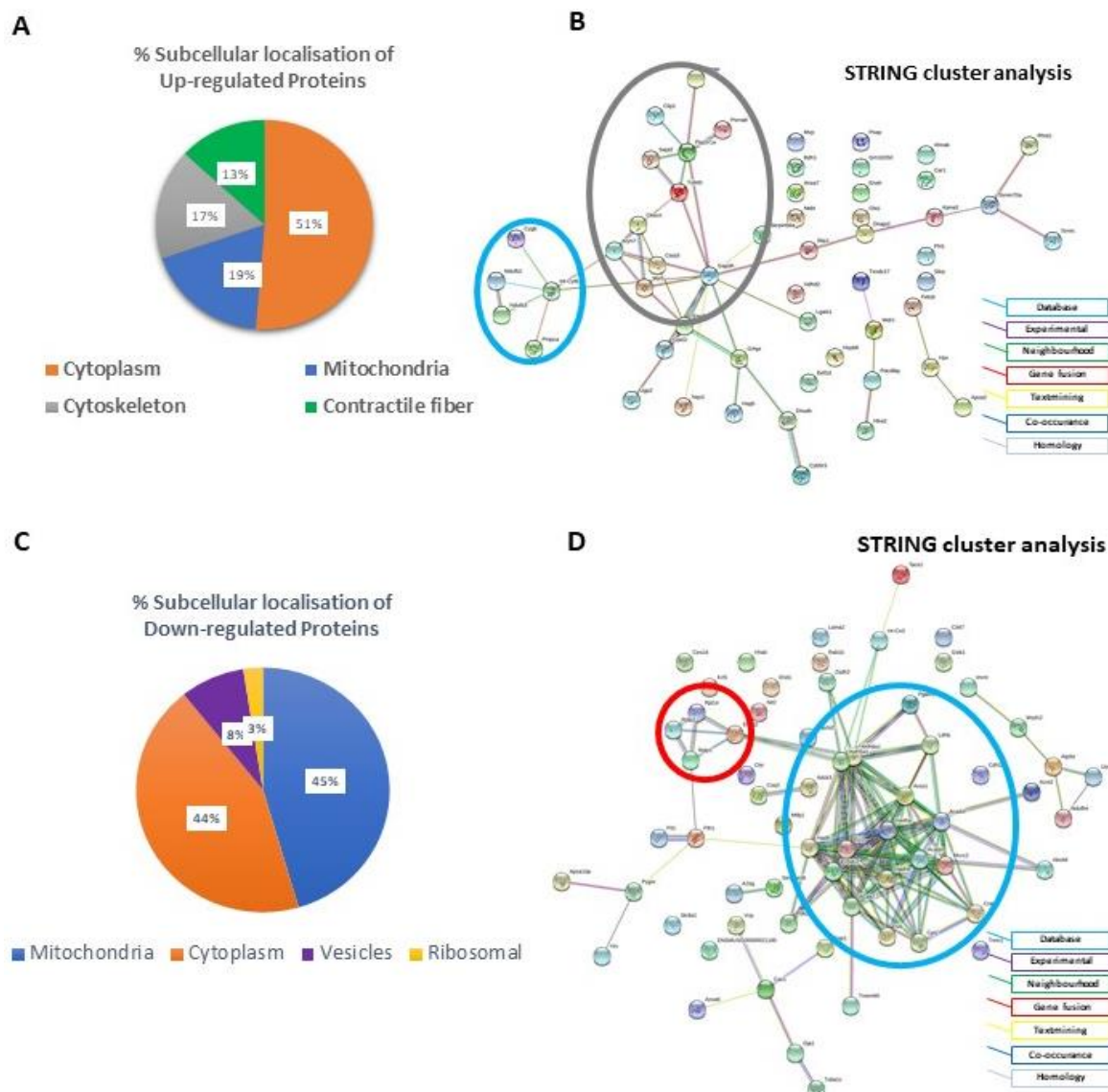

Fig. 3.19. Characterization for Group B, WT-SHAM vs WT-TAC proteome. Pie chart shows proteins according to their subcellular location assigned by STRING and Gene-ontology (GO). %age of up-regulated proteins (**A**) and down-regulated proteins (**C**), Orange colour shows proteins localised in cytoplasm, blue colour represents the mitochondrial, green colour represents contractile fibre associated proteins, grey colour represents cytoskeleton proteins, purple colour represents vesicle associated proteins and yellow colour represents ribosomal associated proteins. Analysis of protein interaction network by STRING (B & D), Coloured lines between the proteins indicate the protein co-occurrence, co-expression, known interactions and predicted interactions. Up-regulated proteins show interconnecting mitochondrial proteins (blue circle) represents a functionally associated protein cluster, while cytoskeleton associated proteins are showing another cluster (grey circle) in up-regulated proteins (**B**). Interconnecting mitochondrial proteins (blue circle)

represents a functionally associated protein cluster, while ribosomal associated proteins are showing another cluster (red circle) in down-regulated proteins (**D**). B and D full view available as Supplementary Fig. S2 and S3 respectively.

We further analysed these up and down- regulated proteins using STRING analysis. We observed out of 60 up-regulated proteins in WT-TAC, 51% proteins belonging to cytoplasm, 19% to mitochondrial, 17% proteins to cytoskeleton while 13% to contractile fibre proteins (Fig. 3.19A). The STRING analysis revealed functional link between up-regulated proteins in WT-TAC, based on their function and localisation. One cluster of proteins (blue circle) belong to mitochondrial proteins while second cluster (grey circle) represents cytoskeleton associated proteins (Fig. 3.19B). Some other proteins are also linked but they do not form a major interconnecting cluster. Most of them are multiple enzymes either involved in translocation of molecules or associated with different metabolic pathways. Similarly, we observed out of 70 down-regulated proteins in WT-TAC, 44% proteins belonging to cytoplasm, 45% proteins to mitochondria, 8% to vesicles while 3% to ribosome in (Fig. 3.19C). Interestingly, majority of down-regulated proteins are linked to mitochondria in WT-TAC. The STRING analysis revealed functional link between down-regulated proteins in WT-TAC, based on their function and localisation. One major cluster of proteins (blue circle) belong to mitochondrial proteins while second cluster (red circle) represents Ribosomal associated proteins (Fig. 3.19D). Some other proteins are also linked but they do not form a major interconnecting cluster. Most of them are multiple enzymes which are associated with different metabolic pathways.

3.6.2.3 Characterization of Group C (KO-SHAM vs KO-TAC) proteome

Next, we analysed group C, KO-SHAM comparison with KO-TAC. Previously, we observed in PCA plot (Fig. 3.15) that KO-SHAM and KO -TAC are showing clusters variability which would be interesting to analyse. Perseus analysis showed there were 150 up-regulated and 53 down-regulated proteins in KO-TAC as compared to KO-SHAM. We further analysed these up and down-regulated proteins using STRING analysis. We observed out of 150 up-regulated proteins in KO-TAC, 40% proteins belonging to cytoplasm, 28% to vesicles, 17% to mitochondrial, 13% proteins to cytoskeleton while 2% to proteasome associated proteins (Fig. 3.20A). The STRING analysis revealed functional link between up-regulated proteins in KO-TAC, based on their function and localisation. One cluster of

proteins (blue circle) belong to mitochondrial proteins while second cluster (green circle) represents proteasome-
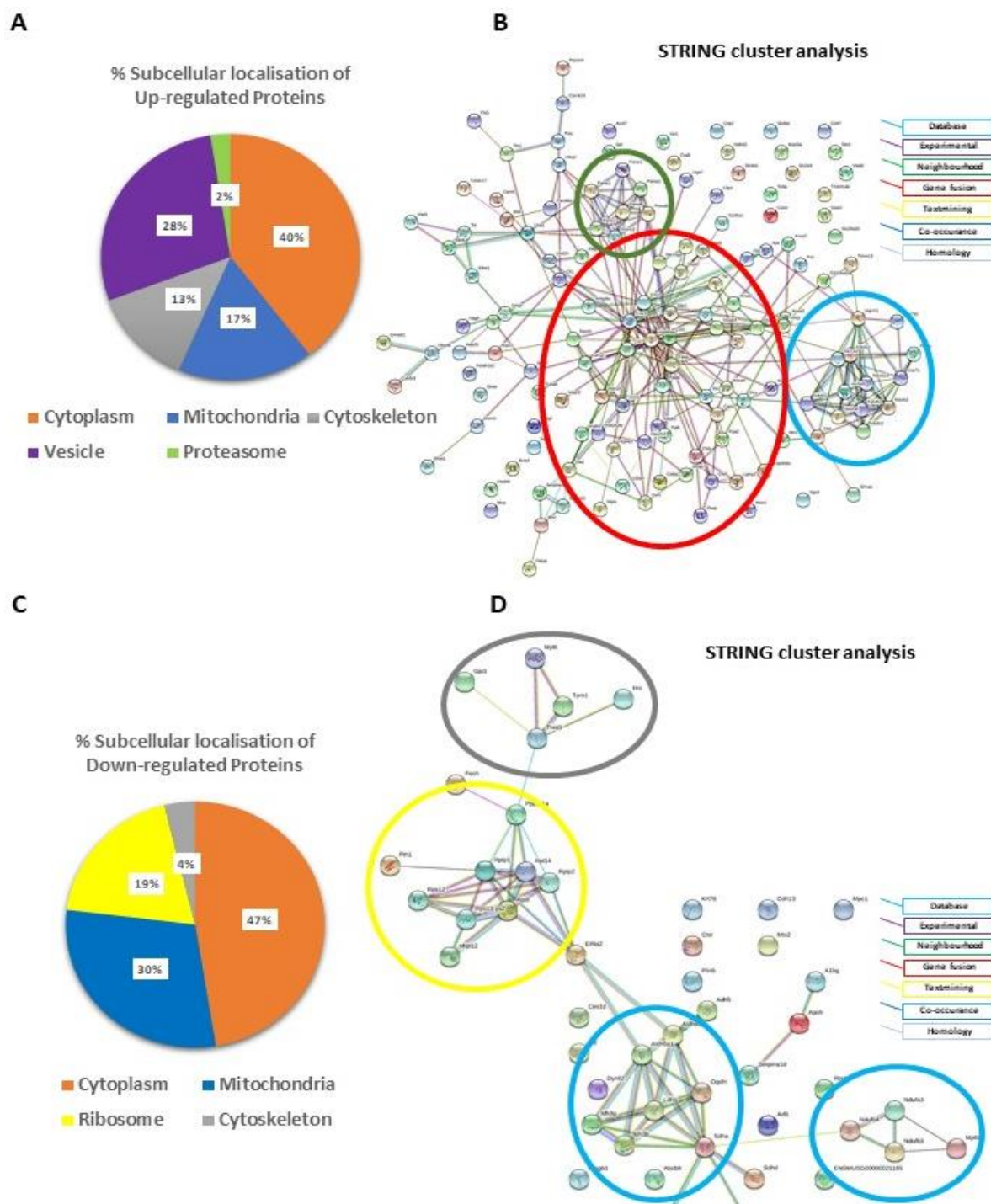

Fig. 3.20. Characterization for Group C, KO-SHAM vs KO-TAC proteome. Pie chart shows proteins according to their subcellular location assigned by STRING and Gene-ontology (GO). % of up-regulated proteins (**A**) and down-regulated proteins (**C**), Orange colour shows proteins localised in cytoplasm, blue colour represents the mitochondrial, green colour represents contractile fibre associated proteins, grey colour represents cytoskeleton proteins, purple colour represents vesicle associated proteins, Light-green colour represents proteasome associated proteins and yellow colour represents ribosomal associated proteins. Analysis of protein interaction network by STRING (B& D), Coloured lines between the proteins indicate the protein co-occurrence, co-expression, known interactions and predicted interactions. Up-regulated proteins show interconnecting major cluster (red circle) represents multiple enzymes involved in metabolic pathways and cytoskeleton associated proteins while, mitochondrial proteins (blue circle) represents a functionally associated protein

72

cluster, while proteasome associated proteins are showing another cluster (green circle) (**B**). Interconnecting major clusters show mitochondrial proteins (blue circle), ribosomal proteins (yellow circle) and cytoskeleton proteins (grey circle) in down-regulated proteins (**D**). B and D full view available as Supplementary Fig. S4 and S5 respectively.

-associated proteins (Fig. 3.20B), Interestingly third major cluster have proteins which are mainly enzymes either involved in translocation of molecules or associated with different metabolic pathways and some cytoskeleton associated proteins. In down-regulated proteins we observed out of 53 proteins in KO-TAC, 47% proteins belonging to cytoplasm, 30% proteins to mitochondria, 19 % to ribosome while 8% to cytoskeleton (Fig. 3.20C). The STRING analysis revealed functional link between down-regulated proteins in KO-TAC, based on their function and localisation. Two clusters of proteins (blue circle) belong to mitochondrial proteins, one cluster (yellow circle) associated with ribosomal proteins while one small cluster (grey circle) represents cytoskeleton associated proteins (Fig. 3.20D).

3.6.2.4 Characterization of Group D (WT-TAC vs KO-TAC) proteome

Next, we analysed group D, WT-TAC comparison with KO-TAC. Previously, we observed in PCA plot (Fig. 3.15) that WT-TAC and KO -TAC are showing clusters variability which would be interesting to analyse. Perseus analysis showed there were 43 up-regulated and 36 down-regulated proteins in KO-TAC as compared to WT-TAC. We further analysed these up and down- regulated proteins using STRING analysis. We observed out of 43 up-regulated proteins in KO-TAC, 47% proteins belonging to cytoplasm, 33% to mitochondrial, while 20% to vesicles associated proteins (Fig. 3.21A). The STRING analysis revealed functional link between up-regulated proteins in KO-TAC, based on their function and localisation. One major cluster of proteins (blue circle) belong to mitochondrial proteins (Fig. 3.21B). We observed out of 36 down-regulated proteins in KO-TAC, 39% proteins belonging to cytoplasm, 22% to vesicle associated, 21% to cytoskeleton, 10% proteins to mitochondria and 8 % to ribosome (Fig. 3.21C). The STRING analysis revealed functional link between down-regulated proteins in KO-TAC, based on their function and localisation. One cluster (yellow circle) associated with ribosomal proteins while one small cluster (grey circle) represents cytoskeleton associated proteins (Fig. 3.21D).
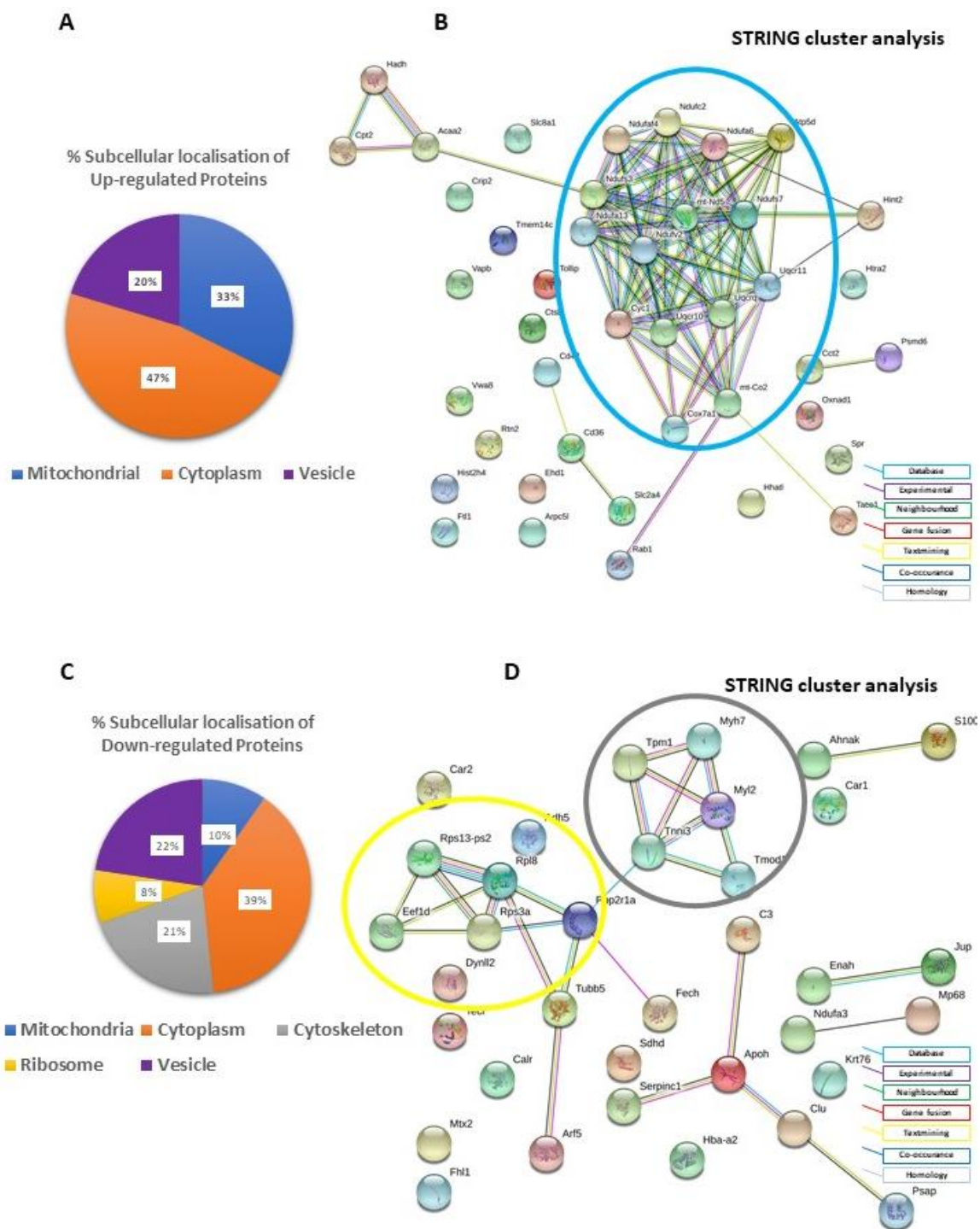
Fig. 3.21. Characterization for Group D, WT-TAC vs KO-TAC proteome. Pie chart shows proteins according to their subcellular location assigned by STRING and Gene-ontology (GO). % of up-regulated proteins (**A**) and down-regulated proteins (**C**), Orange colour shows proteins localised in cytoplasm, blue colour represents the mitochondrial, green colour represents contractile fibre associated proteins, grey colour represents cytoskeleton proteins, purple colour represents vesicle associated proteins, and yellow colour represents ribosomal associated proteins. Analysis of protein interaction network by STRING, Coloured lines between the proteins indicate the protein co-occurrence, co-expression, known interactions and predicted interactions. Up-regulated proteins show Interconnecting major cluster shows mitochondrial proteins (blue circle) (**B**). Interconnecting major clusters show ribosomal proteins (yellow circle) and cytoskeleton proteins (grey circle) (**D**). B and D full view available as Supplementary Fig. S6 and S7 respectively.

Interestingly in our data, group D (WT-TAC/KO-TAC) up-regulated proteins were associated with mitochondrial function in functional annotation and in cluster analysis (Fig. 3.19B). We further investigated the proteins which were associated with mitochondria and found out NADH dehydrogenase complex (Complex I of ETC) proteins were dominating the cluster (Fig. 3.19B). It is interesting to note that mitochondrial Complex I deficiency in the mouse heart results in severe hypertrophic cardiomyopathy due to selective loss of Ndufs4 (Chouchani *et al.,* 2014). We found 9 out of 45 subunits of Complex I to be up-regulated in KO-TAC mice.

3.6.3 Ingenuity Pathway Analysis (IPA) for significantly differentiated proteins in Group C and D

Then we concentrated more on KO-TAC vs KO-SHAM (Group C) and KO-TAC vs. WT-TAC (Group D) groups to identify signalling pathways that are differentially regulated in KO-TAC hearts and might have been responsible for observed cardiac hypertrophy rescue.

For this reason, we employed IPA tool, which confirmed that the identified proteins of KO-TAC mice hearts are majorly associated with mitochondrial dysfunction (p-value $9.72e^{-13}$), Oxidative phosphorylation (p-value $6.44e^{-13}$), and Sirtuin signalling pathway (p-value $1.47e^{-06}$) (Fig. 3.22A-B). Both STRING and IPA analyses highlighted increased number of proteins belongings to mitochondrial activity and oxidative phosphorylation in KO-TAC mice hearts. These analyses suggest that restored mitochondrial function might be a contributing factor in improved cardiac function. In order to verify this hypothesis, we made use of our *in-vitro* model of inflammation and investigated the effect of PTP1b inhibition on mitochondrial activity.
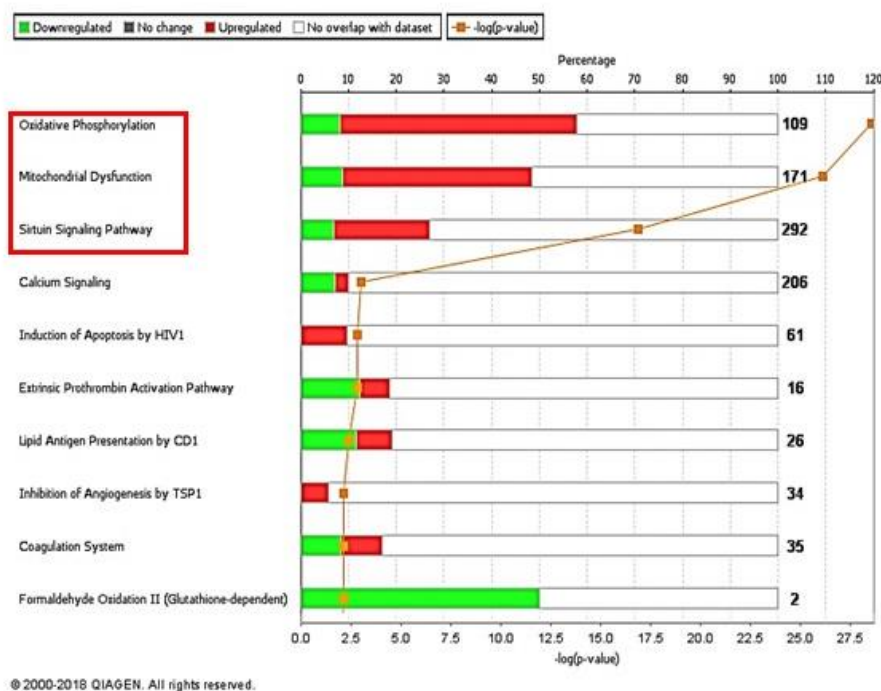
A

B

Fig. 3.22. Ingenuity pathway analysis (IPA) of KO-TAC vs WT-TAC proteins: A. Top Canonical Pathways displays the most significant Pathways across the entire dataset. The significance values of the canonical pathways were calculated by Fisher's exact test right-tailed. **B.** Stacked Bar chart plotted between -log of p-values (orange) and percentage are displaying the number of up-regulated (red), down-regulated (green) proteins, and orange square represents the -log of p-values of proteins from data set, in each Canonical Pathway.

3.6.4 PTP1b Inhibition in HUVECs

To inhibit the function of PTP1B in HUVECs we decided to use Claramine Sulphate, a known and commercially available inhibitor of PTP1B. To establish the concentration of Claramine required for efficient inhibition of PTP1B function, we treated HUVECs with different concentrations of Claramine (10, 50 and 100 µM) in four groups 1. **Control** - non-treated cells, 2. **TNF-α-only -** cells were treated with 20ng/ml TNF-α for 2 hrs, 3. **Claramine-only -** cells were treated with either 10, 50 or 100 µM Claramine for 30 min and

4. **Claramine+TNF-α -** cells were treated with either 10, 50 or 100 μM Claramine for 30 mins followed by TNF-α treatment for 2 hrs. Cells were harvested after treatment and analysed for the expression levels of p-AKT, which is a target of PTP1B to confirm the inhibition of PTP1B function. TNF-α treated cells showed reduced expression of p-AKT, while 100 μM of Claramine-only showed significantly higher expression of p-AKT as compared to control cells (Fig. 3.23). When cells are treated with Claramine followed by TNF-α, there is no difference in expression of p-AKT as compared to non-treated control. This data indicates that PTP1B inhibition leads to increased phosphorylation in of AKT, however, TNF-α treatment reverses this phosphorylation to basal level. After successfully establishing the PTP1B inhibition model in HUVECs, we went on to study the role of PTP1B in restoring mitochondrial function.
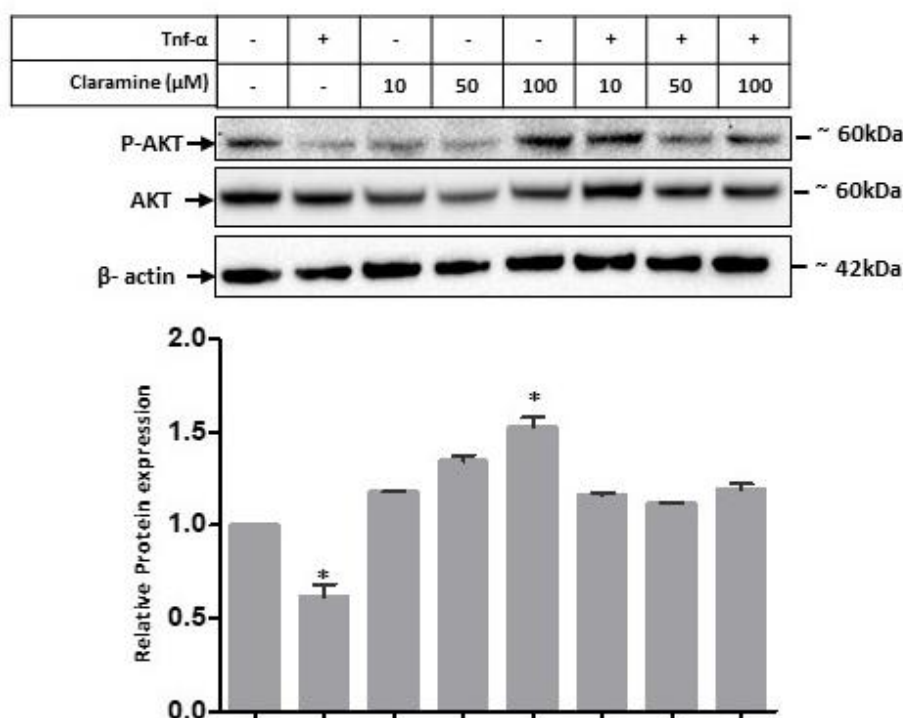

Fig. 3.23. PTP1B inhibition in HUVECs. Western Blot shows relative Protein expression of p-AKT normalised to house-keeping β-actin then to AKT in Control, TNF-α-only, Claramine-only (10, 50, 100 μM) , Claramine (10, 50, 100 μM)+TNF-α. Values are mean ± SEM of two biological replicates and asterisk indicate statistical significance of * $p < 0.05$ compared to control group.

3.6.5 Mitochondrial function assay

To study the role of PTP1B in mitochondrial function, we treated HUVECs in five different groups 1. **Control** non-treated cells, 2. **Claramine-only -** cells treated with Claramine for 30 min, 3: **TNF-α-only -** cells treated with 1500 units/ml of TNF-α for 6 hrs to induce mitochondrial dysfunction, 4: **Claramine+TNF-α –** in which cells were pre-treated with Claramine for 30 min followed by TNF-α for 6 hrs and 5: **Mitochondrial toxin -** cells treated with Sodium Azide 100 µM as a positive control of mitochondrial toxicity. Thereafter, Cytotoxicity and ATP production was measured by using Mitochondrial ToxGlo™ Assay kit (Promega).

The Mitochondrial ToxGlo™ Assay is a live cell-based assay that measures mitochondrial dysfunction. The assay detects the changes in cell membrane integrity and cellular ATP levels. Firstly, cell membrane integrity is analysed via detection of dead cell protease activity. If treatments are cytotoxic then the added fluorogenic peptide can cross the cell membrane and give significant signal as compared to viable cells of control. Next, ATP detection reagent is used to lyse the cells and generate a luminescent signal. To minimise the ATP production from glycolysis, all treatments were done in DMEM containing Galactose and in the absence of serum to avoid Glucose. Our data showed that there is a reduced ATP production when cells were treated with TNF-α or Positive control-mitochondrial toxin, highlighting the mitochondrial dysfunction during inflammatory response. However, pre-treatment with PTP1B inhibitor, Claramine, protects HUVECs from TNF-α induced mitochondrial dysfunction (Fig. 3.24). In parallel, cytotoxicity was measured, which indicated no significant difference among various treatments, indicating that the observed depletion of ATP, especially in TNF-α treatment, is not due to necrosis, but rather due to the inherent mitochondrial dysfunction.
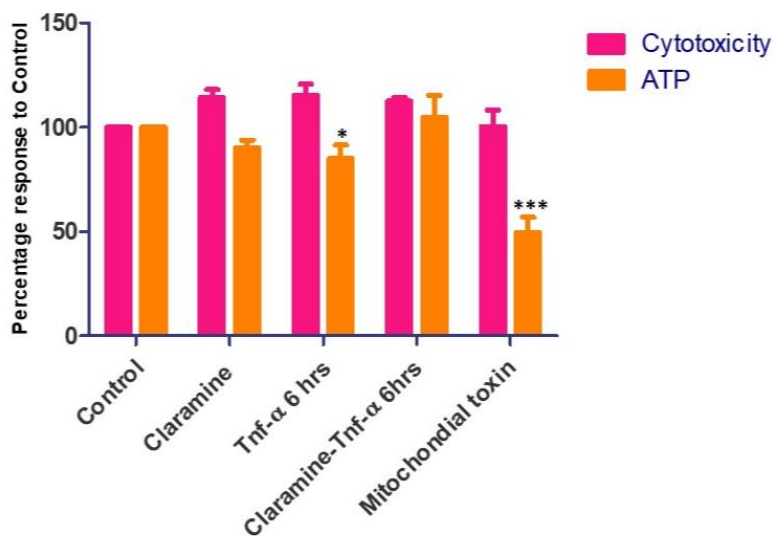
Fig. 3.24. Evaluation of mitochondrial toxicity in *in-vitro* inflammatory model. HUVECs were treated in following groups as 1. not-treated control, 2. Claramine only-, TNF-α-only-, Claramine+TNF-α and Mitochondrial toxin (Sodium Azide). The percentage of Cytotoxicity (pink) and ATP production (orange) was measured by using Mitochondrial ToxGlo kit (Promega). Values are mean ± SEM of two biological replicates and asterisks indicate statistical significance of *** $p < 0.001$, and * $p < 0.05$.

Our data showed that KO-TAC heart improved cardiac function after deletion of endothelial specific *PTP1B* because of improved mitochondrial function.

4. Discussion

Atherosclerosis, a chronic inflammatory disorder of vascular system, is one of the major contributing cause in development and progression of CVDs including coronary artery disease and heart attack (Verstraete, 1990; Zampetaki *et al.,* 2010). Inflammatory response can lead to ECs activation and dysfunction which is considered as initiative trigger in the development of atherosclerosis (Chien, 2008; Xiao *et al.,* 2014). Hypertension, hyperglycemia, disturbed blood flow, hypercholesteremia, and inflammatory mediators in blood like LPS (secreted by microbes) and TNF-α (secreted by cells, in response to LPS) can initiate inflammatory response in ECs via activation of NF-κB (Fig. 4.1) (Bleakley *et al.,* 2015; Dart and Chin-Dusting, 1999; Hadi *et al.,* 2005; Higashi *et al.,* 2012; Messner and Bernhard, 2014).
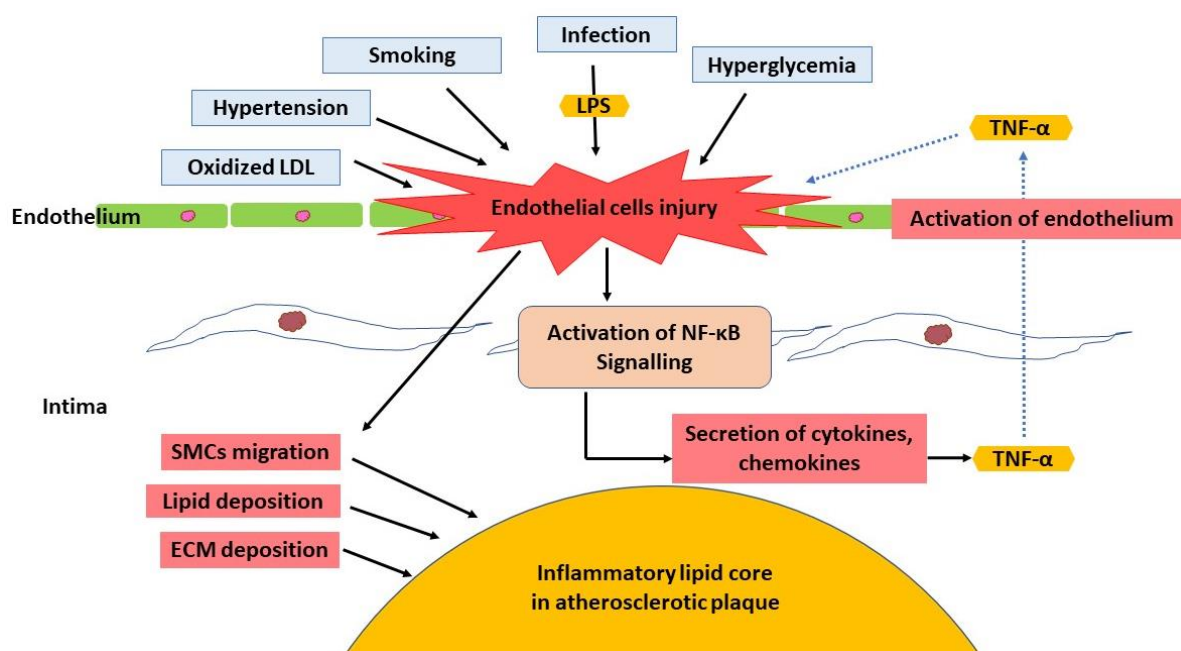
Figure 4.1. Factors involved in ECs activation, inflammation, and in atherosclerotic plaque development Factors involved in ECs activation, inflammation, monolayer disruption and progression of atherosclerotic plaque development**.** Smoking, hypertension, hyperglycemia, and LPS secreted by bacteria can cause ECs injury which results in activation of NF-κB signalling pathway. Cytokines, chemokines and growth factor secreted by activated ECs participate in further the development of atherosclerotic plaque.

Among these causative agents LPS and TNF-α, pro-inflammatory mediators, are used for establishing *in-vitro* inflammatory models. LPS and TNF-α lead to ECs activation, expression of adhesion molecules on ECs and activation of various signalling pathways including NF-κB pathway. LPS secreted by bacteria activates toll like receptor 4 (TLR4),

which leads to CD14 dependent activation of Src-kinase which phosphorylates Caveolin-1 (Cav-1) (Wong *et al.,* 2004). Phosphorylated Cav-1 leads to formation of a complex including Interleukin receptor associated kinase 1 (IRAK1), (IRAK4) and Myeloid differentiation primary response 88 (MyD88) which leads to NF-κB signalling pathway activation (Fig. 4.2) (Jiao *et al.,* 2013; Wong *et al.,* 2004).
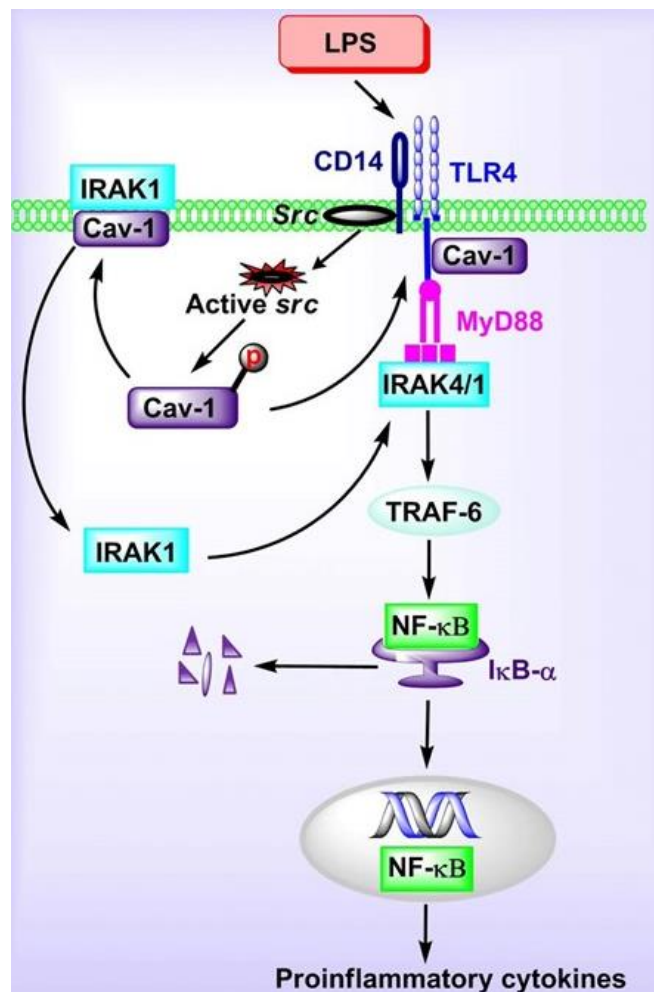
Figure 4.2. LPS mediated NF-κB activation LPS activates TLR4 which leads to CD14 mediated activation of Src-kinase which phosphorylates Cav-1. Phosphorylated Cav-1 leads to formation of IRAK1-IRAK4-MyD88 complex formation which leads to TRAF-6 based activation of IκB kinase which activates NF-κB signalling pathway (Figure published by Jiao *et al.,* 2013).

TNF-α, a proinflammatory cytokine, binds to ECs surface via tumor necrosis factor receptor (TNFR) and activates NF-κB signalling pathway via activation of IκB kinase. TNF-α stimulation leads to multiple changes leading to ECs dysfunction (Zhang *et al.,* 2009). These changes include reduced eNO production, reduced ECs specific vasodilation and vascular repair. It also increases oxidative stress, apoptosis, vascular inflammation, cell

infiltration which contributes in the development of atherosclerosis (Fig. 4.3) (Zhang *et al.,* 2009).

Nf-κB, a key mediator of inflammation, translocates from cytoplasm into nucleus and initiates transcription of pro-inflammatory markers (Brown *et al.,* 2014; Xiao *et al.,* 2014). Inflammatory markers include adhesion molecules like *VCAM-I* and *SELE* which are expressed on activated ECs and binds to monocytes (Gerhardt and Ley, 2015). Activated ECs also release cytokines like *IL6* and *IL8* which further recruits immune cells to ECs (Gerhardt and Ley, 2015; Ramji and Davies, 2015).
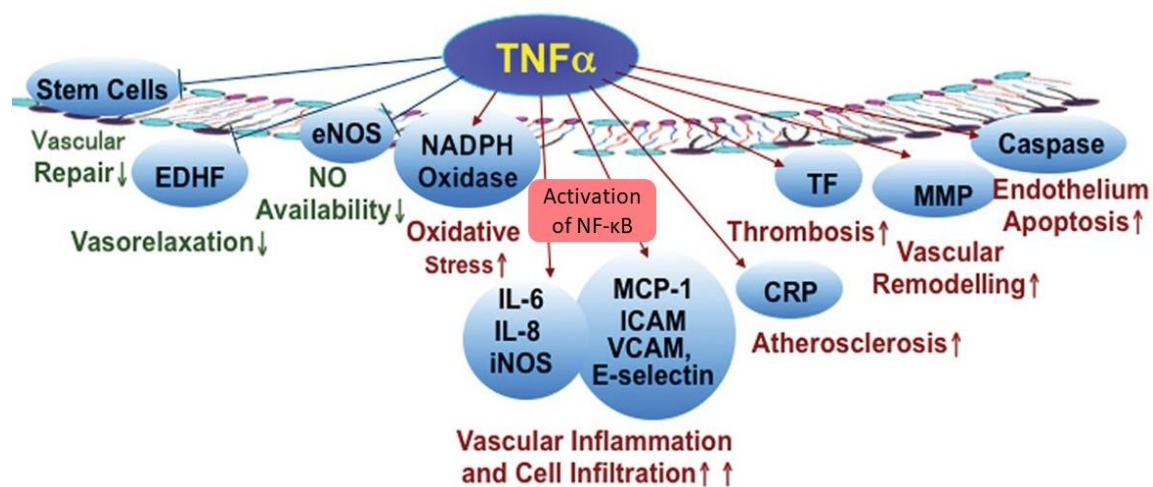

Figure 4.3. TNF-α mediated NF-κB activation contributes in ECs dysfunction TNF-α activates TNFR which leads to activation of IκB kinase which activates NF-κB signalling pathway. Activated NF-κB contributes in inflammation and increases cellular infiltration across ECs monolayer (Figure adapted from Zhang *et al.,* 2009).

We used HUVECs as our *in-vitro* model for induction of inflammation in atherosclerosis and first to study the function of BRD4 in this model system. In agreement with the literature, HUVECs treated with TNF-α showed successful translocation of NF-κB into nucleus as compared to control cells. Our data shows significant increase of pro-inflammatory markers *SELE* and *VCAMI* in HUVECs after TNF-α treatment. Together, localisation of NF-κB inside the nucleus and overexpression of pro-inflammatory markers confirms the establishment of inflammatory phenotype in HUVECs.

BRD4 is an epigenetic factor and a member of transcription initiation machinery. It recognises and binds to the acetylated chromatin and recruit RNA polymerase to initiate transcription (Crowe *et al.,* 2016; Devaiah *et al.,* 2016; Devaiah *et al.,* 2012). BRD4 is involved in multiple cellular activities but its role in inflammation came into view in 2013

where BRD4 was reported as a partner of NF-κB on chromatin during inflammation (Xu and Vakoc, 2014a). To elaborate the role of BRD4 during inflammation, we used HUVECs as *in-vitro* model. We first used JQ1, a classical inhibitor of BRD4 to inhibit the function of BRD4. JQ1 binds to bromodomain I and II of BRD4 with hydrogen bonding interaction and blocks its ability to bind to acetylated chromatin (Bid and Kerk, 2016). We first treated the HUVECs with JQ1 followed by TNF-α treatment. Our data showed that pre-treatment with 500 nM of JQ1 for 4 hrs significantly reduced the expression of inflammatory markers. We observed ˜10-fold and ˜17-fold reduction in expression of SELE and VCAM-I, respectively, as compared to TNF-α-only treated cells. These results are in support of previous studies that showed BRD4 binds to SE regions of pro-inflammatory genes along with NF-κB during inflammation. These results also indicate that the inhibition of BRD4 function reduces the expression of *BRD4* and pro-inflammatory markers during inflammation.

Further on our immunostaining data showed that inhibition of BRD4 function did not affect the subcellular localization of Nf-κB. These results confirm that JQ1 treatment does not affect the NF-κB translocation into the nucleus during inflammatory response and the observed reduced expression of inflammatory markers is due to inhibition of BRD4 function.

JQ1 is an efficient inhibitor of BRD4, however, it also interacts with other members of BET family (Huang *et al.,* 2016; Huang *et al.,* 2017). Short half-life of JQ1 also make it unsuitable for animal studies and clinical trials (Wadhwa and Nicolaides, 2016). Hence, we decided to analyse another inhibitor of BRD4, RVX208, which is orally active and was already in clinical trials for atherosclerosis, diabetes, Alzheimer's disease, and chronic kidney disease (Picaud *et al.,* 2013; Wadhwa and Nicolaides, 2016). It has been reported that RVX208 treatment increases the apolipoprotein A-I (Apo-A-I) and High-density cholesterol (HDL) in blood which reduces multiple adverse effects observed in cardiac patients (Ghosh *et al.,* 2017). Interestingly, *BRD4*, but not *BRD2* and *BRD3*, knockdown increases the mRNA levels of *Apo-A-I* confirming it as a target of BRD4 (Zengerle *et al.,* 2015). Isothermal titration calorimetry studies on BET proteins with RVX208 showed 4-fold higher binding affinity of RVX208 to BRD4 as compared to other BET family members (Kempen *et al.,* 2013).

Collectively from literature review we know that RVX208 is a stable, orally active, already in clinical trials drug which blocks BRD4 activity and improves the cardiac function (Gilham

et al., 2016). Keeping these facts in mind, we decided to comparatively analyse effects of RVX208 and JQ1 in our studies. Previous studies have used variable concentrations of JQ1 for variable time points including 250 nM for 6 hrs (Huang *et al.,* 2016), 500 nM for 3 hrs (Huang *et al.,* 2017), 500 nM for 4 hrs (Picaud *et al.,* 2013), 500 nM for 24 hrs (Bid *et al.,* 2016) and 1-2 µM of JQ1 for 24 hrs (Bid *et al.,* 2016).

As per our knowledge there are no studies reporting the RVX208 treatment on HUVECs. However, we found two studies on primary human hepatocytes which showed treatment with 30 µM RVX208 for 24 and 48 hrs for inhibition of BRD4 (Gilham *et al.,* 2016; Wasiak *et al.,* 2016). Another study on C11 macrophage cell line used 50 to 100 µM of RVX208 for 72 hrs (Lu *et al.,* 2017). In order to establish RVX208 concentration necessary to inhibit the inflammatory phenotype, we initially used different concentrations of RVX208 for 4 hrs which did not reduce the expression of inflammatory markers even at higher concentration of 200 µM. We treated HUVECs with 30 and 60 µM of RVX208 for 12-, 24- and 48-hrs followed by TNF-α for 12 hrs. We observed 12 hrs pre-treatment was significantly reducing the expression of pro-inflammatory marker. On the basis of these experiments, we treated HUVECs with 60 µM of RVX208 followed by 12 hrs TNF-α treatment for BRD4 inhibition. As we did not find any difference in 4 hrs and 12 hrs treatment with JQ1 we used 500 nM of JQ1 for 12 hrs followed by 12 hrs TNF-α treatment.

Comparative analysis indicated that 12 hrs pre-treatment with RVX208 reduces the expression of *SELE* by 2.8-fold and of *VCAM-1* and *IL6* by 3-fold and 7-fold, respectively, as compared to TNF-α treatment. However, pre-treatment with JQ1 reduces the expression of *SELE* by 6-fold and of *VCAM-1* and *IL6* by 8-fold and 10-fold, respectively, as compared to TNF-α treatment. This indicates that both JQ1 and RVX208 could efficiently inhibit the inflammatory response, however, JQ1 is rather more efficient than RVX208, and the reason could be non-specific interaction of JQ1 with BRD2 and BRD3, if any (Bid and Kerk, 2016; Huang *et al.,* 2016; Huang *et al.,* 2017; Wadhwa and Nicolaides, 2016; Zengerle *et al.,* 2015). Interestingly, BRD4 is highly expressed in ECs as compared to BRD2 and BRD3 hence the results obtained with JQ1 might be directly attributable to BRD4 inhibition in these cells (Huang *et al.,* 2016).

Another interesting observation from our treatments was whenever we treat the cells with RVX208-only or JQ1-only we observed the reduction of *VCAM-I* and *IL6* expression as compared to DMSO control. RVX208-only treatment reduced the expression of *VCAM-I*

and *IL6* by 1.4-fold and 3-fold, respectively. Similarly, JQ1-only treatment reduces the expression of *VCAM-I* and *IL6* by 2.5-fold and 2.3-fold, respectively. This data shows that BRD4 is also responsible for basal level gene expression of *VCAM-I* and *IL6*, therefore, in presence of only inhibitors basal level gene expression of these genes is also reduced. Brown *et al.* (2014) performed ChIP-Seq analysis and identified BRD4 binding on SEs of several pro-inflammatory genes including *VCAM-I* in presence and absence of TNF-α.
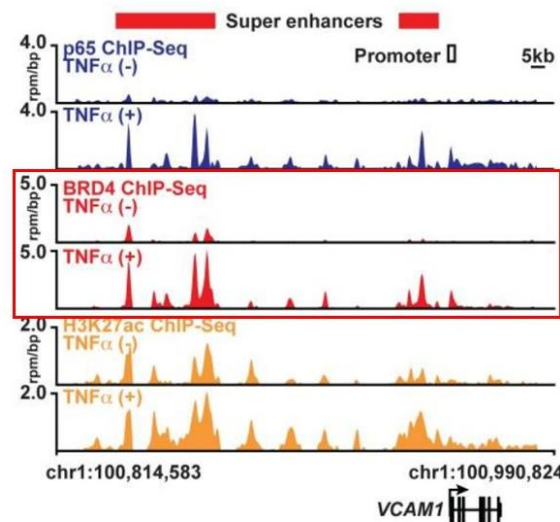

Figure 4.4 BRD4 genome binding in absence and presence of TNF-α. Heat maps showing gene track ChIP-seq signals for BRD4 (red) at *VCAM-I* loci untreated (top) and TNF-α treated (bottom). (Figure published by Brown *et al.,* 2014).

In normal resting ECs, BRD4 binds at *VCAM-I* enhancer region and that binding increases upon treatment with TNF-α (Fig. 4.4). This evidence shows that BRD4 binds to SEs region of *VCAM-I* , and perhaps also on *IL6*, in resting ECs. This might be the reason for the observed reduced expression of both genes in RVX208-only and JQ1-only treated cells.

BRD4 isoforms namely BRD4-long (BRD4-L) and BRD4-short (BRD4-S) are known for their differential roles in different diseases. In particular, over expression of BRD4-S is associated with enhanced metastasis in colon and breast cancers (Alsarraj *et al.,* 2013; Hu *et al.,* 2015). On the other hand, BRD4-L isoform has been reported to reduce metastasis (Alsarraj *et al.,* 2013; Hu *et al.,* 2015). Owing to these facts we were interested to determine the expression of BRD4 isoforms in normal as well as in inflammatory states of ECs. Hence, we studied the expression pattern of BRD4 isoforms not only in HUVECs

in normal and inflammatory conditions, but also during BRD4 inhibition studies and in CVDs models like cardiac hypertrophy and aging hearts.

Our data indicated that mRNA expression of *BRD4-total* was high when HUVECs are treated with TNF-α for 12 hrs. We wanted to investigate further that the increased expression of *BRD4* during inflammatory stress is due to higher expression of *BRD4-L* or *BRD4-S*. We analyzed isoform specific mRNA expression and observed in case of inflammatory stimulus both isoforms have non-significant higher expression, however at protein levels we found short isoform to be significantly high during inflammatory stress. Moreover, we also observed BRD4-S high protein expression in cells which were pre-treated with inhibitors followed by TNF-α treatment. As discussed previously that BRD4-S has been known for its role in enhancing cancer metastasis. Similarly, the observed increased expression of BRD4-S during inflammatory response in ECs may indicate its role in ECs dysfunction. However, further studies aimed at selective knock-down of *BRD4* isoforms are necessary to confirm these results.

Similarly, when we treat cells with inhibitors-only we observed reduced expression of *BRD4-total*. These results indicate that BRD4 inhibitors not only inhibit the function of BRD4 but also reduce its expression suggesting auto-regulation of BRD4 expression. These results are in agreement with data of Wang *et al.* (2016) which reported suppression of BRD4 mRNA and protein expression in oral carcinoma cell line (Cal27), when treated with 500 nM to 1 µM of JQ1 (Wang *et al.,* 2016). The reduced expression of *BRD4-total* in our system is due to reduced expression of *BRD4-L* at mRNA and protein levels. We observed higher expression of *BRD4-L* in HUVECs, hence we may conclude that JQ1 and RVX208 both effect *BRD4-L* levels in HUVECs probably because of its higher expression.

Aging is a major non-modifiable risk factor, which contributes in progression of CVDs. Age-specific cardiac remodelling includes left ventricle hypertrophy, fibrosis, cardiomyocytes lengthening, and deposition of ECM in cardiac tissues leads to multiple pathological cardiac conditions (Cheng *et al.,* 2009; Mottonen *et al.,* 2017). One interesting hallmark of age specific cardiac remodelling is isoform shift of Myosin heavy chains in heart. Embryonic heart mainly consists of β-MHC which converts to α-MHC in adult heart (Gupta, 2007; Mahdavi *et al.,* 1984). As the mammals age, β-MHC became dominant again (Gupta, 2007). Similarly, in cardiac hypertrophy, α-MHC disappears, and β-MHC is dominantly expressed (Gupta, 2007; Herron *et al.,* 2001; Hudson *et al.,* 2011). Keeping these changes

in mind, we decided to analyse whether *BRD4* isoforms have any role during cardiac remodelling due to aging and cardiac hypertrophy. The mRNA expression analysis of *Brd4-total*, *Brd4-L* and *Brd4-S* did not show any significant differences in mice hearts of 1 to 18-months-old except for 6-months-old mice heart, which showed significantly higher *Brd4-S* expression. Protein expression of BRD4-S was only detectable till 8-months old and BRD4-L was significantly higher in 18-months-old mice hearts. However, further analysis on older than 18 months could further explain that whether BRD4-L isoform is high at old age or not. It is known that there is an increase in expression of inflammatory genes in pressure overloaded hearts (Chen *et al.,* 2015; Souders *et al.,* 2012). BRD4 inhibition reduces the expression of pro-fibrotic genes and have been recommended as a treatment of fibrosis (Stratton *et al.,* 2017). In this context, we decided to analyse the expression of BRD4 protein in cardiac fibrosis model of TAC mice. Our data showed that there is no significant expression difference in TAC and SHAM mice. This data may indicate that BRD4 isoforms expression may not vary during cardiac remodelling of hearts in hypertrophy or during aging process.

ECs monolayer is classified as largest organ due to its active contribution in physiological pathways (Aird, 2004; Anggard, 1990). It acts as a barrier between blood and tissues and regulates immune system, transport of nutrients and growth of new vessels by secreting biologically active substances (Aird, 2004; Anggard, 1990). Inflammation, microbial infection, ROS and increased oxidative stress due to oxidized LDL in blood can cause ECs monolayer disruption and which can lead to progression of multiple diseases including atherosclerosis (Ji *et al.,* 2015).

We decided to analyse the effect of inflammatory stimulus on ECs barrier function *in-vitro*. HUVEC monolayers were established and were first treated with TNF-α to analyse the effect of inflammatory stimulus. We observed reduction in trans endothelial electric resistance, increase in permeability across the monolayer with 12 hrs of TNF-α treatment. These results support a previous study of Urbano *et al.* (2017), which reported increase of permeability across ECs with TNF-α treatment. Our data also indicate that whenever HUVECs were pre-treated with RVX208 or JQ1 followed by TNF-α treatment inhibited the barrier dysfunction. These results indicate that BRD4 inhibition is reducing the expression of pro-inflammatory cytokines and adhesion molecules and protecting the ECs monolayer from disruption.

Huang *et al.* (2016) previously reported that JQ1 treatment reduced the VEGF-induced permeability by blocking p21-activated kinase-1 (PAK-1) and eNOS activation. From literature review we know that VEGFR2 is also responsible for activation of p38MAPK pathway and in line with this, Huang *et al.* (2017) in another study reported that JQ1 treatment suppresses vascular inflammation via blocking of p38MAPK pathway. Interestingly, our group previously reported increased permeability in human epithelial colorectal adenocarcinoma cells (Caco-2 cells) is due to a cytokine Midkine, an upstream regulator of p38MAPK pathway (Khan *et al.,* 2017). It has been reported that cytokines can modulate the cytoskeleton of ECs and open the gaps between adjacent cells which increase the permeability of ECs monolayers (Ramji and Davies, 2015). Among different cytokines, Midkine is an interesting target as it has been reported to be highly expressed in inflammatory kidney disease and atherosclerosis (Salaru *et al.,* 2013; Salaru *et al.,* 2016).

Based on these evidences, we decided to analyse Midkine expression in ECs monolayer in the presence of inflammatory stimuli. Our data showed increased expression of *MIDKINE* at mRNA level after 6 hrs of TNF-α treatment and it steadily increased until 72hrs of treatment. At protein level we observed MIDKINE to be secreted from HUVECs after 36 hrs of TNF-α treatment and it steadily increased until 72hrs of treatment. This data is in agreement with the higher expression of Midkine during inflammatory response which is responsible for increased permeability (Fig. 4.5) (Salaru *et al.,* 2013; Salaru *et al.,* 2016). In conclusion, our data shows ECs monolayer disruption is due to increased expression of *MIDKINE*. This data is in agreement with previous studies which reported the increased expression of MIDKINE in atherosclerotic plaques (Salaru *et al.,* 2013).
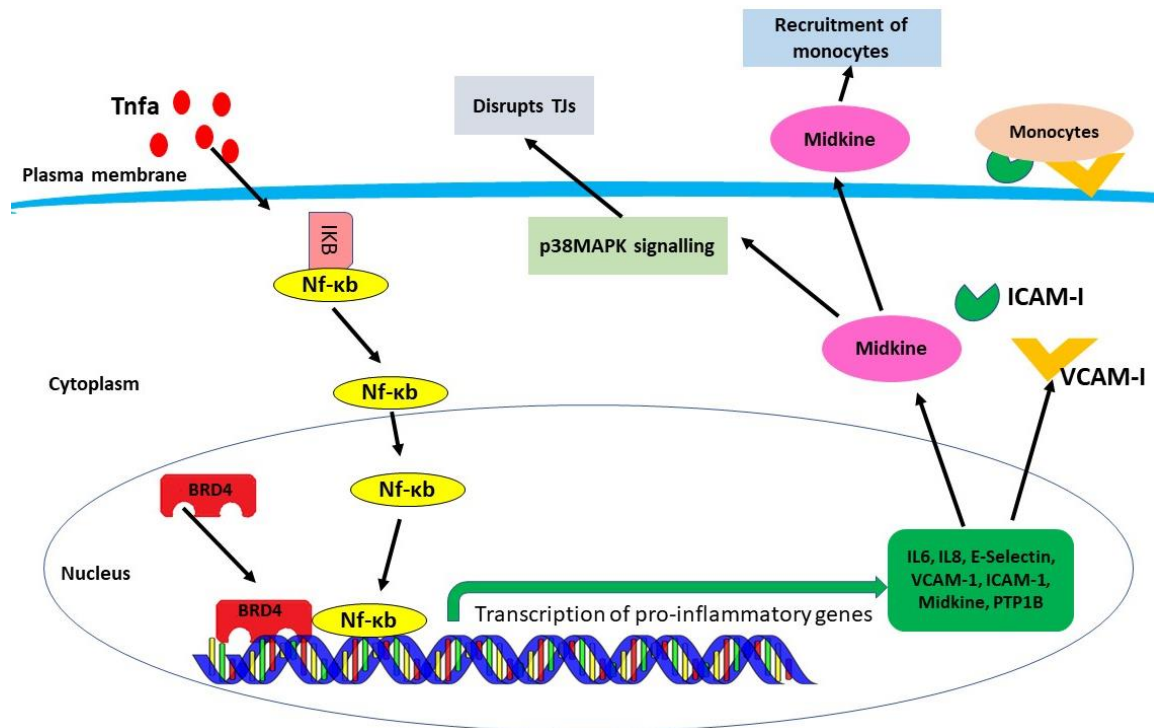
Figure 4.5. Summary of inflammatory response in ECs, Inflammatory stimuli (TNF-α) induces activation and translocation of NF-κB into nucleus. NF-κB along with BRD4 protein transcribe pro-inflammatory markers including 1*: I-CAM*, *VCAM-I*, which express on ECs monolayer and bind to monocytes from blood 2: MIDKINE, which contributes in recruitment of monocytes and activates p38MAPK mediated disruption of tight junctions in ECs and increase the permeability of ECs monolayer.

As our data showed that BRD4 inhibition is protecting ECs monolayer from inflammation and protecting monolayer integrity. We were interested to analyse what is the effect of BRD4 inhibition on expression of Midkine. Our data shows that pre-treatment with RVX208 or JQ1 significantly reduces the expression of Midkine at mRNA and protein levels. On the basis of these results we concluded that BRD4 inhibition not only protecting ECs from inflammatory phenotype but also protecting their barrier function via reducing the expression of Midkine (Fig. 4.6). Taken together, further animal studies should be conducted to analyses effect of BRD4 *in-vivo* to decide whether BRD4 inhibition could be used as therapeutic approach in treatment of atherosclerosis and other inflammatory diseases.
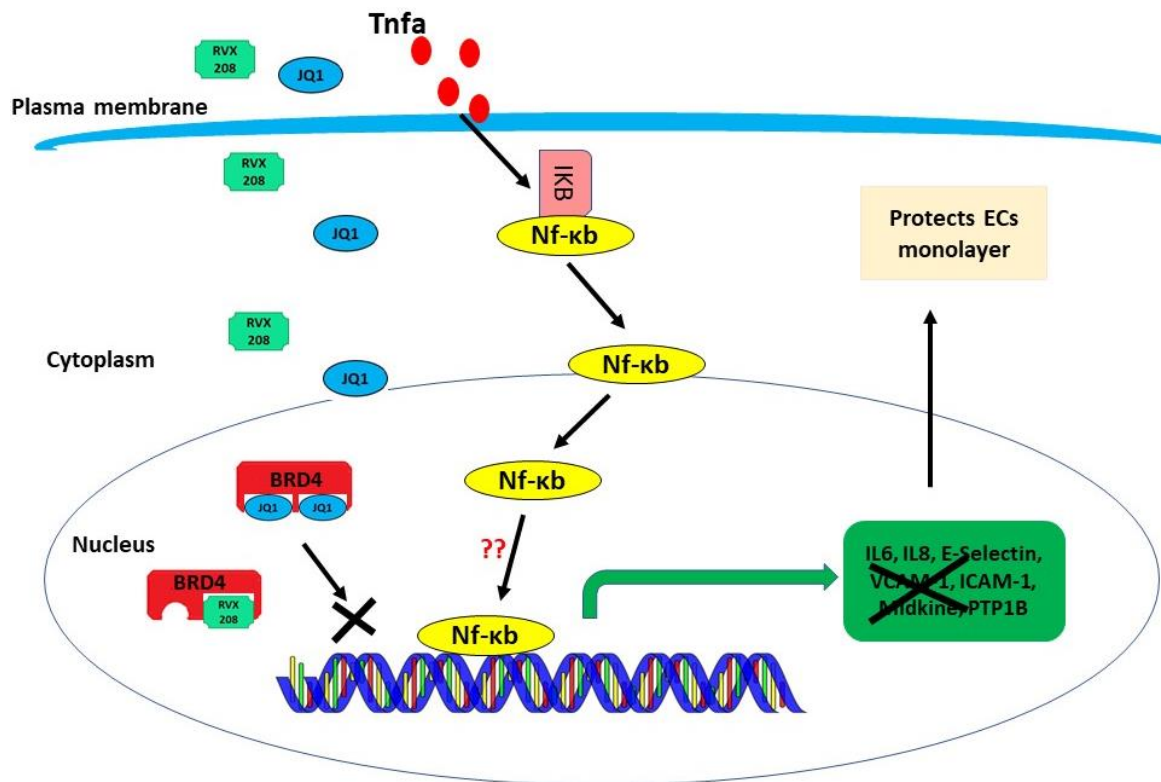
Figure 4.6 BRD4 inhibition reduces the expression of pro-inflammatory markers: Small molecular inhibitors of BRD4 binds to BRD4 bromodomains and inhibits its binding to chromatin, which reduces the expression of pro-inflammatory markers and protects ECs from activation and tight junction disruption.

Next, we wanted to study the role of PTP1B, a target of BRD4 and NF-κB pathway and it has been reported to be overexpressed during inflammation (Zabolotny *et al.,* 2008). PTP1B is a phosphatase which is ubiquitously expressed in mammalian tissues and is responsible for activation and deactivation of multiple signalling pathways (Zabolotny *et al.,* 2008). PTP1B dephosphorylates insulin receptor, EGFR/VEGFR receptor, platelet derived growth factor receptor (PDGFR), Colony stimulating factor 1 receptor (CSFR-1), and insulin growth factor receptor (IGFR) (Fig. 4.7). In ECs, PTP1B overexpression leads to ECs dysfunction, inhibition of VEGFR2 signalling pathway resulting in impaired ECs migration and angiogenesis (Lanahan *et al.,* 2014; Thiebaut *et al.,* 2016; Zabolotny *et al.,* 2008). PTP1B inhibition protects the mice from developing atherosclerotic plaques (Thompson *et al.,* 2017).
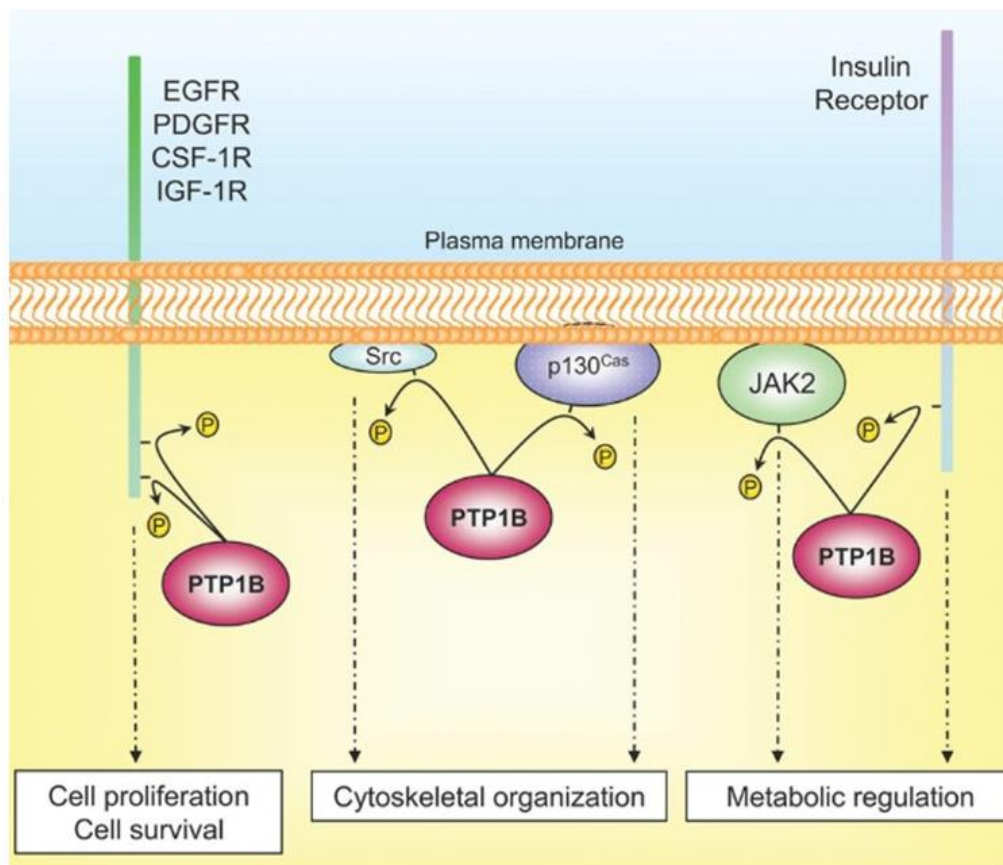
Figure 4.7 PTP1B target receptors: PTP1B dephosphorylates insulin receptor, VEGFR receptor, PDGFR, CSF1R, IGF-1R receptor and regulates metabolic pathways, cytoskeleton organization, cell proliferation and survival. (Figure published by Tiganis *et al.,* 2007).

We observed significantly higher expression of PTP1B gene and protein in HUVECs, when treated with TNF-α. These results are in agreement with previous studies on muscle myoblasts cell line (C2C12) and adipose tissues, which showed over expression of PTP1B when treated with TNF-α (Panzhinskiy *et al.,* 2013; Zabolotny *et al.,* 2008).

PTP1B inhibition studies have shown it as a promising approach in treatment of obesity, diabetes, hypertension, ECs dysfunction, cardiac dysfunction, and cardiac inflammation (Ali *et al.,* 2009; Bruder-Nascimento *et al.,* 2015; Coquerel *et al.,* 2014). A recent study by Gogiraju *et al.,* 2016 showed ECs specific deletion of PTP1B (Endo.*Ptp1b*.KO) protects the mice from cardiac hypertrophy and cardiac fibrosis in TAC model (Gogiraju *et al.,* 2016). However, it was intriguing to further investigate the proteins and pathways which were affected in *Endo.Ptp1b.KO* heart tissues. To answer this, we performed a quantitative global proteome analysis on wild type and *Endo.Ptp1b.KO* mice with and without induced pressure via aortic constriction.

Our proteomic analysis could identify 899 proteins in all four groups (WT-SHAM, WT-TAC, KO-SHAM, KO-TAC) with differential expression, however with 1% FDR we could quantify and consider only 697 proteins for further analysis. Previously, proteomic studies on TAC mice reported 538 proteins (Dai *et al.,* 2013). As per our knowledge this is the first study to show cardiac proteome analysis of ECs with *Ptp1b* specific deletion.

Our data showed only 8 up-regulated and 58 down-regulated proteins in KO-SHAM as compared to WT-SHAM. Pathway analysis showed that all these proteins do not belong to one specific pathway but included interesting targets like Gap junction alpha-1 protein, Calnexin, ribosomal proteins, Glutathione oxidase and cytoskeleton proteins. Gap junction alpha-1 protein (GJA1), also known as connexin43, is one of the major cardiac gap junction protein and a marker of cardiac lineage (Eshkiki *et al.,* 2017; Kurtenbach *et al.,* 2014). It has been reported that PTP1B knock down results in overexpression of GJA1 which interrupts the embryonic stem cells differentiation towards cardiac lineage (Eshkiki *et al.,* 2017). Interestingly, a previous study has reported that reduced expression of GJA1 is a marker of congestive heart failure (Kurtenbach *et al.,* 2014). In line with these previous observations, our data showed 2-fold up-regulation of GJA1 in KO-SHAM as compared to WT-SHAM which may indicate improved cardiac gap junctions in *Ptp1b* KO animals. Calnexin is an endoplasmic reticulum (ER) membranous protein which is responsible for folding of secretory and membrane bounded proteins (Lee *et al.,* 2015). It has been reported that Calnexin forms a complex with C-terminal of PTP1B and act as an anchor of PTP1B in ER (Lee *et al.,* 2015). We observed a 2-fold decreased expression of Calnexin in KO-SHAM. This data suggests that KO of PTP1B leads to down-regulation of Calnexin through unknown mechanism. Moreover, it has also been reported that Calnexin-PTP1B interaction recruits PTP1B to ribosome-translocon complex ensuring its post-translation modification role on various targets (Lee *et al.,* 2015). Ribosome translocon complex includes ribosomal subunits like 60S and 40S (Voorhees *et al.,* 2014). Interestingly we observed reduced expression of multiple ribosomal protein of 60S subunit (Proteins: P1, L4, L27A and L29) and of 40S subunit (S4, S9 and S16) up to 1.5-fold to 2-fold. However, we did not find any translocon protein to be down-regulated. Oxidative stress leads to inactivation of PTP1B via its oxidation (Geraghty *et al.,* 2013). Glutathione peroxidase (Gpx) is a common intracellular antioxidant enzyme which has higher activity in response to inflammatory stimuli and oxidative stress (Geraghty *et al.,* 2013; Mobasher *et al.,* 2013). It has been reported that Gpx-activity did not increased in PTP1B deficient hepatocytes

during induced hepatotoxicity and cells show increased antioxidant defence (Mobasher *et al.,* 2013). We observed 2-fold down-regulation of Gpx in KO-SHAM tissues which may indicate that Ptp1b deletion protects the hearts against ROS stress. PTP1B is known to regulate adhesion and migration of cells via dephosphorylation of cytoskeleton proteins like Actin, Filamin C, Cofilin and Fibrinogen (Arregui *et al.,* 2013; Sumi *et al.,* 1999; Wang *et al.,* 2018). Cellular movements depend on polymerisation and depolymerisation of actin cytoskeleton (Sumi *et al.,* 1999). VEGFR phosphorylation leads to activation of p38MAPK pathway which induces actin polymerisation via phosphorylates of cofilin, an acting binding protein (Wang *et al.,* 2018). PTP1B is a regulator of VEGFR signalling and PTP1B deletion from ECs leads to increased phosphorylation of VEGFR (Gogiraju *et al.,* 2016; Lanahan *et al.,* 2014). Interestingly we found that in absence of PTP1B multiple cytoskeleton proteins are more than 2-fold down-regulated including fibrinogen and actin related proteins: cofilin and filamin C. This data shows that absence of PTP1B may not only affect the cytoskeleton proteins function but also might affect their expression. Hence, further studies are important to answer these observations.

Next, we analysed WT-SHAM and WT-TAC proteins and our data showed 60 up-regulated and 70 down-regulated proteins in WT-TAC as compared to WT-SHAM. Multiple previous studies analysed TAC hearts for global proteome, however, we reported highest number of differentially regulated proteins in WT-TAC mice which is 130 proteins as compared to previously reported 123 (proteomics study) and 95 (transcriptomics + proteomics study) (Dai *et al.,* 2013; Lau *et al.,* 2018). Pathway analysis showed that up-regulated proteins exhibit one cluster of cytoskeleton proteins. It has been reported previously that pressure overloaded hearts exhibit increased density of microtubules component which contributes to stiffness of cardiac muscle (Dai *et al.,* 2013; Lau *et al.,* 2018; Tagawa *et al.,* 1997). We observed some interesting cytoskeleton proteins in WT-TAC, including Myosin heavy chain, Four and a half LIM domains 1 (FHL1) and β-Tubulin, to be up-regulated.

Myosin is a main molecule of thick filament of cardiac muscle which generates movement by hydrolysis of ATP (Gupta, 2007). Myosin consists of 2 heavy chains (MHCs) (encoded by gene α and β) and four light chains (MLCs) (Gupta, 2007; Mahdavi *et al.,* 1984). In rodents β-MHC expresses predominantly in ventricles and before birth, expression of α-MHC starts to increase in ventricles and dominates in young rodents (Gupta, 2007). Isoform shift of Myosin from α-MHC to β-MHC is an important hallmark of hypertrophy (Gupta, 2007; Herron *et al.,* 2001; Hudson *et al.,* 2011). We observed 22-fold up-regulation

in β-MHC in WT-TAC as compared to WT-SHAM further validating our proteome analysis. Four and a half LIM domain proteins domain (FHL) proteins, such as FHL1 are non-enzymatic proteins associated with cytoskeleton (McGrath *et al.,* 2006). Higher expression of FHL1 at transcriptome and proteome level is considered as a marker of cardiac hypertrophy (Dai *et al.,* 2013; Lau *et al.,* 2018). We observed 4-fold up-regulation of FHL1 in WT-TAC mice as compared to WT-SHAM. On the other hand Tubulin protein is a dimer of α- and β-tubulin and it has been reported that β-tubulin expression is high in human failing hearts with cardiac hypertrophy (Aquila-Pastir *et al.,* 2002). We also observed 2.4-fold higher expression of β-tubulin in hypertrophic TAC mice.

Interestingly in down-regulated proteins of WT-TAC, we observed one major cluster consisting of mitochondrial associated proteins. Previous studies have also reported that pressure overloaded hearts have mitochondrial dysfunction due to down-regulation of oxidation-reduction associated proteins, fatty acid metabolism proteins and electron transport chain associated proteins (Dai *et al.,* 2013; Lau *et al.,* 2018). Mitochondrial dynamics change during cardiac remodelling in CVDs (Vasquez-Trincado *et al.,* 2016). Myocardial infarction, atherosclerosis, diabetic cardiomyopathy and cardiac hypertrophy poses increased energy demand stress on mitochondria in cardiac tissue which leads to cell death, mitochondrial DNA damage, and metabolic disorder, respectively (Fig. 4.8) (Vasquez-Trincado *et al.,* 2016).
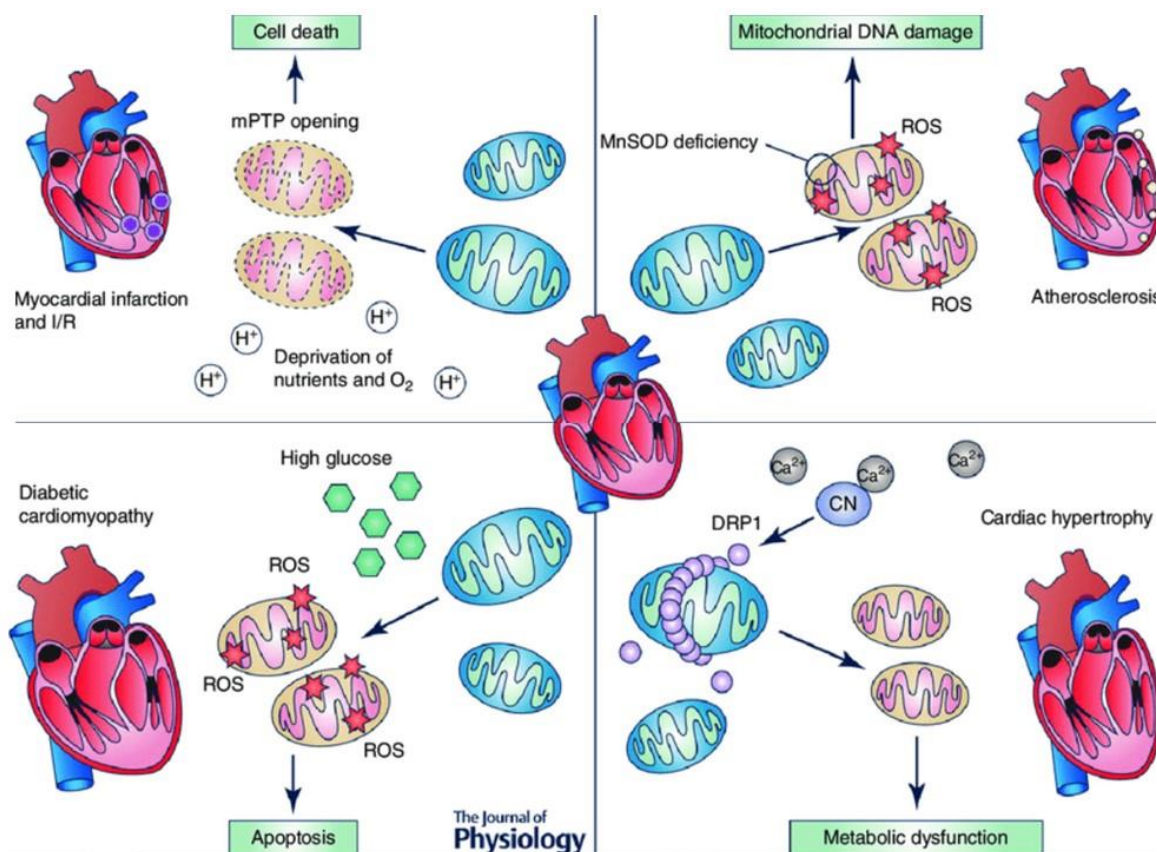
Figure 4.8 Mitochondrial dysfunction in CVDs: CVDs leads to extensive cardiac remodelling and metabolic stress on cardiac tissues. In myocardial infarction cardiac cells are deprived of oxygen and nutrients which leads to mitochondrial permeability transition pore opening ((mPTP) causing cell death. Cardiac tissues face higher ROS in atherosclerosis which cause mitochondrial DNA damage. In diabetic cardiomyopathy, apoptosis is high due to increased ROS production. In cardiac hypertrophy, pressure overload leads to increase demand of mitochondrial biogenesis and energy production and failure of it leads to increase demand of mitochondrial biogenesis and energy production and failure leads to metabolic dysfunction in hypertrophic hearts (Figure published by Vasquez *et al.,* 2016).

Previously, proteomic study and IPA analysis on pressure overload heart showed attenuated mitochondrial function, oxidative phosphorylation and Rho based actin cytoskeleton polymerisation (RhoGDI signalling) and Rho GTPase signalling (Dai *et al.,* 2013). In support of these findings our WT-TAC data after IPA analysis showed similar results (Fig.4.9). We observed attenuated pathways including oxidative phosphorylation (p value 5.19 e^{-05}), mitochondrial dysfunction (p value 1.97 e^{-04}), RhoGDI signalling (p value 2.19 e^{-04}), and Rho Family GTPases signalling (p value 6.15 e^{-04}) (Fig. 4.9).

Furthermore, IPA analysis revealed a list of possible phenotypic symptoms on the basis of differentially regulated proteins which includes cardiac arrythmia, dilation, heart failure, cardiac fibrosis and cardiac infarction (Fig. 4.11). Interestingly these phenotypic symptoms

resemble to TAC induced cardiac hypertrophy in WT mice hearts. This data also validates the hypertrophy in WT mice.

Summary of Analysis - Observation 2

Top Canonical Pathways	
Name	p-value
Oxidative Phosphorylation	5.19E-05
Mitochondrial Dysfunction	1.97E-04
RhoGDI Signaling	2.19E-04
Signaling by Rho Family GTPases	6.15E-04
Glycerol-3-phosphate Shuttle	2.73E-03

Cardiotoxicity

Name	p-value
Cardiac Arrythmia	1.43E-02 - 6.83E-04
Cardiac Dilation	3.96E-02 - 1.09E-03
Heart Failure	9.53E-03 - 9.53E-03
Cardiac Fibrosis	1.56E-02 - 1.56E-02
Cardiac Infarction	1.70E-01 - 1.70E-01

Figure 4.9 IPA analysis of WT-TAC proteins compared to WT-SHAM proteins: IPA analysis showing top canonical pathways attenuated in WT-TAC (upper panel) which includes oxidative phosphorylation, mitochondrial dysfunction, RhoGDI signalling and RhoGTPases signalling. IPA analysis also revealed cardiotoxic effect of these proteins and pathways in WT-TAC resembling to hypertrophic heart properties (lower panel).

Further on we analysed which proteins could be more significantly differentially regulated in our proteome data causing above mentioned mitochondrial dysfunction. In support of this hypothesis, we observed in our down-regulated protein data some mitochondrial associated proteins which have been previously reported to be down-regulated during pressure overload. NADH dehydrogenase is a largest enzyme complex consisting of almost 44 subunits and functions in mitochondrial Electron Transport Chain (ETC). It has been reported that NADH dehydrogenase 1- β subcomplex subunit 4 is down-regulated in pressure overloaded failing hearts (Bugger *et al.,* 2010). Interestingly, we found also this protein to be 2.3-fold downregulated in our WT-TAC samples. Moreover, we found also another subunit, NADH dehydrogenase 1- β subcomplex subunit 1, to be down-regulated up to 2-fold.

ATP synthase subunit delta is a subunit of mitochondrial ATP synthase enzyme which is responsible for ATP synthesis and is reported to be downregulated in failing hearts (Bugger

et al., 2010). We observed 2.2-fold down-regulation of ATP synthase subunit delta in WT-TAC. It has been reported that pressure overloaded hearts exhibit down-regulation of multiple fatty acid β oxidation pathway proteins at transcriptome and proteome level (Lau *et al.,* 2018). We observed multiple fatty acid metabolism associated enzymes to be down-regulated in WT-TAC mice including 3-ketoacyl-CoA thiolase (2.79-fold), Methylcrotonoyl-CoA carboxylase (2.62-fold), Carboxylesterase 1 (2.5-fold), Enoyl-CoA delta isomerase 1 (2.3-fold) and biosynthesis O-methyltransferase (2.02-fold). These findings show that WT-TAC had impaired fatty acid metabolism, yet another hallmark of hypertrophy (Lau *et al.,* 2018). Collectively, our data showed down-regulation of above-mentioned proteins which have been reported previously in WT-TAC mice. However, we observed many other mitochondrial associated proteins which have not been reported previously such as ATP binding cassette protein (3.34-fold), Phospholemman (2.12-fold), Sodium/calcium exchanger 1 (2.09), Glutaryl-CoA dehydrogenase (1.86-fold), Acyl-coenzyme A thioesterase 2 (1.86-fold), Enoyl-CoA hydratase (1.77-fold), Hydroxyacyl-coenzyme A dehydrogenase (1.76-fold), Acetyl-coenzyme A synthetase (1.55-fold) etc. Together with the known mitochondrial proteins, all these down-regulated proteins confirm that WT-TAC mice have mitochondrial dysfunction and impaired metabolic pathways.

Table 4.1 shows the comparison of some published studies with our proteomic study, we observed similar pattern of proteins in WT-TAC as published already in different proteomic studies.

Table 4.1. Comparison of our proteomic results with different published LC-MS/MS based proteomic studies on TAC animals

	Dao-Fu Dai *et al.,* 2013	Dao-Fu Dai *et al.,* 2012	Rüdebusch *et al.,* 2017	Bugger *et al.,* 2009	Our study
Animal model	C57BL6 mice	C57BL6 mice	C57BL6 mice	Sprague-Dawley Rat	C57BL6 mice
Heart collection after surgery (days)	28	28	56	140	140
Sample type	Left ventricle	Purified	Left ventricle	Mitochondria	Heart lysates

		mitochondria			
Search engine	SEQUEST	SEQUEST	SEQUEST	....	MASCOT
Statistical test	Two-way ANOVA	Two-way ANOVA	Two-way ANOVA	T-test	T-test
P-value/ Fold change	0.05/1.5-fold	0.05/1.5-fold	0.05/2-fold	0.05/>0.5-fold	0.05/1.5-fold
Number of differentially regulated proteins	121	96	99	70	130
Canonical Pathways	Actin signalling pathway, Rho signalling, Fatty acid, Glycolysis, Oxidative phosphorylation	ETC, Transmembrane transport, ATP synthesis, protein folding	Actin signalling pathway, Rho signalling, Fatty acid, Oxidative phosphorylation	Fatty acid, Oxidative phosphorylation	Actin signalling pathway, Rho signalling, Fatty acid, Glycolysis, Oxidative phosphorylation
Mitochondrial proteins	Downregulated	....	....	Downregulated	Downregulated

Next, we analysed 2 groups having PTP1B deficiency, namely SHAM and TAC. Previously, Gogiraju *et al.,* 2016 reported reduced fibrosis and hypertrophy in KO-TAC. We observed different proteome in KO-TAC as compared to KO-TAC and we found 150 up-regulated and 53 downregulated proteins. Pathway analysis showed that up-regulated proteins includes mitochondrial proteins, proteasome associated proteins and proteins involved in secretion and transportation. In down-regulated proteins we observed small clusters of mitochondria, cytoskeleton, and ribosomal proteins.

As mentioned above WT-TAC mice having higher expression of β-MHC (up to 22-fold) is a major hallmark of cardiac hypertrophy. Unexpectedly, we also observed increased expression of β-MHC (up to 7-fold) in KO-TAC, however, this up regulation is 3-fold less as compared to WT-TAC. Even though PTP1B deficiency in mice is protecting from cardiac fibrosis and hypertrophy, still TAC surgery might be inserting pressure overload on cardiac tissues. KO-TAC showed up-regulation of multiple mitochondrial associated proteins as

compared to SHAM mice. TAC surgery exhibits pressure on cardiac tissues which leads to increased mitochondrial biogenesis to compensate the energy demand (Rosca *et al.,* 2013). However hypertrophic hearts exhibit reduced mitochondrial biogenesis which leads to cellular death (Rosca and Hoppel, 2013). Our data suggest that KO hearts have increased mitochondrial biogenesis and have balance between energy demand and production. KO-TAC mice hearts also showed over-expression of proteasome associated proteins. Proteasomal over-expression can be related to over-expression of proteins in TAC mice to degrade misfolded proteins. However, it has also been reported that down-regulation of PTP1B improves the proteasomal function in neuroblastoma cell lines (Jeon *et al.,* 2017). So, over-expression of proteasomal subunits could be an effect of PTP1B deficiency, in general.

PTP1B-deficient mice hearts are protected from hypertrophy and fibrosis as compared to WT-TAC. Proteome analysis between WT-TAC and KO-TAC mice showed 43 up-regulated and 36 down-regulated proteins in KO-TAC as compared to WT-TAC. STRING analysis showed mitochondrial cluster in up-regulated proteins while in down-regulated proteins showed cluster of ribosomal and cytoskeleton proteins. This data is quite interesting and related to previous discussion that KO-TAC showed less hypertrophy and fibrosis as compared to WT-TAC. Mitochondrial dysfunction is associated with pressure overload in human and mice hearts (Dai *et al.,* 2013; Dai *et al.,* 2012; Lau *et al.,* 2018). Our data showed PTP1B deficiency leads to improved mitochondrial function via increased expression of mitochondrial proteins.

Previously 10 subunits of NADH were found downregulated in WT-TAC mice (Dai *et al.,* 2012). We observed 9 subunits of NADH dehydrogenase to be up-regulated in KO-TAC. We observed some other mitochondrial up-regulated proteins like 3 subunits of Cytochrome b-c1 complex, 3-ketoacyl-CoA thiolase, Cytochrome c oxidase, ATP-synthase subunit delta, Hydroxyacyl-coenzyme A dehydrogenase and NADH-ubiquinone oxidoreductase.

Some other interesting up-regulated proteins include 26S proteasome complex, which have been reported to protect mice from cardiac hypertrophy (Dickhout and Austin, 2006). We also observed up-regulation of Sepiapterin reductase, a crucial enzyme in (6R)-l-erythro-5,6,7,8-tetrahydrobiopterin (BH4) biosynthesis (Sumi-Ichinose *et al.,* 2017). BH4 is an important cofactor of NOS enzyme and it reverses the oxidative stress, cardiac

hypertrophy, and fibrosis in a 5-week-old pressure induced hypertrophy model (Moens *et al.,* 2008; Sumi-Ichinose *et al.,* 2017). Overexpression of Sepiapterin reductase in KO-TAC indicates that PTP1B deficiency in ECs may improving the eNO production which is contributing in reducing the oxidative stress, fibrosis, and hypertrophy. FHL1 a marker of cardiac hypertrophy and was up to 1.77-fold downregulated in KO-TAC as compared to WT-TAC. Glucose transporter 4 (GLUT4) is responsible for glucose uptake and deficiency of it leads to cardiac hypertrophy (Wende *et al.,* 2017). We observed up-regulation of GLUT4 in KO-TAC mice as compared to WT-TAC showing improved glucose metabolism in KO-TAC.

Among down-regulated proteins, we identified multiple ribosomal proteins. As discussed previously that PTP1B deficiency leads to reduced expression of ribosomal proteins. However, as PTP1B deficient hearts have reduced fibrosis and hypertrophy, this might be the reason that there is reduced protein biosynthesis machinery. KO-TAC mice also showed down-regulation of cytoskeleton associated proteins, notably β-MHC, a hallmark of hypertrophy, was down-regulated in KO-TAC as compared to WT-TAC. Elevated levels of Integrin linked kinase, that physically links β-integrins with the actin cytoskeleton, have been reported in human cardiac hypertrophy and induces hypertrophy in mice (Lu *et al.,* 2006). In line with these observations, we found up to 3-fold down-regulation of integrin linked kinase in KO-TAC as compared to WT-TAC. It has been reported that there is an increase in transcription of β1- and β2-tubulin genes in cardiac hypertrophy (Narishige *et al.,* 1999). We observed 2.98-fold down-regulation of Tubulin-β in KO-TAC as compared to WT-TAC. Other than cytoskeleton associated proteins we also observed that KO-TAC mice have decreased expression Carbonic Anhydrase I and II (CA-I and CA-II) as compared to WT-TAC. Carbonic Anhydrases (CAs) are a group of enzymes which .are responsible for the reversible conversion of CO_2 and H_2O in HCO_3^- and H^+. Inhibition of CAs in rats showed reduced hypertrophy. CA-II expression is high in cardiac hypertrophic mice (Alvarez *et al.,* 2013). Interestingly, human hypertrophic ventricles show increased expression of CA-II and CA-IV expression (Alvarez *et al.,* 2013). In our study we found that KO-TAC mice have decreased expression CA-I and CA-II as compared to WT-TAC suggesting Carbon metabolism is balanced in KO-TAC model.
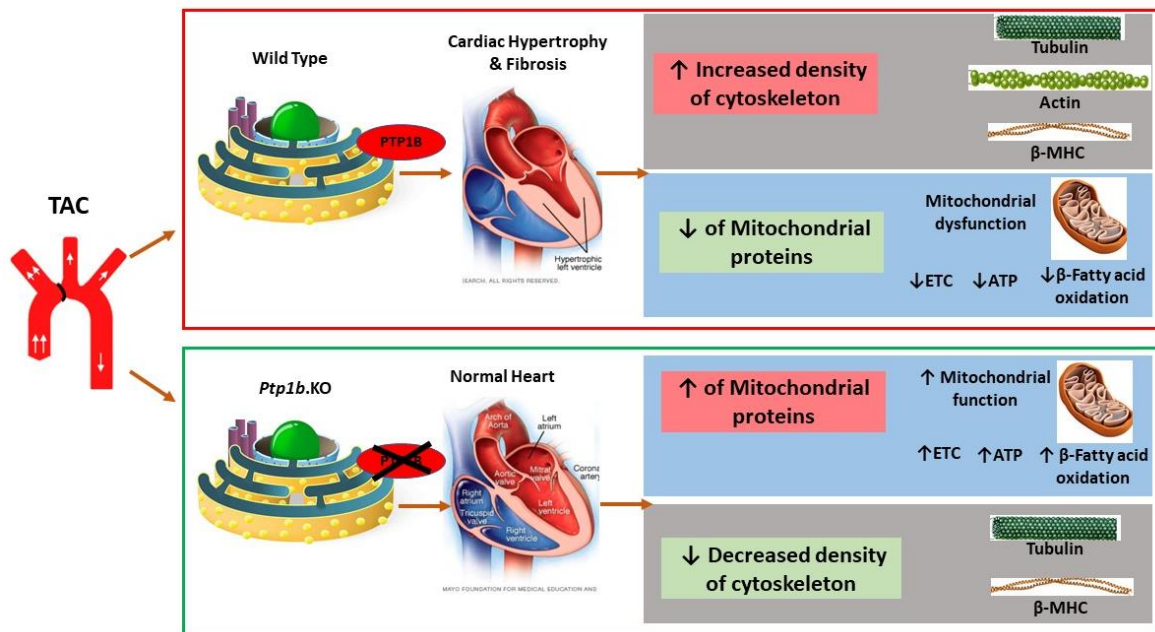
Figure 4.10 Summary of global proteome comparison in WT-TAC and KO-SHAM: TAC operation induces hypertrophy in wild type hearts (upper panel) due to up-regulation of cytoskeleton associated proteins and mitochondrial dysfunction due to down-regulation of mitochondrial proteins related to electron transport chain (ETC), ATP synthesis and Fatty acid metabolism. However, *Ptp1b*.KO mice hearts (lower panel) do not develop hypertrophy and fibrosis in response to TAC due to up-regulation of mitochondrial proteins and down-regulation of cytoskeleton associated proteins.

In summary our proteome data strongly supports that PTP1B deficiency protects the mice from cardiac hypertrophy and fibrosis due to improved mitochondrial function and reduced cytoskeleton density (Fig. 4.10). To support these observations, we performed *in vitro* studies using PTP1b inhibitor in ECs to confirm the improved mitochondrial function. We observed that TNF-α treatment induces the mitochondrial functional stress which leads to reduced production of ATP. This observation is supported a study by Kalogeris *et al.,* 2014, who reported decrease in ATP production and mitochondrial mass in ECs in response to TNF-α (Kalogeris *et al.,* 2014). Furthermore, we were able to analyse successfully that PTP1B inhibition prior to TNF-α treatment in ECs protects the cells from mitochondrial dysfunction as well as the restoration of ATP production.

In conclusion our study elaborates that BRD4 inhibition reduces the inflammation and could be a therapeutic target for atherosclerosis. Furthermore, PTP1B inhibition improves the cardiac function in pressure overloaded hearts by improving the mitochondrial function in *Ptp1b*-KO mice (Fig. 4.11).
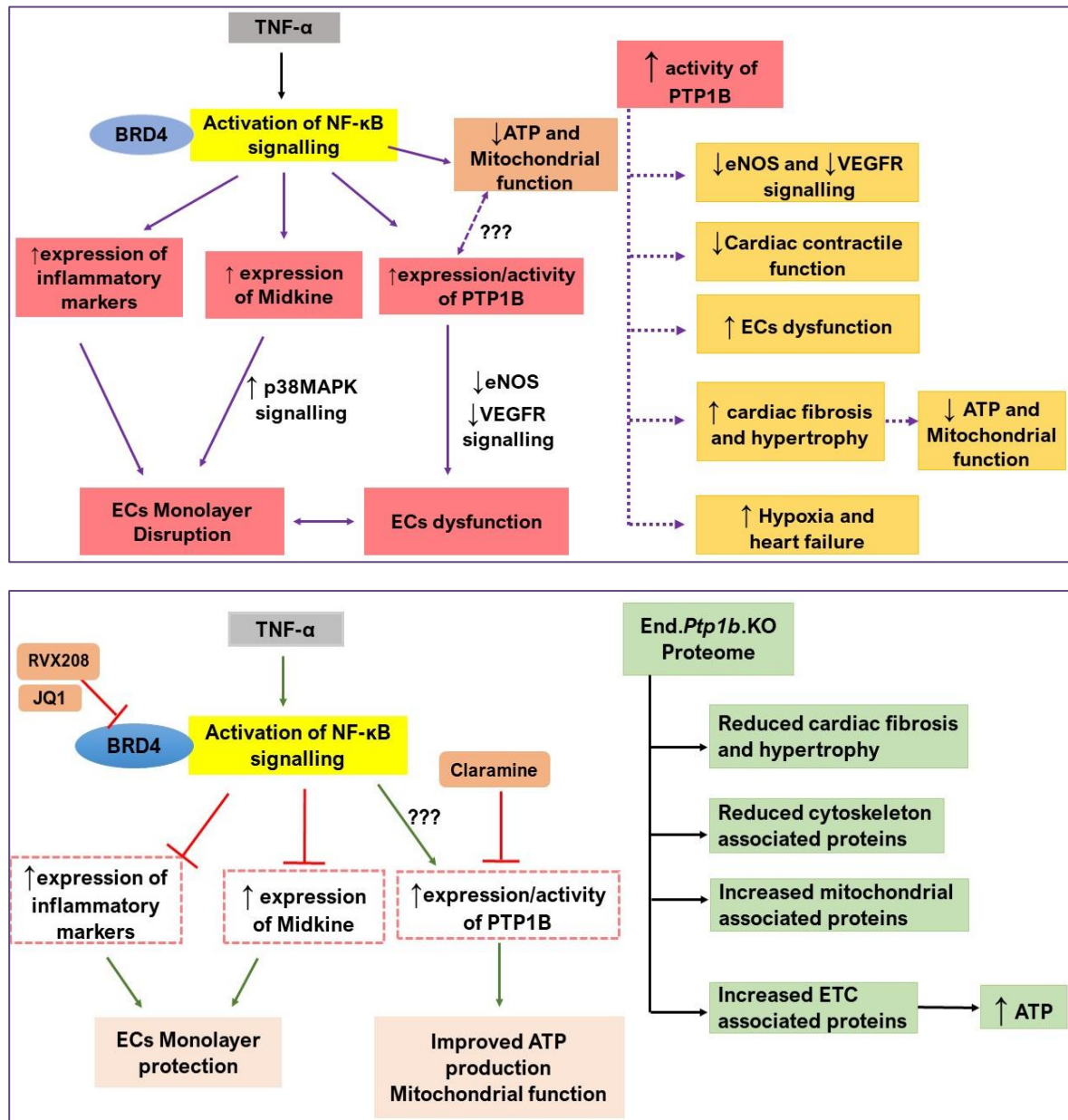
Figure 4.11 Conclusion: TNF-α, BRD4 and PTP1B function on ECs and CVDs: Upper Panel :TNF-α induces activation of NF-κB, BRD4 and NF-κB transcribe inflammatory markers, Midkine and PTP1B. Increased expression of inflammatory markers and Midkine contributes in ECs dysfunction and monolayer disruption. Increased expression of PTP1B is known for reduced expression of eNOS and VEGFR signalling, an indication of ECs dysfunction. Increased activity of PTP1B have been reported to be associated with reduced cardiac contractile function, reduced ATP production, increased cardiac fibrosis, hypertrophy, ECs dysfunction, hypoxia and heart failure. **Lower Panel:** Our data showed RVX208/JQ1 based BRD4 inhibition reduces the expression of inflammatory markers, Midkine and it protects ECs monolayer from disruption. Further studies should be conducted to analyse the effect of BRD4 inhibition on PTP1B expression. Our data showed that PTP1B inhibition with Claramine recovers the ATP production loss induced by TNF-α treatment. Our data showed the Endo.*Ptp1b*.KO reduces the cardiac hypertrophy and fibrosis by reducing the cytoskeleton associated protein expression and increasing the mitochondrial protein expression to compensate the energy demand in pressure overloaded hearts.

5. Summary

Vascular and lymphatic system is lined by Endothelial cells (ECs) monolayer or endothelium. Healthy endothelium maintains vessel functions by releasing different substances including Nitric Oxide (NO). Cardiovascular risk factors induce ECs dysfunction, which leads to the increase permeability of ECs and development of atherosclerosis. In response to inflammatory stimulus, NF-κB signalling pathway becomes activated. NF-κB signalling is responsible for releasing cytokines and expressing adhesion molecules on ECs surface. BRD4 is a chromatin regulator transcription factor, which binds to super enhancers of basal cell state maintaining gene loci. BRD4 redistributes on chromatin during inflammation and along with NF-κB binds to super enhancers of inflammatory gene loci.

In the present study, we analysed the role of BRD4 and its isoforms in ECs dysfunction and investigated whether BRD4 inhibition restores ECs function under inflammation-stimulating conditions. We established an *in vitro* model of inflammatory phenotype using he treatment of HUVECs with TNF-α. Our study indicates that BRD4 short isoform is overexpressed in HUVECs during inflammation along with increased expression of inflammatory markers, Midkine, and PTP1B. Pre-treatment with BRD4 inhibitors (JQ1 and RVX-208) abrogates ECs activation and dysfunction via reducing the expression of pro inflammatory markers. We also observed that TNF-α treated HUVECs showed increased permeability which indicates disrupted monolayer integrity. In contrast, monolayer integrity was retained when HUVECs pre-treated with BRD4 inhibitors.

Elevated levels of Midkine has been reported in human and mice atherosclerotic plaques. It has also been reported to disrupt monolayer integrity via activation of downstream signalling pathways. HUVECs secrete Midkine when treated to 48-72 hours with TNF-α. BRD4 inhibition with JQ1 and RVX208 reduced the Midkine secretion indicating BRD4 inhibition is retaining the monolayer integrity by reduce Midkine signalling. As far as we know, this is the first study that identified the role of BRD4 in regulation of Midkine, an upstream regulator of p38MAPK signalling pathway. Our data pointed out that an orally administered RVX208 drug can contribute in atherosclerosis treatment. Our study gives an indication that BRD4 inhibition can be used as a therapeutic option for treatment of atherosclerosis.

Our results confirms the previous observations stating PTP1B inhibition is beneficial in ECs, *in-vitro* and *in-vivo*. This is the first study to report the heart global proteome of PTP1B-deficient mice and its contribution in prevention of cardiac fibrosis and hypertrophy. Our data shed light on cardio-protective role of PTP1B deletion by identifying the improvement of mitochondrial function in cardiac hypertrophy animals. Furthermore, this report proved in *in-vitro* study that PTP1B inhibition improves the ATP production in ECs. From our results, it can be suggested that PTP1B inhibition can be a therapeutic option in prevention of cardiac fibrosis and hypertrophy after myocardial infarction. This study provides essential understanding into beneficial roles of BRD4 and Ptp1b in CVDs, especially, atherosclerosis and cardiac hypertrophy.

6. Bibliography

Aird, W. C. (2004) Endothelium as an organ system. *Crit Care Med*. **32**:S271-S279.

Ali, M. I., P. Ketsawatsomkron, E. J. Belin de Chantemele, J. D. Mintz, K. Muta, C. Salet, S. M. Black, M. L. Tremblay, D. J. Fulton, M. B. Marrero, and D. W. Stepp. (2009) Deletion of protein tyrosine phosphatase 1b improves peripheral insulin resistance and vascular function in obese, leptin-resistant mice via reduced oxidant tone. *Circ. Res*. **105**:1013-1022.

Alonso, A., J. Sasin, N. Bottini, I. Friedberg, I. Friedberg, A. Osterman, A. Godzik, T. Hunter, J. Dixon, and T. Mustelin. (2004) Protein tyrosine phosphatases in the human genome. *Cell* **117**:699-711.

Alsarraj, J., F. Faraji, T. R. Geiger, K. R. Mattaini, M. Williams, J. Wu, N. H. Ha, T. Merlino, R. C. Walker, A. D. Bosley, Z. Xiao, T. Andresson, D. Esposito, N. Smithers, D. Lugo, R. Prinjha, A. Day, N. P. Crawford, K. Ozato, K. Gardner, and K. W. Hunter. (2013) BRD4 short isoform interacts with RRP1B, SIPA1 and components of the LINC complex at the inner face of the nuclear membrane. *PLoS. One*. **8**:e80746.

Alsarraj, J., R. C. Walker, J. D. Webster, T. R. Geiger, N. P. Crawford, R. M. Simpson, K. Ozato, and K. W. Hunter. (2011) Deletion of the proline-rich region of the murine metastasis susceptibility gene Brd4 promotes epithelial-to-mesenchymal transition- and stem cell-like conversion. *Cancer Res*. **71**:3121-3131.

Alvarez, B. V., A. L. Quon, J. Mullen, and J. R. Casey. (2013) Quantification of carbonic anhydrase gene expression in ventricle of hypertrophic and failing human heart. *BMC. Cardiovasc. Disord*. **13**:2.

Ambler, C. A., J. L. Nowicki, A. C. Burke, and V. L. Bautch. (2001) Assembly of trunk and limb blood vessels involves extensive migration and vasculogenesis of somite-derived angioblasts. *Dev. Biol*. **234**:352-364.

Anggard, E. E. (1990) The endothelium--the body's largest endocrine gland? *J. Endocrinol*. **127**:371-375.

Aquila-Pastir, L. A., N. R. DiPaola, R. G. Matteo, N. G. Smedira, P. M. McCarthy, and C. S. Moravec. (2002) Quantitation and distribution of beta-tubulin in human cardiac myocytes. *J. Mol. Cell Cardiol*. **34**:1513-1523.

Arregui, C. O., A. Gonzalez, J. E. Burdisso, and A. E. Gonzalez Wusener. (2013) Protein tyrosine phosphatase PTP1B in cell adhesion and migration. *Cell Adh. Migr*. **7**:418-423.

Aveleira, C. l. A., C. M. Lin, S. F. Abcouwer, A. F. AmbrÃ³sio, and D. A. Antonetti. (2010) TNF-a Signals Through PKC/NF-kB to Alter the Tight Junction Complex and Increase Retinal Endothelial Cell Permeability. *Diabetes*. **59**:2872–2882.

Banquet, S., E. Gomez, L. Nicol, F. Edwards-Levy, J. P. Henry, R. Cao, D. Schapman, B. Dautreaux, F. Lallemand, F. Bauer, Y. Cao, C. Thuillez, P. Mulder, V. Richard, and E. Brakenhielm. (2011)

Arteriogenic therapy by intramyocardial sustained delivery of a novel growth factor combination prevents chronic heart failure. *Circulation*. **124**:1059-1069.

Barr, A. J. (2010) Protein tyrosine phosphatases as drug targets: strategies and challenges of inhibitor development. *Future. Med. Chem*. **2**:1563-1576.

Bence, K. K., M. Delibegovic, B. Xue, C. Z. Gorgun, G. S. Hotamisligil, B. G. Neel, and B. B. Kahn. (2006) Neuronal PTP1B regulates body weight, adiposity and leptin action. *Nat. Med*. **12**:917-924.

Besnier, M., A. Galaup, L. Nicol, J. P. Henry, D. Coquerel, A. Gueret, P. Mulder, E. Brakenhielm, C. Thuillez, S. Germain, V. Richard, and A. Ouvrard-Pascaud. (2014) Enhanced angiogenesis and increased cardiac perfusion after myocardial infarction in protein tyrosine phosphatase 1B-deficient mice. *FASEB J*. **28**:3351-3361.

Bid, H. K. and S. Kerk. (2016) BET bromodomain inhibitor (JQ1) and tumor angiogenesis. *Oncoscience*. **3**:316-317.

Bid, H. K., D. A. Phelps, L. Xaio, D. C. Guttridge, J. Lin, C. London, L. H. Baker, X. Mo, and P. J. Houghton. (2016) The Bromodomain BET Inhibitor JQ1 Suppresses Tumor Angiogenesis in Models of Childhood Sarcoma. *Mol. Cancer Ther*. **15**:1018-1028.

Bleakley, C., P. K. Hamilton, R. Pumb, M. Harbinson, and G. E. McVeigh. (2015) Endothelial Function in Hypertension: Victim or Culprit? *J. Clin Hypertens*. **17**:651-654.

Brown, J. D., C. Y. Lin, Q. Duan, G. Griffin, A. Federation, R. M. Paranal, S. Bair, G. Newton, A. Lichtman, A. Kung, T. Yang, H. Wang, F. W. Luscinskas, K. Croce, J. E. Bradner, and J. Plutzky. (2014) NF-kB directs dynamic super enhancer formation in inflammation and atherogenesis. *Mol. Cell*. **56**:219-231.

Bruder-Nascimento, T., B. R. Butler, D. J. Herren, M. W. Brands, K. K. Bence, and E. J. Belin de Chantemele. (2015) Deletion of protein tyrosine phosphatase 1b in proopiomelanocortin neurons reduces neurogenic control of blood pressure and protects mice from leptin- and sympatho-mediated hypertension. *Pharmacol. Res.* **102**:235-244.

Bugger, H., M. Schwarzer, D. Chen, A. Schrepper, P. A. Amorim, M. Schoepe, T. D. Nguyen, F. W. Mohr, O. Khalimonchuk, B. C. Weimer, and T. Doenst. (2010) Proteomic remodelling of mitochondrial oxidative pathways in pressure overload-induced heart failure. *Cardiovasc. Res*. **85**:376-384.

Callahan, M. K., K. A. Williams, P. Kivisakk, D. Pearce, M. F. Stins, and R. M. Ransohoff. (2004) CXCR3 marks CD4+ memory T lymphocytes that are competent to migrate across a human brain microvascular endothelial cell layer. *J. Neuroimmunol.* **153**:150-157.

Carmeliet, P. (2005) Angiogenesis in life, disease and medicine. Nature 438:932-936.

Carreno, J. E., F. Apablaza, M. P. Ocaranza, and J. E. Jalil. (2006) Cardiac hypertrophy: molecular and cellular events. Rev. *Esp. Cardiol*. **59**:473-486.

Chaturvedi, N. 2003. ETHNIC DIFFERENCES IN CARDIOVASCULAR DISEASE. *Heart*. **89**:681-686

Chen, W. Y., J. Hong, J. Gannon, R. Kakkar, and R. T. Lee. (2015) Myocardial pressure overload induces systemic inflammation through endothelial cell IL-33. *Proc. Natl. Acad. Sci. U. S. A* **112**:7249-7254.

Cheng, S., V. R. Fernandes, D. A. Bluemke, R. L. McClelland, R. A. Kronmal, and J. A. Lima. (2009) Age-related left ventricular remodeling and associated risk for cardiovascular outcomes: the Multi-Ethnic Study of Atherosclerosis. *Circ. Cardiovasc. Imaging* **2**:191-198.

Chiang, C. M. (2009) Brd4 engagement from chromatin targeting to transcriptional regulation: selective contact with acetylated histone H3 and H4. *F1000. Biol. Rep*. **1**:98.

Chien, S. (2008) Effects of disturbed flow on endothelial cells. *Ann. Biomed. Eng* **36**:554-562.

Chouchani, E. T., C. Methner, G. Buonincontri, C. H. Hu, A. Logan, S. J. Sawiak, M. P. Murphy, and T. Krieg. (2014) Complex I deficiency due to selective loss of Ndufs4 in the mouse heart results in severe hypertrophic cardiomyopathy. *PLoS. One*. **9**:e94157.

Conti, P. and Y. Shaik-Dasthagirisaeb. (2015) Atherosclerosis: a chronic inflammatory disease mediated by mast cells. *Cent. Eur. J. Immunol.* **40**:380-386.

Coquerel, D., R. Neviere, E. Delile, P. Mulder, X. Marechal, D. Montaigne, S. Renet, I. Remy-Jouet, E. Gomez, J. P. Henry, J. C. do Rego, V. Richard, and F. Tamion. (2014) Gene deletion of protein tyrosine phosphatase 1B protects against sepsis-induced cardiovascular dysfunction and mortality. Arterioscler. *Thromb. Vasc. Biol.* **34**:1032-1044.

Crawford, N. P., J. Alsarraj, L. Lukes, R. C. Walker, J. S. Officewala, H. H. Yang, M. P. Lee, K. Ozato, and K. W. Hunter. (2008) Bromodomain 4 activation predicts breast cancer survival. *Proc. Natl. Acad. Sci. U. S. A* **105**:6380-6385.

Crowe, B. L., R. C. Larue, C. Yuan, S. Hess, M. Kvaratskhelia, and M. P. Foster. (2016) Structure of the Brd4 ET domain bound to a C-terminal motif from gamma-retroviral integrases reveals a conserved mechanism of interaction. *Proc. Natl. Acad. Sci. U. S. A* **113**:2086-2091.

Dai, D. F., E. J. Hsieh, T. Chen, L. G. Menendez, N. B. Basisty, L. Tsai, R. P. Beyer, D. A. Crispin, N. J. Shulman, H. H. Szeto, R. Tian, M. J. MacCoss, and P. S. Rabinovitch. (2013) Global proteomics and pathway analysis of pressure-overload-induced heart failure and its attenuation by mitochondrial-targeted peptides. *Circ. Heart Fail*. **6**:1067-1076.

Dai, D. F., E. J. Hsieh, Y. Liu, T. Chen, R. P. Beyer, M. T. Chin, M. J. MacCoss, and P. S. Rabinovitch. (2012) Mitochondrial proteome remodelling in pressure overload-induced heart failure: the role of mitochondrial oxidative stress. *Cardiovasc. Res.* **93**:79-88.

Dart, A. M. and J. P. Chin-Dusting. (1999) Lipids and the endothelium. *Cardiovasc. Res*. **43**:308-322.

Deaton, C., E. S. Froelicher, L. H. Wu, C. Ho, K. Shishani, and T. Jaarsma. (2011) The global burden of cardiovascular disease. *Eur. J. Cardiovasc. Nurs. 10 Suppl* **2**:S5-13.

Devaiah, B. N., C. Case-Borden, A. Gegonne, C. H. Hsu, Q. Chen, D. Meerzaman, A. Dey, K. Ozato, and D. S. Singer. (2016) BRD4 is a histone acetyltransferase that evicts nucleosomes from chromatin. *Nat. Struct. Mol. Biol.* **23**:540-548.

Devaiah, B. N., B. A. Lewis, N. Cherman, M. C. Hewitt, B. K. Albrecht, P. G. Robey, K. Ozato, R. J. Sims, III, and D. S. Singer. (2012) BRD4 is an atypical kinase that phosphorylates serine2 of the RNA polymerase II carboxy-terminal domain. *Proc. Natl. Acad. Sci. U. S. A* **109**:6927-6932.

Dhingra, R. and R. S. Vasan. (2011) Age as a Cardiovascular Risk Factor. med clin north america. *Med Clin North Am.* **96**:87-91

Dickhout, J. G. and R. C. Austin. (2006) Proteasomal regulation of cardiac hypertrophy: is demolition necessary for building? *Circulation* **114**:1796-1798.

Dormond, O., A. Foletti, C. Paroz, and C. Ruegg. (2001) NSAIDs inhibit alpha V beta 3 integrin-mediated and Cdc42/Rac-dependent endothelial-cell spreading, migration and angiogenesis. *Nat. Med.* **7**:1041-1047.

Drugs.R.D. (2011) Rvx 208. *Drugs R. D.* **11**:207-213.

Elchebly, M., P. Payette, E. Michaliszyn, W. Cromlish, S. Collins, A. L. Loy, D. Normandin, A. Cheng, J. Himms-Hagen, C. C. Chan, C. Ramachandran, M. J. Gresser, M. L. Tremblay, and B. P. Kennedy. (1999) Increased insulin sensitivity and obesity resistance in mice lacking the protein tyrosine phosphatase-1B gene. *Science* **283**:1544-1548.

Eshkiki, Z. S., M. H. Ghahremani, P. Shabani, S. G. Firuzjaee, A. Sadeghi, H. Ghanbarian, and R. Meshkani. (2017) Protein tyrosine phosphatase 1B (PTP1B) is required for cardiac lineage differentiation of mouse embryonic stem cells. *Mol. Cell Biochem*. **425**:95-102.

Falk, E. (1992) Why do plaques rupture? Circulation 86:III30-III42.

Forouhi, N. G. and N. Sattar. (2006) CVD risk factors and ethnicity--a homogeneous relationship? *Atheroscler. Suppl* **7**:11-19.

Friedl, J., M. Puhlmann, D. L. Bartlett, S. K. Libutti, E. N. Turner, M. F. Gnant, and H. R. Alexander. (2002) Induction of permeability across endothelial cell monolayers by tumor necrosis factor (TNF) occurs via a tissue factor-dependent mechanism: relationship between the procoagulant and permeability effects of TNF. *Blood* **100**:1334-1339.

Geraghty, P., A. A. Hardigan, A. M. Wallace, O. Mirochnitchenko, J. Thankachen, L. Arellanos, V. Thompson, J. M. D'Armiento, and R. F. Foronjy. (2013) The glutathione peroxidase 1-protein tyrosine phosphatase 1B-protein phosphatase 2A axis. A key determinant of airway inflammation and alveolar destruction. *Am. J. Respir. Cell Mol. Biol.* **49**:721-730.

Gerhardt, T. and K. Ley. (2015) Monocyte trafficking across the vessel wall. *Cardiovasc. Res*. **107**:321-30

Ghosh, G. C., R. Bhadra, R. K. Ghosh, K. Banerjee, and A. Gupta. (2017) RVX 208: A novel BET protein inhibitor, role as an inducer of apo A-I/HDL and beyond. *Cardiovasc. Ther*. **35**. 1755.

Gilham, D., S. Wasiak, L. M. Tsujikawa, C. Halliday, K. Norek, R. G. Patel, E. Kulikowski, J. Johansson, M. Sweeney, and N. C. Wong. (2016) Corrigendum to "RVX-208, a BET-inhibitor for treating atherosclerotic cardiovascular disease, raises ApoA-I/HDL and represses pathways that contribute to cardiovascular disease". *Atherosclerosis* **253**:345.

Gogiraju, R., M. R. Schroeter, M. L. Bochenek, A. Hubert, T. Munzel, G. Hasenfuss, and K. Schafer. (2016) Endothelial Deletion of Protein Tyrosine Phosphatase-1B Protects Against Pressure Overload-Induced Heart Failure in Mice. *Cardiovasc. Res.* **111**: 204-16.

Gomez, E., M. Vercauteren, B. Kurtz, A. Ouvrard-Pascaud, P. Mulder, J. P. Henry, M. Besnier, A. Waget, H. R. Hooft Van, M. L. Tremblay, R. Burcelin, C. Thuillez, and V. Richard. (2012) Reduction of heart failure by pharmacological inhibition or gene deletion of protein tyrosine phosphatase 1B. *J. Mol. Cell Cardiol.* **52**:1257-1264.

Gupta, M. P. (2007) Factors controlling cardiac myosin-isoform shift during hypertrophy and heart failure. *J. Mol. Cell Cardiol*. **43**:388-403.

Hadi, H. A., C. S. Carr, and S. J. Al. (2005) Endothelial dysfunction: cardiovascular risk factors, therapy, and outcome. *Vasc. Health Risk Manag.* **1**:183-198.

Hajra, L., A. I. Evans, M. Chen, S. J. Hyduk, T. Collins, and M. I. Cybulsky. (2000) The NF-kappa B signal transduction pathway in aortic endothelial cells is primed for activation in regions predisposed to atherosclerotic lesion formation. *Proc. Natl. Acad. Sci. U. S. A* **97**:9052-9057.

Hara, H., N. Takeda, and I. Komuro. (2017) Pathophysiology and therapeutic potential of cardiac fibrosis. *Inflamm. Regen.* **37**:13.

Heineke, J. and J. D. Molkentin. (2006) Regulation of cardiac hypertrophy by intracellular signalling pathways. *Nat. Rev. Mol. Cell Biol*. **7**:589-600.

Herron, T. J., F. S. Korte, and K. S. McDonald. (2001) Loaded shortening and power output in cardiac myocytes are dependent on myosin heavy chain isoform expression. *Am. J. Physiol Heart Circ. Physiol* **281**:H1217-H1222.

Higashi, Y., Y. Kihara, and K. Noma. (2012) Endothelial dysfunction and hypertension in aging. *Hypertens. Res.* **35**:1039-1047.

Holderfield, M. T. and C. C. Hughes. (2008) Crosstalk between vascular endothelial growth factor, notch, and transforming growth factor-beta in vascular morphogenesis. *Circ. Res*. **102**:637-652.

Hu, Y., J. Zhou, F. Ye, H. Xiong, L. Peng, Z. Zheng, F. Xu, M. Cui, C. Wei, X. Wang, Z. Wang, H. Zhu, P. Lee, M. Zhou, B. Jiang, and D. Y. Zhang. (2015) BRD4 inhibitor inhibits colorectal cancer growth and metastasis. *Int. J. Mol. Sci*. **16**:1928-1948.

Huang, B., X. D. Yang, M. M. Zhou, K. Ozato, and L. F. Chen. (2009) Brd4 coactivates transcriptional activation of NF-kappaB via specific binding to acetylated RelA. *Mol. Cell Biol*. **29**:1375-1387.

Huang, M., Q. Qiu, Y. Xiao, S. Zeng, M. Zhan, M. Shi, Y. Zou, Y. Ye, L. Liang, X. Yang, and H. Xu. (2016) BET Bromodomain Suppression Inhibits VEGF-induced Angiogenesis and Vascular Permeability by Blocking VEGFR2-mediated Activation of PAK1 and eNOS. *Sci. Rep.* **6**:23770.

Huang, M., S. Zeng, Y. Zou, M. Shi, Q. Qiu, Y. Xiao, G. Chen, X. Yang, L. Liang, and H. Xu. (2017) The suppression of bromodomain and extra-terminal domain inhibits vascular inflammation by blocking NF-kappaB and MAPK activation. *Br. J. Pharmacol*. **174**:101-115.

Hudson, B., C. Hidalgo, C. Saripalli, and H. Granzier. (2011) Hyperphosphorylation of mouse cardiac titin contributes to transverse aortic constriction-induced diastolic dysfunction. *Circ. Res*. **109**:858-866.

Hueso, L., C. Rios-Navarro, A. Ruiz-Sauri, F. J. Chorro, J. Nunez, M. J. Sanz, V. Bodi, and L. Piqueras. (2017) Dynamics and implications of circulating anti-angiogenic VEGF-A165b isoform in patients with ST-elevation myocardial infarction. *Sci. Rep.* **7**:9962.

Huq, Michiko Moriyama, and Pradeep Kumar Ray. (2018) Risk Factors for Development of Cardiovascular Disease. Asian Hosptal and Health care management report https://www.asianhhm.com/medical-sciences/risk-factors-development-cardiovascular-disease.

Imes, C. C. and F. M. Lewis. (2014) Family history of cardiovascular disease (CVD), perceived CVD risk, and health-related behavior: A review of the literature. *J. Cardiovasc. Nurs.* **29**:108-29.

Isogai, C., W. E. Laug, H. Shimada, P. J. Declerck, M. F. Stins, D. L. Durden, A. Erdreich-Epstein, and Y. A. DeClerck. (2001) Plasminogen activator inhibitor-1 promotes angiogenesis by stimulating endothelial cell migration toward fibronectin. *Cancer Res*. **61**:5587-5594.

Jeon, Y. M., S. Lee, S. Kim, Y. Kwon, K. Kim, C. G. Chung, S. Lee, S. B. Lee, and H. J. Kim. (2017) Neuroprotective Effects of Protein Tyrosine Phosphatase 1B Inhibition against ER Stress-Induced Toxicity. *Mol. Cells* **40**:280-290.

Ji, K. T., L. Qian, J. L. Nan, Y. J. Xue, S. Q. Zhang, G. Q. Wang, R. P. Yin, Y. J. Zhu, L. P. Wang, J. Ma, L. M. Liao, and J. F. Tang. (2015) Ox-LDL induces dysfunction of endothelial progenitor cells via activation of NF-kappaB. *Biomed. Res. Int*. **2015:**175291.

Jiao, H., Y. Zhang, Z. Yan, Z. G. Wang, G. Liu, R. D. Minshall, A. B. Malik, and G. Hu. (2013) Caveolin-1 Tyr14 phosphorylation induces interaction with TLR4 in endothelial cells and mediates MyD88-dependent signaling and sepsis-induced lung inflammation. *J. Immunol*. **191**:6191-6199.

Jing, L., C. M. Binkley, J. D. Suever, N. Umasankar, C. M. Haggerty, J. Rich, G. J. Wehner, S. M. Hamlet, D. K. Powell, A. Radulescu, H. L. Kirchner, F. H. Epstein, and B. K. Fornwalt. (2016) Cardiac remodeling and dysfunction in childhood obesity: a cardiovascular magnetic resonance study. *J. Cardiovasc. Magn Reson*. **18**:28.

Kachur, S., C. J. Lavie, S. A. de, R. V. Milani, and H. O. Ventura. (2017) Obesity and cardiovascular diseases. *Minerva Med*. **108**:212-228.

Kadomatsu, K., P. Bencsik, A. Gorbe, C. Csonka, K. Sakamoto, S. Kishida, and P. Ferdinandy. (2014) Therapeutic potential of midkine in cardiovascular disease. *Br. J. Pharmacol*. **171**:936-944.

Kalogeris, T. J., C. Baines, and R. J. Korthuis. (2014) Adenosine prevents TNFalpha-induced decrease in endothelial mitochondrial mass via activation of eNOS-PGC-1alpha regulatory axis. *PLoS. One*. **9**:e98459.

Kathiresan, S. and D. Srivastava. (2012) Genetics of Human Cardiovascular Disease. *Cell*. **148**:1242-57.

Kazakoff, P. W., T. R. McGuire, E. B. Hoie, M. Cano, and P. L. Iversen. (1995) An in vitro model for endothelial permeability: assessment of monolayer integrity. *In Vitro Cell Dev. Biol. Anim*. **31**:846-852.

Kempen, H. J., D. Bellus, O. Fedorov, S. Nicklisch, P. Filippakopoulos, S. Picaud, and S. Knapp. (2013) Stimulation of Hepatic Apolipoprotein A-I Production by Novel Thieno-Triazolodiazepines: Roles of the Classical Benzodiazepine Receptor, PAF Receptor, and Bromodomain Binding. *Lipid Insights*. **6**:47-54.

Khan, N., L. Binder, D. V. K. Pantakani, and A. R. Asif. (2017) MPA Modulates Tight Junctions' Permeability via Midkine/PI3K Pathway in Caco-2 Cells: A Possible Mechanism of Leak-Flux Diarrhea in Organ Transplanted Patients. *Front Physiol* **8**:438.

Khan, N., C. Lenz, L. Binder, D. V. Pantakani, and A. R. Asif. (2016) Active and Repressive Chromatin-Associated Proteome after MPA Treatment and the Role of Midkine in Epithelial Monolayer Permeability. *Int. J. Mol. Sci.* **17**: E597

Kim, J., M. Montagnani, S. Chandrasekran, and M. J. Quon. (2012) Role of Lipotoxity in Endothelial Dysfunction. *Heart Fail. Clin*. **8**: 589–607.

Kobayashi, K., K. Maeda, M. Takefuji, R. Kikuchi, Y. Morishita, M. Hirashima, and T. Murohara. (2017) Dynamics of angiogenesis in ischemic areas of the infarcted heart. *Sci. Rep*. **7**:7156.

Kolber, M. R. and C. Scrimshaw. (2014) Family history of cardiovascular disease. *Can. Fam. Physcian*. **60**(11): 1016.

Kritchevsky, S. B., M. Cesari, and M. Pahor. (2005) Inflammatory markers and cardiovascular health in older adults. *Cardiovasc. Res*. **66**:265-275.

Kurtenbach, S., S. Kurtenbach, and G. Zoidl. (2014) Gap junction modulation and its implications for heart function. *Front Physiol* **5**:82.

Kwak, B. R., M. Back, M. L. Bochaton-Piallat, G. Caligiuri, M. J. Daemen, P. F. Davies, I. E. Hoefer, P. Holvoet, H. Jo, R. Krams, S. Lehoux, C. Monaco, S. Steffens, R. Virmani, C. Weber, J. J. Wentzel, and

P. C. Evans. (2014) Biomechanical factors in atherosclerosis: mechanisms and clinical implications. *Eur. Heart J*. **35**:3013-3020d.

Lamalice, L., B. F. Le, and J. Huot. (2007) Endothelial cell migration during angiogenesis. *Circ. Res*. **100**:782-794.

Lanahan, A. A., D. Lech, A. Dubrac, J. Zhang, Z. W. Zhuang, A. Eichmann, and M. Simons. (2014) PTP1b is a physiologic regulator of vascular endothelial growth factor signaling in endothelial cells. *Circulation* **130**:902-909.

Lau, E., Q. Cao, M. P. Y. Lam, J. Wang, D. C. M. Ng, B. J. Bleakley, J. M. Lee, D. A. Liem, D. Wang, H. Hermjakob, and P. Ping. (2018) Integrated omics dissection of proteome dynamics during cardiac remodeling. *Nat. Commun.* **9**:120.

Lee, D., A. Kraus, D. Prins, J. Groenendyk, I. Aubry, W. X. Liu, H. D. Li, O. Julien, N. Touret, B. D. Sykes, M. L. Tremblay, and M. Michalak. (2015) UBC9-dependent association between calnexin and protein tyrosine phosphatase 1B (PTP1B) at the endoplasmic reticulum. *J. Biol. Chem*. **290**:5725-5738.

Leon, B. M. and T. M. Maddox. (2015) Diabetes and cardiovascular disease: Epidemiology, biological mechanisms, treatment recommendations and future research. *World Journal Diabetes.* **13**: 1246-58

Leon, I. R., V. Schwammle, O. N. Jensen, and R. R. Sprenger. (2013) Quantitative assessment of in-solution digestion efficiency identifies optimal protocols for unbiased protein analysis. *Mol. Cell Proteomics.* **12**:2992-3005.

Libby, P. (2000) Changing concepts of atherogenesis. *J. Intern. Med.* **247**:349-358.

Lovren, F., H. Teoh, and S. Verma. (2015) Obesity and atherosclerosis: mechanistic insights. *Can. J. Cardiol.* **31**:177-183.

Low, J. L., C. L. Chai, and S. Q. Yao. (2014) Bidentate inhibitors of protein tyrosine phosphatases. Antioxid. *Redox. Signal*. **20**:2225-2250.

Lu, H., P. W. Fedak, X. Dai, C. Du, Y. Q. Zhou, M. Henkelman, P. S. Mongroo, A. Lau, H. Yamabi, A. Hinek, M. Husain, G. Hannigan, and J. G. Coles. (2006) Integrin-linked kinase expression is elevated in human cardiac hypertrophy and induces hypertrophy in transgenic mice. *Circulation* **114**:2271-2279.

Lu, P., Y. Shen, H. Yang, Y. Wang, Z. Jiang, X. Yang, Y. Zhong, H. Pan, J. Xu, H. Lu, and H. Zhu. (2017) BET inhibitors RVX-208 and PFI-1 reactivate HIV-1 from latency. *Sci. Rep.* **7**:16646.

Mahdavi, V., A. P. Chambers, and B. Nadal-Ginard. (1984) Cardiac alpha- and beta-myosin heavy chain genes are organized in tandem. *Proc. Natl. Acad. Sci. U. S. A* **81**:2626-2630.

Man, S., E. E. Ubogu, K. A. Williams, B. Tucky, M. K. Callahan, and R. M. Ransohoff. (2008) Human brain microvascular endothelial cells and umbilical vein endothelial cells differentially facilitate

leukocyte recruitment and utilize chemokines for T cell migration. *Clin Dev. Immunol*. **2008**:384982.

Manabe, I., T. Shindo, and R. Nagai. (2002) Gene expression in fibroblasts and fibrosis: involvement in cardiac hypertrophy. *Circ. Res.* **91**:1103-1113.

Manning, G., D. B. Whyte, R. Martinez, T. Hunter, and S. Sudarsanam. (2002) The protein kinase complement of the human genome. *Science* **298**:1912-1934.

Matz, R. L. and R. Andriantsitohaina. (2003) Age-related endothelial dysfunction : potential implications for pharmacotherapy. *Drugs Aging* **20**:527-550.

McGrath, M. J., D. L. Cottle, M. A. Nguyen, J. M. Dyson, I. D. Coghill, P. A. Robinson, M. Holdsworth, B. S. Cowling, E. C. Hardeman, C. A. Mitchell, and S. Brown. (2006) Four and a half LIM protein 1 binds myosin-binding protein C and regulates myosin filament formation and sarcomere assembly. *J. Biol. Chem*. **281**:7666-7683.

McLure, K. G., E. M. Gesner, L. Tsujikawa, O. A. Kharenko, S. Attwell, E. Campeau, S. Wasiak, A. Stein, A. White, E. Fontano, R. K. Suto, N. C. Wong, G. S. Wagner, H. C. Hansen, and P. R. Young. (2013) RVX-208, an inducer of ApoA-I in humans, is a BET bromodomain antagonist. *PLoS. One.* **8**:e83190.

Messner, B. and D. Bernhard. (2014) Smoking and cardiovascular disease: mechanisms of endothelial dysfunction and early atherogenesis. *Arterioscler. Thromb. Vasc. Biol*. **34**:509-515.

Michael Pittilo, R. (2000) Cigarette smoking, endothelial injury and cardiovascular disease. *int. J. Exp. Pathol.* **4**:219-230

Michaelis, U. R. (2014) Mechanisms of endothelial cell migration. *Cell Mol. Life Sci*. **71**:4131-4148.

Mobasher, M. A., A. Gonzalez-Rodriguez, B. Santamaria, S. Ramos, M. A. Martin, L. Goya, P. Rada, L. Letzig, L. P. James, A. Cuadrado, J. Martin-Perez, K. J. Simpson, J. Muntane, and A. M. Valverde. (2013) Protein tyrosine phosphatase 1B modulates GSK3beta/Nrf2 and IGFIR signaling pathways in acetaminophen-induced hepatotoxicity. *Cell Death. Dis*. **4**:e626.

Moens, A. L., E. Takimoto, C. G. Tocchetti, K. Chakir, D. Bedja, G. Cormaci, E. A. Ketner, M. Majmudar, K. Gabrielson, M. K. Halushka, J. B. Mitchell, S. Biswal, K. M. Channon, M. S. Wolin, N. J. Alp, N. Paolocci, H. C. Champion, and D. A. Kass. (2008) Reversal of cardiac hypertrophy and fibrosis from pressure overload by tetrahydrobiopterin: efficacy of recoupling nitric oxide synthase as a therapeutic strategy. *Circulation*. **117**:2626-2636.

Monaco, C. and E. Paleolog. (2004) Nuclear factor kappaB: a potential therapeutic target in atherosclerosis and thrombosis. *Cardiovasc. Res.* **61**:671-682.

Montecucco, F., V. Braunersreuther, G. L. Viviani, S. Ã. Lenglet, and F. o. Mach. (2012) Update on the Pathophysiological Role of Intracellular Signaling Pathways in Atherosclerotic Plaques and Ischemic Myocardium. *Current Signal Transduction Therapy*. **2**:104-110.

Mottonen, M. J., O. Ukkola, J. Lumme, Y. A. Kesaniemi, H. V. Huikuri, and J. S. Perkiomaki. (2017) Cardiac Remodeling from Middle Age to Senescence. *Front Physiol* **8**:341.

Najafova, Z., R. Tirado-Magallanes, M. Subramaniam, T. Hossan, G. Schmidt, S. Nagarajan, S. J. Baumgart, V. K. Mishra, U. Bedi, E. Hesse, S. Knapp, J. R. Hawse, and S. A. Johnsen. (2017) BRD4 localization to lineage-specific enhancers is associated with a distinct transcription factor repertoire. *Nucleic Acids Res.* **45**:127-141.

Nakamura, Y., N. Patrushev, H. Inomata, D. Mehta, N. Urao, H. W. Kim, M. Razvi, V. Kini, K. Mahadev, B. J. Goldstein, R. McKinney, T. Fukai, and M. Ushio-Fukai. (2008) Role of protein tyrosine phosphatase 1B in vascular endothelial growth factor signaling and cell-cell adhesions in endothelial cells. *Circ. Res.* **102**:1182-1191.

Narishige, T., K. L. Blade, Y. Ishibashi, T. Nagai, M. Hamawaki, D. R. Menick, D. Kuppuswamy, and G. Cooper. (1999) Cardiac hypertrophic and developmental regulation of the beta-tubulin multigene family. *J. Biol. Chem.* **274**:9692-9697.

Nicoletti, A. and J. B. Michel. (1999) Cardiac fibrosis and inflammation: interaction with hemodynamic and hormonal factors. *Cardiovasc. Res.* **41**:532-543.

Nikolic, D., M. Rizzo, D. P. Mikhailidis, N. C. Wong, and M. Banach. (2015) An evaluation of RVX-208 for the treatment of atherosclerosis. *Expert. Opin. Investig. Drugs* **24**:1389-1398.

Panzhinskiy, E., J. Ren, and S. Nair. (2013) Protein tyrosine phosphatase 1B and insulin resistance: role of endoplasmic reticulum stress/reactive oxygen species/nuclear factor kappa B axis. *PLoS. One*. **8**:e77228.

Picaud, S., C. Wells, I. Felletar, D. Brotherton, S. Martin, P. Savitsky, B. Diez-Dacal, M. Philpott, C. Bountra, H. Lingard, O. Fedorov, S. Müller, P. E. Brennan, S. Knapp, and P. Filippakopoulos. (2013) RVX-208, an inhibitor of BET transcriptional regulators with selectivity for the second bromodomain. *Proc. Natl. Acad. Sci. U. S. A.* **49**: 19754-9

Ramji, D. P. and T. S. Davies. (2015) Cytokines in atherosclerosis: Key players in all stages of disease and promising therapeutic targets. *Cytokine Growth Factor Rev.* **26**:673-685.

Rio, D. C., M. Ares, Jr., G. J. Hannon, and T. W. Nilsen. (2010) Purification of RNA using TRIzol (TRI reagent). *Cold Spring Harb. Protoc.* **6**:prot5439.

Rosca, M. G. and C. L. Hoppel. (2013) Mitochondrial dysfunction in heart failure. *Heart Fail. Rev.* **18**:607-622.

Rosca, M. G., B. Tandler, and C. L. Hoppel. (2013) Mitochondria in cardiac hypertrophy and heart failure. *J. Mol. Cell Cardiol.* **55**:31-41.

Rosiek, A. and K. Leksowski. (2016) The risk factors and prevention of cardiovascular disease: the importance of electrocardiogram in the diagnosis and treatment of acute coronary syndrome. *Ther. Clin. Risk Manag.* **12**:1223-1229.

Royall, J. A., R. L. Berkow, J. S. Beckman, M. K. Cunningham, S. Matalon, and B. A. Freeman. (1989) Tumor necrosis factor and interleukin 1 alpha increase vascular endothelial permeability. *Am. J. Physiol* **257**:L399-L410.

Salaru, D., C. Arsenescu-Georgescu, Z. Halloul, M. Damerau, C. Albert, and P. R. Mertens. (2013) Expression of midkine, a multifunctional cytokine, in human atherosclerotic plaques. *European Journal of Internal Medicine*. **24**: e38.

Salaru, D. L., C. Arsenescu-Georgescu, C. Chatzikyrkou, J. Karagiannis, A. Fischer, and P. R. Mertens. (2016) Midkine, a heparin-binding growth factor, and its roles in atherogenesis and inflammatory kidney diseases. *Nephrol. Dial. Transplant.* **31**:1781-1787.

Samak, M., J. Fatullayev, A. Sabashnikov, M. Zeriouh, B. Schmack, M. Farag, A. F. Popov, P. M. Dohmen, Y. H. Choi, T. Wahlers, and A. Weymann. (2016) Cardiac Hypertrophy: An Introduction to Molecular and Cellular Basis. *Med Sci. Monit. Basic Res*. **22**:75-79.

Schmittgen, T. D. and K. J. Livak. (2008) Analyzing real-time PCR data by the comparative C(T) method. *Nat. Protoc.* **3**:1101-1108.

Sessa, W. C. (2004) eNOS at a glance. *J. Cell Sci.* **117**:2427-2429.

Shimizu, I. and T. Minamino. (2016) Physiological and pathological cardiac hypertrophy. *J. Mol. Cell Cardiol.* **97**:245-262.

Souders, C. A., T. K. Borg, I. Banerjee, and T. A. Baudino. (2012) Pressure overload induces early morphological changes in the heart. *Am. J. Pathol.* **181**:1226-1235.

Srinivasan, B., A. R. Kolli, M. B. Esch, H. E. Abaci, M. L. Shuler, and J. J. Hickman. (2015) TEER measurement techniques for in vitro barrier model systems. *J. Lab Autom*. **20**:107-126.

Stewart, J., G. Manmathan, and P. Wilkinson. (2017) Primary prevention of cardiovascular disease: A review of contemporary guidance and literature. *JRSM. Cardiovasc. Dis*. **6**:2048004016687211.

Strait, J. B. and E. G. Lakatta. (2012) Aging-associated cardiovascular changes and their relationship to heart failure. *Heart Fail. Clin.* **8**:143-164.

Stratton, M. S., S. M. Haldar, and T. A. McKinsey. (2017) BRD4 inhibition for the treatment of pathological organ fibrosis. *F1000Res*. **6**:1015

Sumi, T., K. Matsumoto, Y. Takai, and T. Nakamura. (1999) Cofilin phosphorylation and actin cytoskeletal dynamics regulated by rho- and Cdc42-activated LIM-kinase 2. *J. Cell Biol.* **147**:1519-1532.

Sumi-Ichinose, C., Y. Suganuma, T. Kano, N. Ihira, H. Nomura, K. Ikemoto, T. Hata, S. Katoh, H. Ichinose, and K. Kondo. (2017) Sepiapterin reductase gene-disrupted mice suffer from hypertension with fluctuation and bradycardia. *Physiol Rep.* **6:** e13196

Tagawa, H., N. Wang, T. Narishige, D. E. Ingber, M. R. Zile, and G. Cooper. (1997) Cytoskeletal mechanics in pressure-overload cardiac hypertrophy. *Circ. Res.* **80**:281-289.

Tak, P. P. and G. S. Firestein. (2001) NF-kappaB: a key role in inflammatory diseases. *J. Clin. Invest* **107**:7-11.

Talman, V. and H. Ruskoaho. (2016) Cardiac fibrosis in myocardial infarction-from repair and remodeling to regeneration. *Cell Tissue Res.* **365**:563-581.

Tamrakar, A. K., C. K. Maurya, and A. K. Rai. (2014) PTP1B inhibitors for type 2 diabetes treatment: a patent review. *Expert. Opin. Ther.* Pat **24**:1101-1115.

Tanaka, T. and M. Iino. (2016) Nuclear Translocation of p65 is Controlled by Sec6 via the Degradation of IkappaBalpha. *J. Cell Physiol* **231**:719-730.

Tardiff, J. C. (2006) Cardiac hypertrophy: stressing out the heart. J. Clin Invest 116:1467-1470.

Thiebaut, P. A., M. Besnier, E. Gomez, and V. Richard. (2016) Role of protein tyrosine phosphatase 1B in cardiovascular diseases. *J. Mol. Cell Cardiol*. **101**:50-57.

Thompson, D., N. Morrice, L. Grant, S. S. Le, K. Ziegler, P. Whitfield, N. Mody, H. M. Wilson, and M. Delibegovic. (2017) Myeloid protein tyrosine phosphatase 1B (PTP1B) deficiency protects against atherosclerotic plaque formation in the ApoE(-/-) mouse model of atherosclerosis with alterations in IL10/AMPKalpha pathway. *Mol. Metab* **6**:845-853.

Tian, J., X. An, and L. Niu. (2017) Myocardial fibrosis in congenital and pediatric heart disease. *Exp. Ther. Med* **13**:1660-1664.

Toischer, K., A. G. Rokita, B. Unsold, W. Zhu, G. Kararigas, S. Sossalla, S. P. Reuter, A. Becker, N. Teucher, T. Seidler, C. Grebe, L. Preuss, S. N. Gupta, K. Schmidt, S. E. Lehnart, M. Kruger, W. A. Linke, J. Backs, V. Regitz-Zagrosek, K. Schafer, L. J. Field, L. S. Maier, and G. Hasenfuss. (2010) Differential cardiac remodeling in preload versus afterload. *Circulation* **122**:993-1003.

Tonks, N. K., C. D. Diltz, and E. H. Fischer. (1988) Purification of the major protein-tyrosine-phosphatases of human placenta. *J. Biol. Chem.* **263**:6722-6730.

Travers, J. G., F. A. Kamal, J. Robbins, K. E. Yutzey, and B. C. Blaxall. (2016) Cardiac Fibrosis: The Fibroblast Awakens. *Circ. Res.* **118**:1021-1040.

Vasquez-Trincado, C., I. Garcia-Carvajal, C. Pennanen, V. Parra, J. A. Hill, B. A. Rothermel, and S. Lavandero. (2016) Mitochondrial dynamics, mitophagy and cardiovascular disease. *J. Physiol* **594**:509-525.

Verstraete, M. (1990) Coronary atherosclerosis and thrombosis. *Recenti Prog. Med* **81**:221-227.

Vidler, L. R., P. Filippakopoulos, O. Fedorov, S. Picaud, S. Martin, M. Tomsett, H. Woodward, N. Brown, S. Knapp, and S. Hoelder. (2013) Discovery of novel small-molecule inhibitors of BRD4 using structure-based virtual screening. *J. Med. Chem.* **56**:8073-8088.

von der Thusen, J. H., J. Kuiper, T. J. van Berkel, and E. A. Biessen. (2003) Interleukins in atherosclerosis: molecular pathways and therapeutic potential. *Pharmacol. Rev.* **55**:133-166.

Voorhees, R. M., I. S. Fernandez, S. H. Scheres, and R. S. Hegde. (2014) Structure of the mammalian ribosome-Sec61 complex to 3.4 A resolution. *Cell* **157**:1632-1643.

Wadhwa, E. and T. Nicolaides. (2016) Bromodomain Inhibitor Review: Bromodomain and Extra-terminal Family Protein Inhibitors as a Potential New Therapy in Central Nervous System Tumors. *cureus.* **8(5)**:e620

Wang, L., X. Wu, P. Huang, Z. Lv, Y. Qi, X. Wei, P. Yang, and F. Zhang. (2016) JQ1, a small molecule inhibitor of BRD4, suppresses cell growth and invasion in oral squamous cell carcinoma. *Oncol. Rep.* **36**:1989-1996.

Wang, Y., F. Yan, W. Zhang, S. Pang, and F. Jiang. (2018) Inhibiting Protein Tyrosine Phosphatase 1B to Improve Regenerative Functions of Endothelial Cells. *J. Cardiovasc. Pharmacol.* **71**:59-64.

Wang, Z. and T. Nakayama. (2010) Inflammation, a link between obesity and cardiovascular disease. *Mediators. Inflamm.* **2010**:535918.

Wasiak, S., D. Gilham, L. M. Tsujikawa, C. Halliday, K. Norek, R. G. Patel, K. G. McLure, P. R. Young, A. Gordon, E. Kulikowski, J. Johansson, M. Sweeney, and N. C. Wong. (2016) Data on gene and protein expression changes induced by apabetalone (RVX-208) in ex vivo treated human whole blood and primary hepatocytes. *Data Brief.* **8**:1280-1288.

Wende, A. R., J. Kim, W. L. Holland, B. E. Wayment, B. T. O'Neill, J. Tuinei, M. K. Brahma, M. E. Pepin, M. A. McCrory, I. Luptak, G. V. Halade, S. E. Litwin, and E. D. Abel. (2017) Glucose transporter 4-deficient hearts develop maladaptive hypertrophy in response to physiological or pathological stresses. Am. J. Physiol Heart Circ. Physiol **313**:H1098-H1108.

Wong, F., C. Hull, R. Zhande, J. Law, and A. Karsan. (2004) Lipopolysaccharide initiates a TRAF6-mediated endothelial survival signal. *Blood* **103**:4520-4526.

Xiao, L., Y. Liu, and N. Wang. (2014) New paradigms in inflammatory signaling in vascular endothelial cells. *Am. J. Physiol Heart Circ. Physiol* **306**:H317-H325.

Xu, Y. and C. R. Vakoc. (2014) Brd4 is on the move during inflammation. *Trends cell biol.* **24**:615-616.

Yip, S. C., S. Saha, and J. Chernoff. (2010) PTP1B: a double agent in metabolism and oncogenesis. *Trends Biochem. Sci.* **35**:442-449.

Zabolotny, J. M., Y. B. Kim, L. A. Welsh, E. E. Kershaw, B. G. Neel, and B. B. Kahn. (2008) Protein-tyrosine phosphatase 1B expression is induced by inflammation in vivo. *J. Biol. Chem.* **283**:14230-14241.

Zampetaki, A., L. Zeng, A. Margariti, Q. Xiao, H. Li, Z. Zhang, A. E. Pepe, G. Wang, O. Habi, E. deFalco, G. Cockerill, J. C. Mason, Y. Hu, and Q. Xu. (2010) Histone deacetylase 3 is critical in endothelial survival and atherosclerosis development in response to disturbed flow. *Circulation* **121**:132-142.

Zengerle, M., K. H. Chan, and A. Ciulli. (2015) Selective Small Molecule Induced Degradation of the BET Bromodomain Protein BRD4. *ACS Chem. Biol.* **10**:1770-1777.

Zhang, H., Y. Park, J. Wu, X. Chen, S. Lee, J. Yang, K. C. Dellsperger, and C. Zhang. (2009) Role of TNF-alpha in vascular dysfunction. *Clin Sci.* **116**:219-230.

7. Supplementary material

Supplementary figure. S1: STRING cluster analysis
A: WT-SHAM vs KO-SHAM up-regulated protein cluster
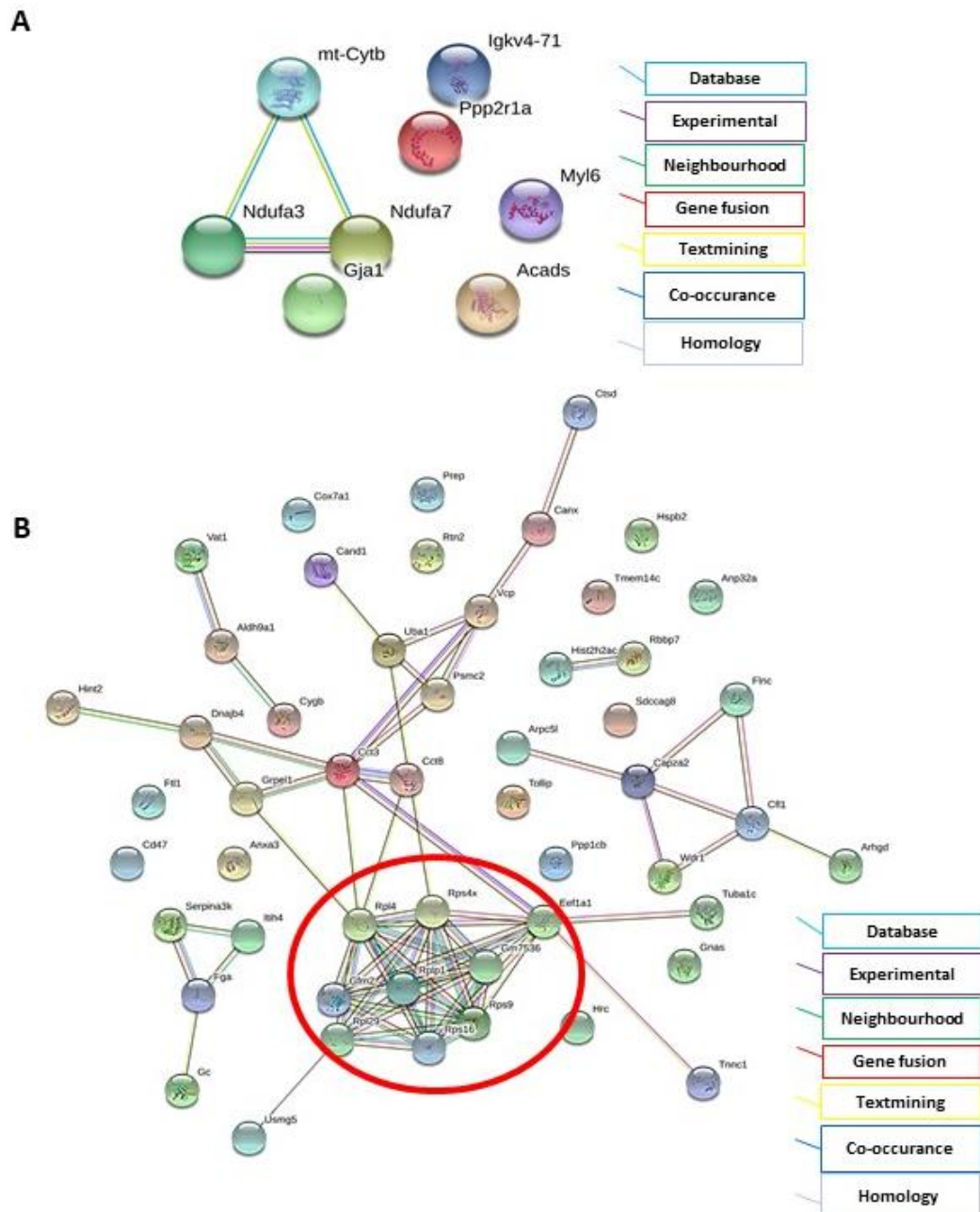B: WT-SHAM vs KO-SHAM down-regulated protein cluster

Fig. S1. Full view of STRING analysis of Group A, WT-SHAM vs KO-SHAM proteome. Analysis of protein interaction network by STRING, Coloured lines between the proteins indicate the protein co-occurrence, co-expression, known interactions and predicted interactions. Up-regulated proteins do not present any specific interaction or cluster (**A**) however Interconnecting ribosomal proteins (red circle) represents a functionally associated protein cluster in down-regulated proteins (**B).**

Supplementary figure. S2: STRING cluster analysis
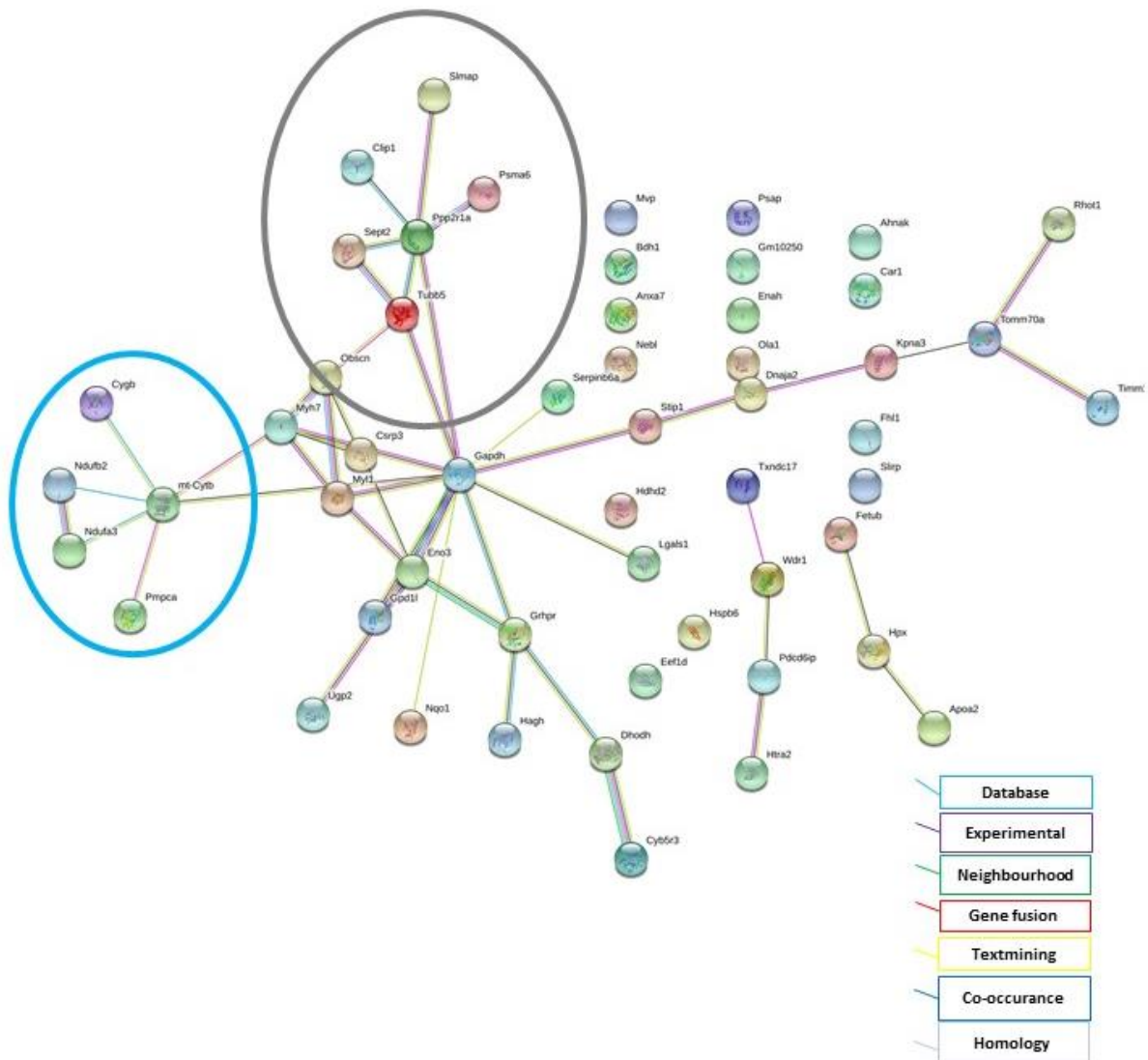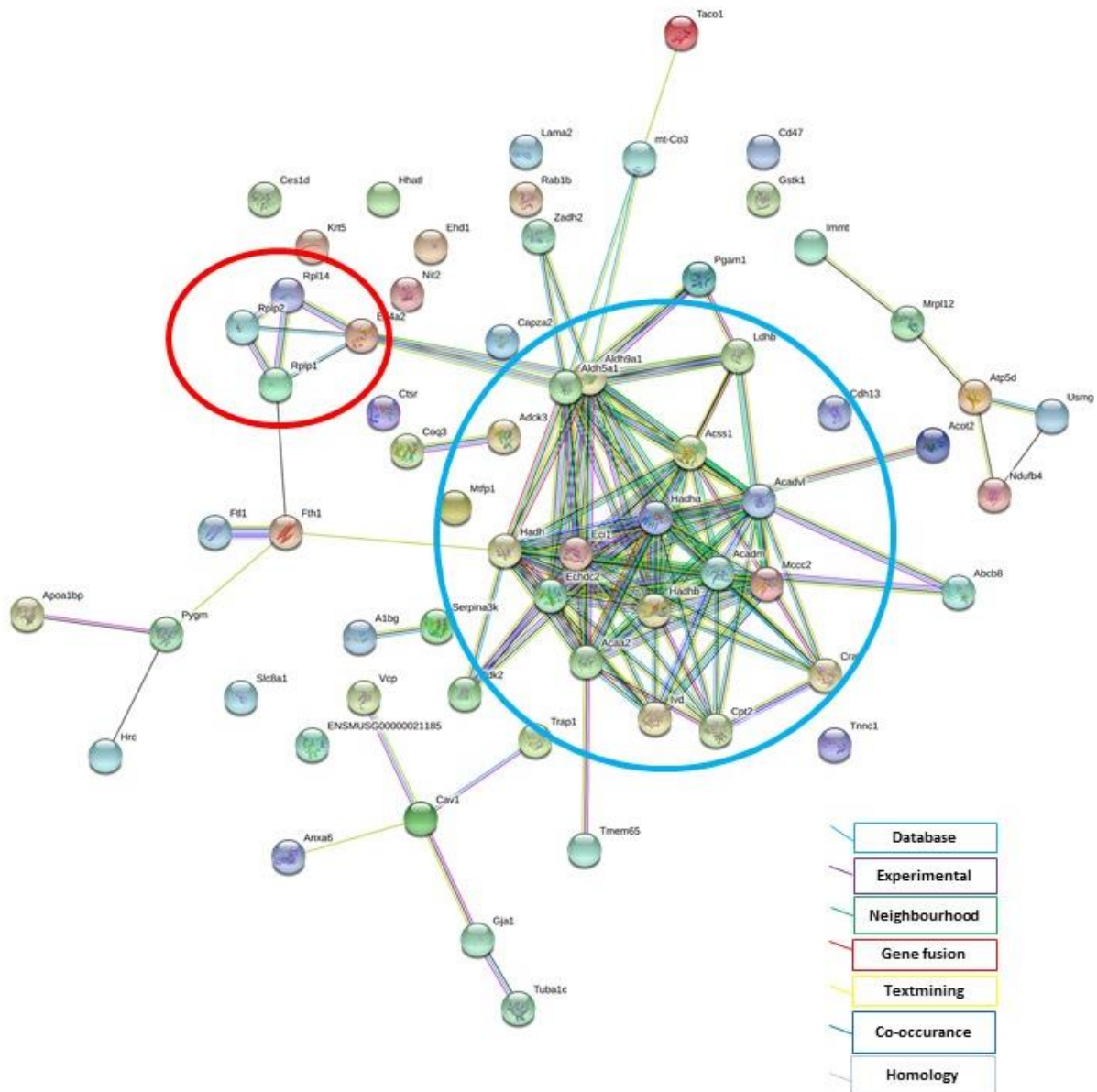WT-SHAM vs WT-TAC up-regulated protein cluster

Fig. S2. Full view of STRING analysis of Group B, WT-SHAM vs WT-TAC proteome (up-regulated). Analysis of protein interaction network by STRING, Coloured lines between the proteins indicate the protein co-occurrence, co-expression, known interactions and predicted interactions. Up-regulated proteins show interconnecting mitochondrial proteins (blue circle) represents a functionally associated protein cluster, while cytoskeleton associated proteins are showing another cluster (grey circle) in up-regulated proteins.

Supplementary figure. S3: STRING cluster analysis
WT-SHAM vs WT-TAC down-regulated protein cluster

Fig. S3. Full view of STRING analysis of Group B, WT-SHAM vs WT-TAC proteome (down-regulated). Analysis of protein interaction network by STRING, Coloured lines between the proteins indicate the protein co-occurrence, co-expression, known interactions and predicted interactions. Interconnecting mitochondrial proteins (blue circle) represents a functionally associated protein cluster, while ribosomal associated proteins are showing another cluster (red circle) in down-regulated proteins.

Supplementary figure. S4: STRING cluster analysis
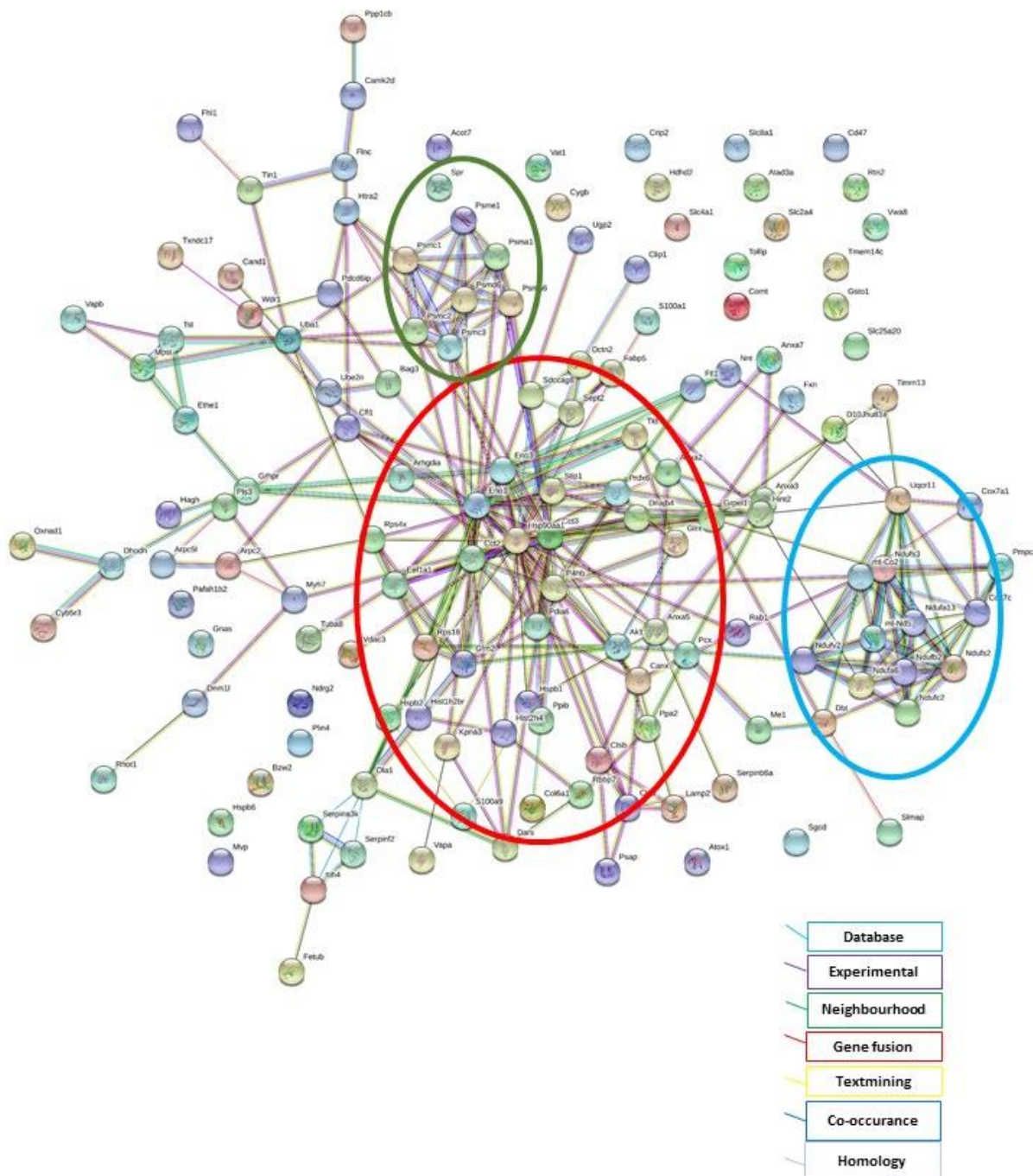KO-SHAM vs KO-TAC up-regulated protein cluster

Fig. S4. Full view of STRING analysis of Group C, KO-SHAM vs KO-TAC proteome (up-regulated). Analysis of protein interaction network by STRING, Coloured lines between the proteins indicate the protein co-occurrence, co-expression, known interactions and predicted interactions. Up-regulated proteins show interconnecting major cluster (red circle) represents multiple enzymes involved in metabolic pathways and cytoskeleton associated proteins while, mitochondrial proteins (blue circle) represents a functionally associated protein cluster, while proteasome associated proteins are showing another cluster (green circle).

Supplementary figure. S5. STRING cluster analysis
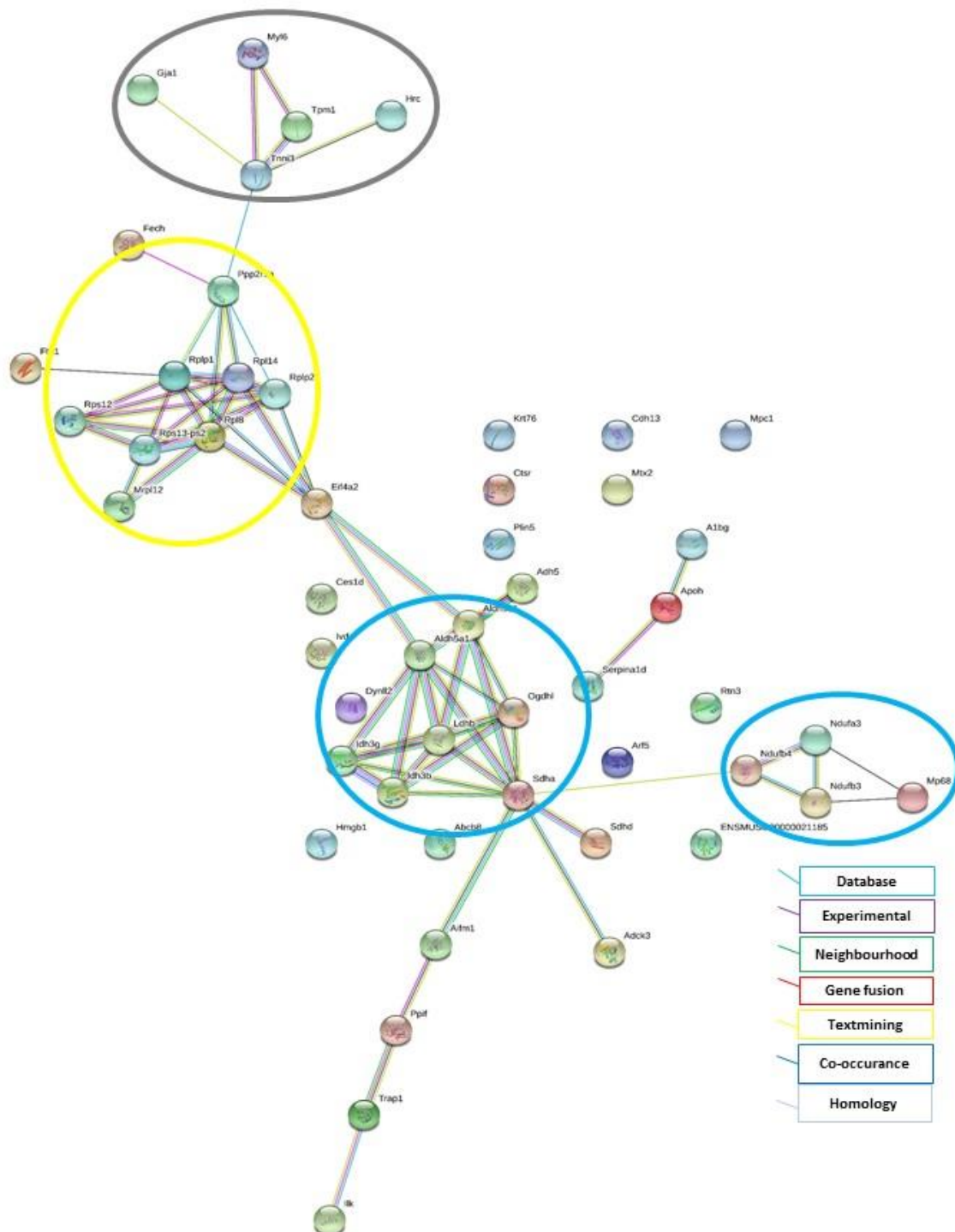KO-SHAM vs KO-TAC down-regulated protein cluster

Fig. S5. Full view of STRING analysis of Group C, KO-SHAM vs KO-TAC proteome (down-regulated). Analysis of protein interaction network by STRING, Coloured lines between the proteins indicate the protein co-occurrence, co-expression, known interactions and predicted interactions. Interconnecting major clusters show mitochondrial proteins (blue circle), ribosomal proteins (yellow circle) and cytoskeleton proteins (grey circle) in down-regulated proteins.

Supplementary figure. S6: STRING cluster analysis
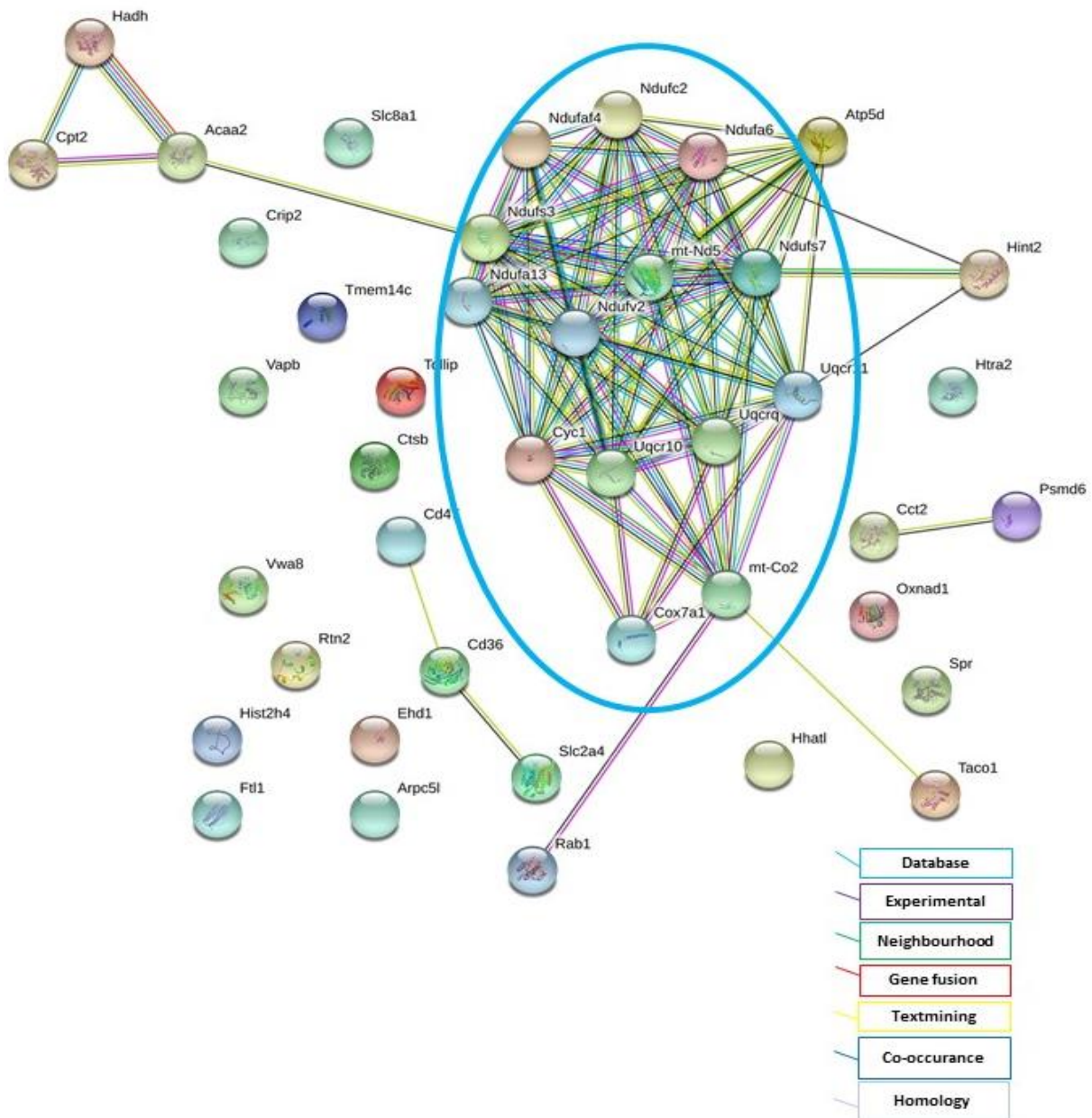WT-TAC vs KO-TAC up-regulated protein cluster

Fig. S6. Full view of STRING analysis of Group D, WT-TAC vs KO-TAC proteome (up-regulated). Analysis of protein interaction network by STRING, Coloured lines between the proteins indicate the protein co-occurrence, co-expression, known interactions and predicted interactions. Up-regulated proteins show Interconnecting major cluster shows mitochondrial proteins (blue circle) . Interconnecting major clusters show ribosomal proteins (yellow circle) and cytoskeleton proteins (grey circle) (**D**).

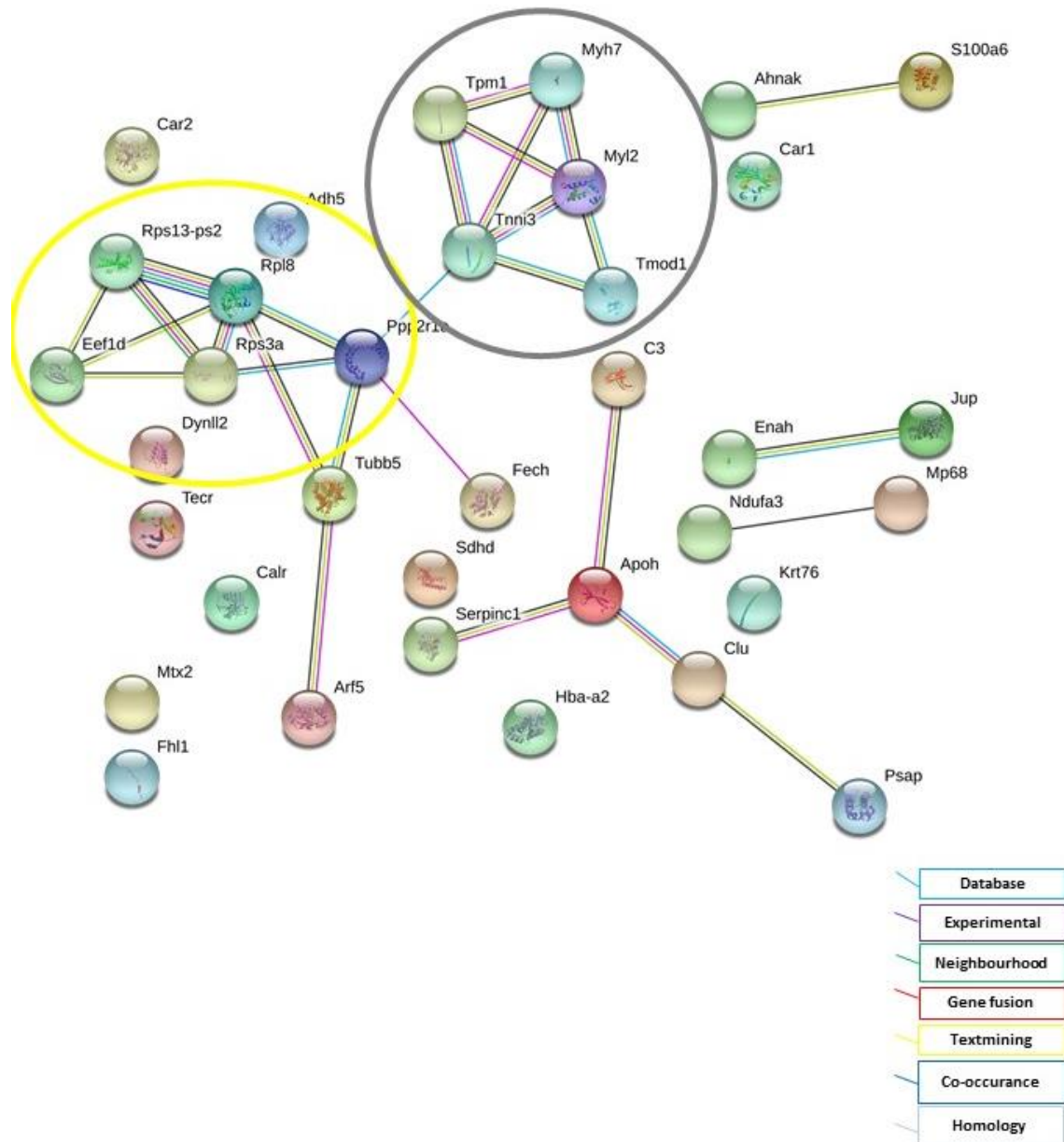**Supplementary figure. S7: STRING cluster analysis KO-SHAM vs KO-TAC down-regulated protein cluster**

Fig. S7. Full view of STRING analysis of Group D, WT-TAC vs KO-TAC proteome (down-regulated). Analysis of protein interaction network by STRING, Coloured lines between the proteins indicate the protein co-occurrence, co-expression, known interactions and predicted interactions. Interconnecting major clusters show ribosomal proteins (yellow circle) and cytoskeleton proteins (grey circle).

8. Acknowledgements

Ph.D. duration was one of the challenging times of my life, there are many people who helped me and made my journey feasible. There are not enough words to say thanks them for their help, love and guidance.

Firstly, I would like to express my deepest gratitude to my mentor **Dr. Krishna Pantakani** for providing me great opportunity to work with him. I would like to thank for his valuable support, guidance and for being always available to help me out not only in research work but in all other situations. I would like to thank him for his patience, enthusiasm and valuable scientific discussion and ideas for my Ph.D. work and projects. I also wanted to show my gratitude to him for guiding, editing and proof reading my annual reports, presentations, and without him this thesis too, would not have been completed. I consider myself very fortunate for being able to work with a very encouraging person.

I would like to sincerely thank **Prof. Dr. Ibrahim Adham** for accepting to be my first supervisor and member of my thesis committee. I would like to show my gratitude to his suggestions and guidance during my annual meetings and also for giving consent to edit my thesis.

I also owe gratitude to **Prof. Dr. Sigrid Hoyer-Fender** for being a part of my Thesis advisory committee and to be my co-referee. I want to thank her for providing guidance and support during my annual thesis committee meetings.

I would like to thank **Prof. Dr. Abdul. R. Asif** for providing an inspiring working environment in his research group at Institute for Clinical Chemistry for my Ph.D. studies. His valuable suggestions and support also guided me through difficult times of Ph.D. I would also like to thank him for proof reading my thesis despite his busy schedule.

I want to thank my institutional head **Prof. Dr. Lutz Binder** for allowing me to proceed my research work in Institute for Clinical Chemistry. I also want to thank him for travel grants and research funding whenever it was needed.

In my daily working environment, I have been blessed with a nice lab group. In my lab group firstly, I would like to thank **Marlena Pantakani** for scientific discussions and good friendship. She has been very helpful in optimization and troubleshooting of lab

problems. Her calm and friendly nature also helped me in solving problems outside the work environment. I want to thank her for good time spent together.

I am indeed thankful to **Reiner Andag**, for his professional technical support and for being a great person to work with. I thank him for being so patient and helpful to multiple technical problems I would bring to him.

I also want to thank my other colleagues including **Priyadharsini Raju**, **Rieke Welzbecher, Sandra Hartung, Ulrike** and **Jenny Gao** for their support and help in lab.

Most specifically, I want to thank my best friend **Neelam Younas** for her care, kindness, fantastic positive attitude to work and tremendous moral support in my difficult times. I want to thank her for our shared laughter, fights, late night walks, travel and drama. She has been an excellent listener and good advisor throughout these years. There are no words to explain how much she helped and guided me.

I also want to show my gratitude to **Dr. Muzna Zahur** for her friendship, care and support. Her nice and positive attitude always helped me to pass through difficult times.

I would like to thank my other friends from all over the world for their support and encouragement. Special thanks to **Sehar Afreen** (for long telephonic chit chat), **Anum Ali Ahmad** (for being positive and supportive), **Humaira Gul** (for shared laughter and encouragement) and **Madiha Nasir** (for lively discussions). I also want to thank **Maryam Afzal** (for humour and irritating me with her singing talent), **Nida Amin** (for being supportive) **Atika Wahab** (for being a nice company), and **Mohsin Shafiq** (for helping me).

Last but not least I owe huge gratitude to my family members for their love, support, prayer and trust. This thesis for sure is a tribute to my Late Father "**Shahid Bashir**" for giving me strength and giving me confidence to achieve my goals. I want to thank my mother "**Naveeda Shahid**", but what can I say? There are no words to describe her love, care and courage. It wouldn't have been possible for me to complete my Ph.D. without your support and your faith in me.

Most specifically, I want to thank my eldest sister **Mariam Shahid** for being so supportive in my life. Her care, advise, love, scolding and continued moral support gave me strength to be here today. I want to thank her for being a role model for me with her bravery, courage and strength. I am indebted to her for giving a greatest gift of my life

in September 2009 which brought brightness, happiness and purpose in my life. I want to show my gratitude to my sisters (**Faiza, Humera, Sadia, Rabia, Binte-Azra** and **Fehda**) and to my brothers (**Farooq, Zubair, Faisal, Khurram, Imran, Talha** and **Ahsan**) for their love, prayers and support. During my Ph.D. times, I missed you guys a lot, but it also gave me realisation that I have been blessed with a great, sweet and supportive family.

My acknowledgements are incomplete without special thanks to my little sweet stars **Moeen, Hadiya, Umama, Mohid, Hafsa** and **Khizar**. Without any doubt I missed you guys the most and your videos and pictures gave me happiness and a lift whenever I was sad. You guys made my visits memorable and cherishable.

9. Curriculum Vitae

Name	Sidra Shahid
Address	Herman Rein Strasse 9, Apartment No. 314, 37075, Goettingen
Email	shahidsidra@yahoo.com
Date of birth	21.05.1987
Place of birth	Lahore, Pakistan
Permanent address	109, CII block, Johar Town Lahore, Pakistan
Nationality	Pakistan
Languages	English, Urdu, German

Educational Background

2014 to date	Ph.D. student, Dissertation: "Role of BRD4 and its target Ptp1b in Endothelial cells and in cardiovascular disease models"
	Institute for Clinical Chemistry, UMG, Goettingen.
2010-2012	Degree, M.Phil (Molecular Biology)
	Dissertation: "Linkage analysis is a tool for carrier screening and genetic counselling of hearing impairment."
	Centre of excellence in Molecular Biology (CEMB)
	University of Punjab, Lahore Pakistan.
2007-2009	Degree, M.Sc (Microbiology and Molecular Genetics)
	Department of Microbiology and Molecular Genetics (MMG)
	University of Punjab, Lahore Pakistan.
2005-2007	Degree, B.Sc (Biology)
	University of Punjab, Lahore Pakistan.
2003-2005	Degree F.Sc (pre-Medical)
	Lahore board Pakistan.

Oral Presentation

123. German Conference of Laboratory Medicine Mannheim, 30th September 2016. Title: **"Phosphoproteome analysis of mouse hearts from endothelial specific knockout of Protein Tyrosine phosphatase 1B (PTP1B)".** Abstract published online in " Clinical Chemistry and Laboratory Medicine (CCLM)", Volume 54, Issue 10, Pages eA367–eA473, ISSN (Online) 1437-4331, ISSN (Print) 1434-662".

Poster Presentation

125. German Conference of Laboratory Medicine Mannheim, 29th September 2018. Title: **"Inhibition of BRD4 by JQ1 and RVX-208 rescues endothelial cell dysfunction in an in vitro model of atherosclerosis".** Abstract will be published online in " Clinical Chemistry and Laboratory Medicine (CCLM), Volume 57.